Tunable, continuous-wave semiconductor disk lasers with emission in the deep ultraviolet

A thesis presented in fulfilment of the
requirements for the degree of

Doctor of Philosophy

by

Julio M. Rodríguez-García

Department of Physics
University of Strathclyde

2017

This thesis is the result of the author's original research. It has been composed by the author and has not been previously submitted for examination which has led to the award of a degree.

Signed: _____

Date: _____

A mis Padres

que me inculcaron la pasión por el saber
y me proporcionaron los medios para que pudiera perseguirlo.

¡Gracias!

Acknowledgements

I would like to express my wholehearted gratitude to my supervisors: Dr. Jennifer Hastie, for accepting me in her research group and providing guidance during my first steps in this vast landscape of scientific research (and her careful, inexhaustible proofreading will never be forgotten); Professor Alan Kemp, who has always been willing to help despite his many responsibilities; and to Dr. David Stothard, for his eager enthusiasm and his peculiar expressions. Dr. David Pabœuf also deserves a special place in this page for his continuous support, guidance, advice, fruitful (and not) discussions and friendship; and for putting up with all my jokes. My gratitude also belongs to Doctors Peter Schlosser, Daniele Parrotta and Brynmor Jones for a warm welcome into the team and for sharing their expertise and experience with me in countless occasions during these years; and to the other members of the Advance Lasers Group, for they all provided valuable contributions to the work here presented.

Many thanks to Elisabeth, for the company, the conversation, the motivation and *die schere*; to Riccardo, for all those hours, dawn to dusk, unravelling the mysteries of lasers; to Doug, for his teachings about beer; to Katie, for teaching me English and Luke, for teaching me Glaswegian; and to Giuseppe, for sharing his vast knowledge about pizza and pasta. Many thanks to Antoine and Caroline for their French charm. And to all the students, post-docs and staff of the Institute of Photonics (too many to name them all) that make it a friendly and welcoming place, a big thank you to you all.

Without the inestimable help of Sharon, Grace and Lorraine I would still be finding my way around the academic bureaucracy instead of writing this thesis, thank you a lot!

Tengo muchísimo que agradecer a mi primo Manuel (conocido en otros círculos como el Dr. Rodríguez-Pascual), amigo y mentor. Sus consejos y ayuda sin duda han simplificado el camino hasta aquí (y su habilidad informática hizo posible SimCav). Así mismo, muchísimas gracias al Dr. Rafa Mayo-García por acogerme en el CIEMAT y abrirme la puerta al mundo investigador. Me gustaría también expresar mi agradecimiento a los Doctores Daniel Jaque, Manuel Marqués y Pablo Pernas, por su dedicación y apoyo, que se extendieron más allá de las clases. Muchas gracias a los colegas, por estar ahí, y a mi familia, en particular a mis padres, por su comprension y ayuda constante. Esta tesis también es un poco vuestra.

Por último, quiero dar las gracias a Ester por compartir esta aventura conmigo. Por acompañarme hasta estas lejanas tierras, por disfrutar con mis excentricidades, por encargarse de todo en mis momentos de escritura más entregada y, sobre todo, por aguantarme todos estos años. ¡Gracias!

Abstract

The work here presented is focused around the design, characterization and ultimately first demonstration of a deep ultraviolet, frequency tripled semiconductor disk laser (SDL). The construction of such a laser is described, together with a review of the relevant theory and investigation of the underlying processes in order to improve the system.

SDLs based on gallium indium phosphide have attracted intense investigation over the last ten years for their fundamental emission in the 660 nm – 690 nm (visible red emission), a region previously only available to SDLs by means of nonlinear frequency conversion. Such frequency conversion applied to red SDLs provides access to the highly energetic ultraviolet region of the electromagnetic spectum but, although its conversion to the near ultraviolet has been rather successful, further extension into the deep UV presents a new set of challenges that must be addressed in order to achieve efficient laser emission. 78 µW of deep ultraviolet emission at 225 nm have been achieved in continuous-wave operation. The output wavelength is tunable for 350 cm^{-1}. This is the shortest wavelength emitted from an SDL to date and is the first implementation of intracavity frequency tripling in a visible SDL.

Contents

List of Figures

CHAPTER 1

Introduction

A laser (acronym for light amplification by stimulated emission of radiation) is a device that makes use of the quantum effect of stimulated emission to produce electromagnetic radiation (visible or invisible light). Unlike conventional light sources, photons emitted by lasers are identical (in particular same wavelength, phase, polarization and direction of propagation) which results in a low divergence, highly coherent beam of light (laser beam).

Stimulated emission occurs when the process of an electron dropping from an excited state to a lower energy state is induced by an incoming photon with the same energy as the difference between electronic levels. In this case, the photon emitted by the demoting electron is identical to the original photon, including direction of propagation. A comparison with the common absorption and spontaneous emission can be seen in figure 1.1. For a large group of atoms spontaneous emission would produce photons with the same energy but random directions or relative phases, while stimulated emission can produce a large number of identical photons (thus amplifying the original signal).

In general, a laser is made by a gain medium placed in an optical resonator. In this system the circulating wave is amplified in the gain medium each time it passes through.

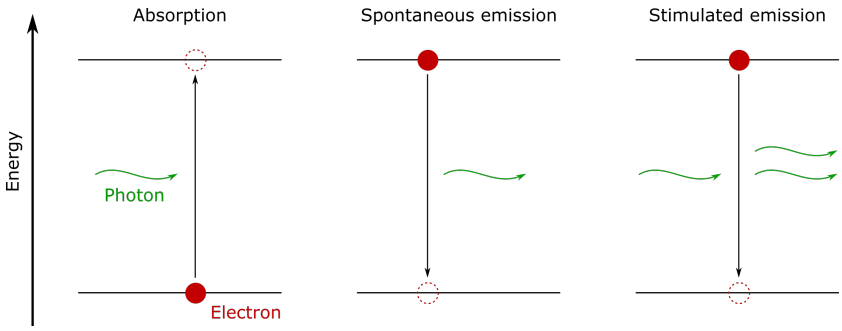

Figure 1.1: Absorption, spontaneous emission and stimulated emission from an electron changing between two energy levels.

The mirrors composing the resonator only allow transmission of a fraction of the light, the laser output. Energy must be pumped into the gain medium, by either electrical or optical means, in order to produce gain. When the gain compensates the resonator losses, laser emission occurs (laser threshold).

Lasers are nowadays omnipresent devices. From simple laser pointers to industrial and military applications, fundamental roles in many disciplines of scientific research and even solutions in medicine, most of our current technology has benefited from the advent of lasers.

1.1 Historical introduction

It was a hundred years ago, in the frame of the quantum revolution that led to modern physics, that Albert Einstein published several papers on light-matter interaction, proposing stimulated emission and photon momentum [1, 2], and furthering the development of quantum electrodynamics. However it was not until ten years later that experimental evidence for stimulated emission was found [3]. During the following years, especially after the light amplification proposals of Weber, Prokhorov and Basov [4, 5], and in parallel with academic research, several companies became involved in a race to develop this new device that was already being envisioned. Finally, in 1954, almost four decades after Einstein's ideas, Townes, Gordon and Zeiger built a device that produced

and amplified coherent microwaves using stimulated emission, that came to be called the maser (microwave amplification by stimulated emission of radiation [6]).

This success led to frenetic research in the field, with theoretical works followed closely by experimental demonstrations, such as the proposal of a three-level system in 1956 [7] followed by an experimental three-level maser in 1957 [8]. In 1958 Schawlow and Townes published their study on extension of the working range of masers to the infrared and visible spectral regions [9] in gas. However, new experiments were being carried out at the time, showing ruby as a suitable material for maser operation [10, 11]. Maiman used a solid-state design with ruby as the active material to produce, in 1960, coherent emission at 694 nm [12]. The laser was born.

The following years witnessed an accelerated expansion of the laser universe. New active materials were quickly tested, giving rise, for example, to the nowadays common neodymium laser [13] or the helium-neon laser, the first one working in continuous operation [14]. Applications in many fields were quickly unfolded and the potential of lasers unleashed, which led to a Nobel Prize being awarded to Townes, Basov and Prokhorov in 1964 "for fundamental work in the field of quantum electronics, which has led to the construction of oscillators and amplifiers based on the maser-laser principle". But the laser History had just begun.

1.1.1 From homojunctions to quantum wells

In 1962, the first semiconductor lasers were developed almost simultaneously by researchers working in the General Electric research laboratory [15], IBM [16] and MIT [17]. These first devices consisted of GaAs homojunctions (two layers made of the same compound) working at cryogenic temperatures, emitting near 850 nm (corresponding to the GaAs bandgap of ∼1.45 eV). Coherent visible radiation from GaAsP junctions was reported later that year [18]. Heterojunctions (in which materials with different bandgaps are used) were devised within a year by Kazarinov and Alferov [19], and

independently by Kroemer [20]. Alferov and Kroemer shared the Nobel Prize in 2000 "for developing semiconductor heterostructures used in high-speed- and opto-electronics". Advancement in the topic continued, reaching room temperature, continuous-wave operation in 1970, in AlAs/GaAs [21] and GaAs/AlGaAs [22] heterostructures.

Initially, heterostructures were seen as a means to produce a barrier for confining electrons to the gain region, but it did not take long for the quantum confinement properties of thin layers between barriers to be considered and experimentally tested. The development of quantum well lasers was a major advance (remarkable is the work of Charles H. Henry from 1972 [23], which led to working devices in 1975 [24]) and room temperature operation was achieved over the next year [25].

This new design was able to reach threshold at much lower current than its bulk counterparts (thanks to the localisation of the carriers closer to the band edges as will be described in the next chapter), producing more efficient laser operation. First measurements are not only clarifying, but also emblematic, such as seen in figure 1.2 comparing absorption of semiconductor layers of different thickness featuring bulk and quantum well optical absorption. The exciton absorption is observable, as is the separation of the energy levels for different quantum well thickness.

The emergence of improved semiconductor growing techniques also played an important role in the development of quantum well lasers: initially liquid phase epitaxy (LPE), in which thin films are grown from metallic solutions [26], was used to grow the semiconductor samples, but while this technique was suitable for growing bulk semiconductor layers (on the order of 2000 Å thick) it was not capable of dealing with the narrow thicknesses required to observe electronic quantum effects (a few nanometres, on the order of the De Broglie wavelength of electrons). Molecular beam epitaxy (MBE), in which vaporised elements condense over a wafer reacting with each other in high vacuum conditions [27], had been developed in 1968 [28] and by 1971 was a suitable method for crystal growth [29], offering the possibility of growing much thinner layers than those made by LPE. Quantum well lasers would surpass the performance of bulk

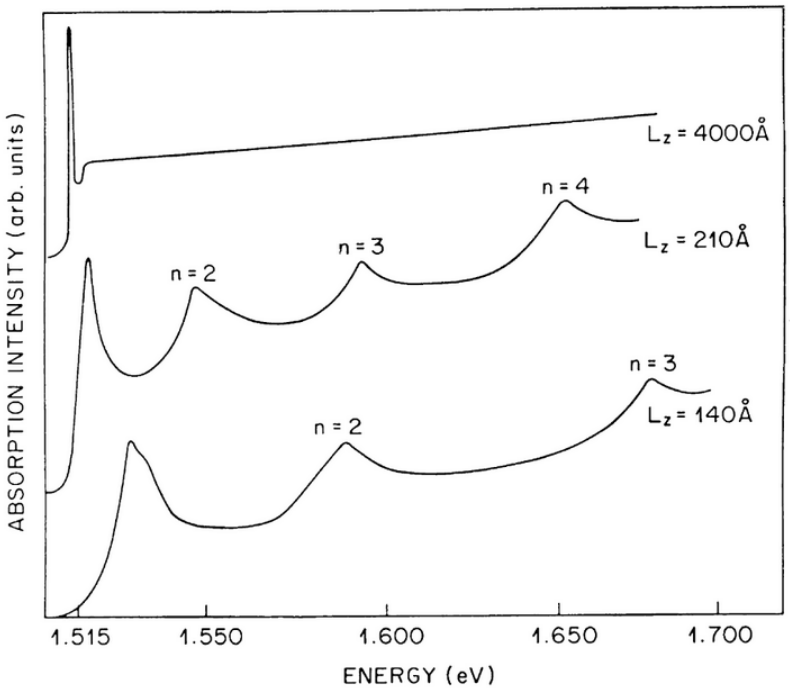

Figure 1.2: Absorption spectra at 2K in GaAs layers, both bulk (4000 Å) and quantum well (210 Å and 140 Å). The quantized measurements feature exciton absorption for each energy level, while only the first exciton is evident in the bulk sample [23].

semiconductor lasers in the following years. Another technique called metal organic chemical vapour deposition (MOCVD), in which chemical reactions are used to deposit vaporised elements over the substrate (as opposed to physical deposition as in MBE) [30], was used to make AlGaAs heterostructure lasers in 1977 [31], showing as good performance as LPE grown devices. While original quantum well lasers used electrical pumping, optical pumping (photopumped lasers) was also successfully employed with single or multi quantum well devices [32, 33]. MBE saw a major advance by the hand of Tsang [34] when he achieved laser thresholds similar to those offered by LPE. In the following years even lower threshold operation would be obtained [35, 36].

Quantum well lasers were accepted to have significant advantages over bulk semiconductor lasers by the early 80s, and publications on QWs quickly increased with research on this topic acquiring a popularity that is still maintained nowadays.

1.1.2 Semiconductor lasers

Semiconductors have triggered a revolution in the field of electronics as well as in optics. Their character in between conductors and insulators, together with our capability of control over certain properties (bandgap, conductivity...), provides us with a broad range of possibilities that have meant they are present in most of current human technology. Alloys of different materials and compositions make it possible to engineer the semiconductor bandgap to target specific applications.

Likewise, semiconductor lasers are the most common type of laser nowadays due to their many advantages. They are easy and cheap to mass produce and easy to integrate with the ubiquitous electronics. Their sub-millimetre size is also an advantage when it comes to gadget integration. Power is supplied by electrical injection, which increases their convenience, so metal contacts are added on top and bottom surfaces as connection with an external circuit. Electrical injection, however, requires material doping to favour conduction, which increases the growth complexity. Current diffusion can also be challenging depending on the device geometry. Materials used are usually limited to direct bandgap semiconductors; indirect bandgap materials do not exhibit efficient light emission since de-excitation also involves phonon emission (see figure 1.3).

Semiconductor lasers can be divided in two groups depending on the direction of laser oscillation / emission, as schematically shown in figure 1.4. Devices in which the oscillation happens parallel to the plane of the gain region are defined as edge emitters, while surface emitters are those in which oscillation happens perpendicular to said plane. There are of course benefits and drawbacks for each approach, which are considered in the following discussion.

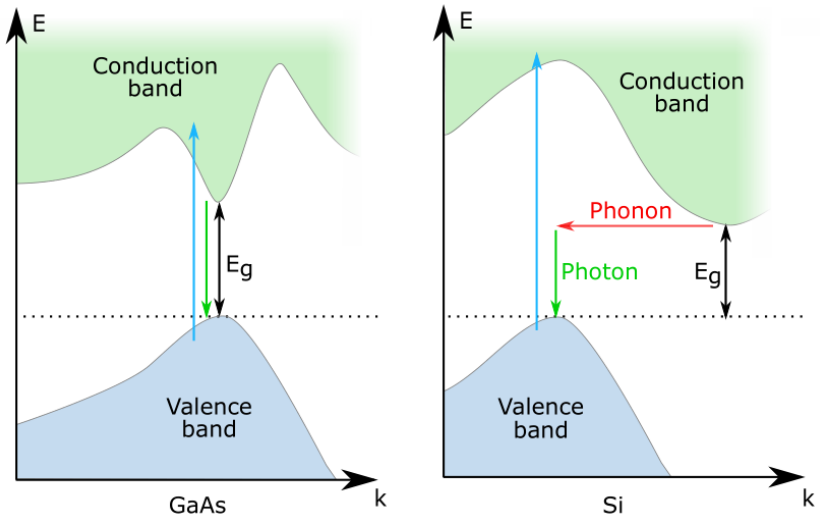

Figure 1.3: Direct and indirect bandgaps as occur in gallium arsenide (GaAs) and silicon (Si). Band transitions in indirect bandgap materials involve phonons, reducing the photon emission efficiency. Illustration from Jones [37].

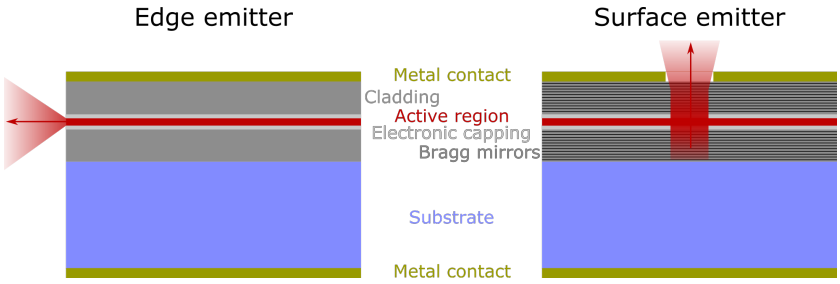

Figure 1.4: Comparison between edge emitting and surface emitting lasers.

Edge emitters

Edge emitting lasers correspond to the original architecture. Simple to grow, oscillation perpendicular to epitaxial growth provides gain over the longer axis of the active region, while reflection is provided by the cleaved edges of the structure (the facets act as end mirrors). Fresnel reflection is in this case large enough to achieve laser operation thanks to the long active region (dimensions as those of the sample itself, of hundreds of micrometres), that provides high gain and thus high tolerance to losses.

This type of semiconductor laser is capable of high power operation, and large arrays can be built for kW level output powers. Unfortunately, the emitter geometry leads to poor beam quality, and there is usually a trade-off between beam quality and output power: the larger the dimensions on the plane of emission the more laser emission, but also the more spatial modes present. This elliptical and highly divergent output was the main reason for the development of surface emitting lasers.

Surface emitters

Surface emitters appeared as early as 1979 [38], introduced in order to improve upon the beam quality of edge emitters. Although at that time this new device was not efficient and worked in pulsed operation at cryogenic temperatures, further development led to vertical cavity surface emitting lasers (VCSELS) being widely used nowadays.

The short gain region, which benefits from advances in quantum wells or even quantum dots, makes these lasers low gain devices, and Fresnel reflection is no longer enough to achieve laser operation, and highly reflective mirrors (usually monolithically grown distributed Bragg reflectors, DBR) are required on both ends of the cavity. Low gain and high reflective mirrors, together with current injection requirements, mean high power is not achievable with these devices. Beam quality is in exchange a great improvement over edge emitters, offering a diffraction limited TEM_{00} mode.

In an attempt to maintain the excellent beam properties of surface emitters with the added possibility of high power operation, semiconductor disk lasers were developed.

Introduction to semiconductor disk lasers

Semiconductor disk lasers (SDLs) are closely related with VCSELs and the former are often referred to as vertical-external cavity surface-emitting lasers (VECSELs).

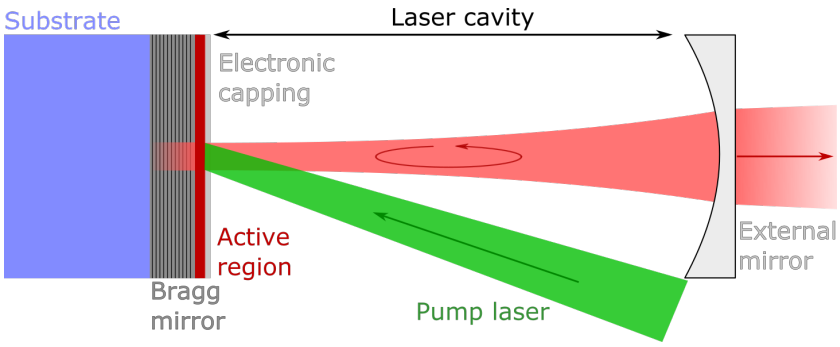

Figure 1.5: Schematic of a semiconductor disk laser.

The similarity of the names, together with the widespread applications of VCSELs, commonly causes confusion; for that reason SDL is preferred in this thesis.

Broadly speaking, in order to move from a VCSEL to a SDL, one of the Bragg mirrors is omitted from the heterostructure and is substituted by a (highly reflective) external mirror. The semiconductor structure that once was a self-contained laser becomes a gain mirror and the laser itself now extends beyond the semiconductor to the external mirror (figure 1.5), creating a macro laser cavity to which we can have access, thus allowing us to employ the huge intracavity power stored within.

Contrary to the previously described semiconductor lasers, SDL qualities are better exploited using optical pumping instead of electrical injection. With optical pumping the design of the gain structure must be calculated for optimum pump absorption, but in exchange doping is not required, greatly simplifying the growth process and therefore improving the quality of the layers. The active region is generally made of multiple quantum wells for efficient laser operation. With appropriate longitudinal mode control, very narrow linewidth operation may be achieved, while the broad gain offered by this gain medium means SDLs can be broadly tuned around their central wavelength. Beam quality, benefiting from the emission geometry, is also improved by control over the alignment of the external resonator. Due to SDLs being low gain devices the transmittance of the output coupling mirror is limited to just a few percent.

More complex setups, that make use of several highly reflective mirrors, are also possible (and actually preferred to two mirror cavities): V, Z or bowtie cavities are common with these devices. Complex setups allow for fine control over the beam geometry so collimated and focused beams with desired sizes can be obtained in the different segments of the laser cavity. These segments are large enough to place optical elements within them (providing that the intracavity losses caused are kept to a minimum) so different applications may be targeted. In particular, the work hereafter described will make use of nonlinear crystals to produce intracavity frequency conversion, benefiting from the strong intracavity fields. Further details on SDLs physics and design can be found in Chapter 2.

Development of SDLs

The first demonstration of a surface-emitting laser operating in an external cavity came in 1991 [39], using a multi-quantum well, InGaAs/InP semiconductor laser emitting at 1.5 µm. No DBR was included in the growing process (the most common format used now), instead reflection was provided by a gold coating of the structure surface. The output power of this system was 60 times higher than that of previous VCSELs, and allowed for mode-locked operation (a technique to produced pulsed output) for the first time with a surface emitter. The following year, the first mode-locked GaAs-based external cavity semiconductor laser was reported [40]. In 1996, continuous operation was presented [41] with a device that included an antireflection coating grown together with the DBR and active region. These early systems were still considered to be types of VCSEL devices, and the pump sources used were both dye and solid state lasers. A proposal to truly differentiate these lasers from VCSELs came in 1997 [42]. This system made use of a commercial diode laser as the pump source, achieving high power operation with a TEM_{00} mode. The suitability of these lasers for nonlinear frequency conversion was first exploited in 1999 to produce blue light at 490 nm from a fundamental infrared wavelength of 980 nm [43]. The same year, single frequency

operation was also demonstrated with a linewidth of 3 kHz [44]. Thermal management, a problem commonly reported in these early experiments, was shown to be improved by means of an optically-contacted transparent heatspreader in 2002 [45].

InGaP material for emission in the visible red (660 nm) was first achieved in 2002 [46], although it worked in pulsed operation and high power operation was only achieved for temperatures under −30 °C. Work carried in the Institute of Photonics led to efficient visible (674 nm) SDLs near room temperature [47] and at ultraviolet wavelengths (337 nm) via second harmonic generation [48]. The work described in this thesis aims to extend SDL coverage to the deep ultraviolet.

The development of SDLs has accelerated since, with new results and improved performance been published every few months. In particular, the spectral coverage of these lasers has greatly expanded: while the first devices were InGaAs based, emitting in the near infrared around 1 µm, nowadays fundamental operation has been demonstrated from 640 nm to beyond 5 µm [49, 50], with pioneering demonstrations at wavelengths as short as 400 nm [51]. Figure 1.6 shows SDL emission for different materials in continuous-wave operation. Results maximizing particular aspects, such as high power [52, 53] or pulsed operation [54], can be found in the literature over the last years. In particular, narrow linewidth SDLs for quantum technologies are currently being develop in the Institute of Photonics within the initiative of the UK National Quantum Technology Hub for Sensors and Metrology [55]. Semiconductor disk lasers are also replacing older solid state solutions in commercial products. As an example, the new Verdi G-series from Coherent Inc. [56], based on this type of device, offers a more compact and practical laser source than its preceding solid-state based V-series at the same wavelength and power (532 nm, over 18 W) [56, 57].

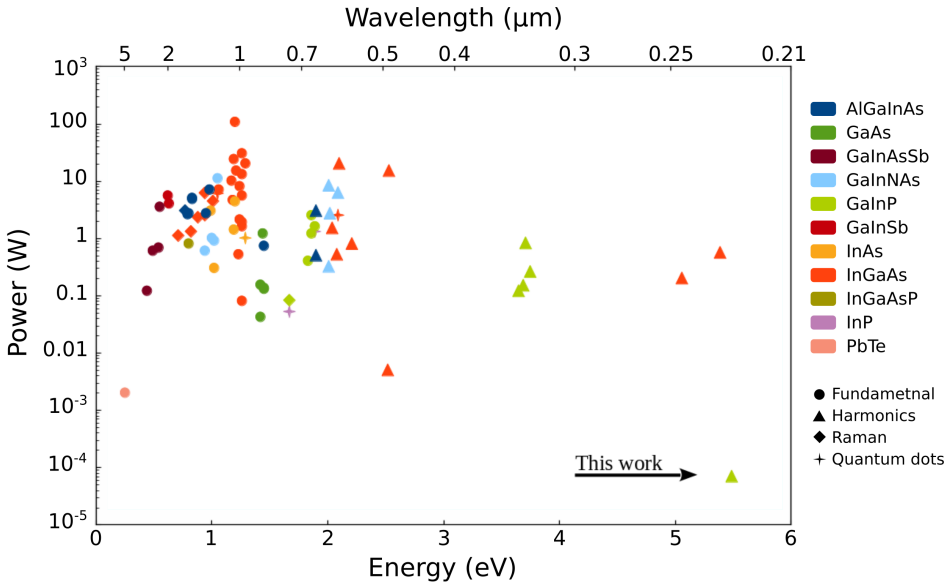

Figure 1.6: Spectral coverage of CW SDLs, with circles representing fundamental emission, triangles for harmonic generation, rhombs for Raman conversion and stars for quantum dots. The color code represents different quantum well material compositions. [42–45, 47, 48, 52, 58–111].

1.2 Deep UV lasers

Ultraviolet (UV) lasers have been increasingly developed and improved over recent years due to the wide range of applications in many different areas, including spectroscopy. However, tunable, continuous-wave, UV lasers are still scarce. Most UV lasers operate in the pulsed regime, with the disadvantage of systematic frequency shifts which can limit the achievable precision on high resolution spectroscopic experiments [112], and at fixed wavelengths. A good example is the HeAg gas laser, with emission at 224.3 nm [113].

The ultraviolet region can be reached via non-linear frequency conversion as a means to use more convenient laser sources. The most common UV laser sources include dye- and solid-state lasers, frequency-converted to higher-energy wavelengths. Depending on the initial (fundamental) wavelength, one or more non-linear conversion steps may be necessary to reach the UV region of the spectrum. In general, at least two conversion

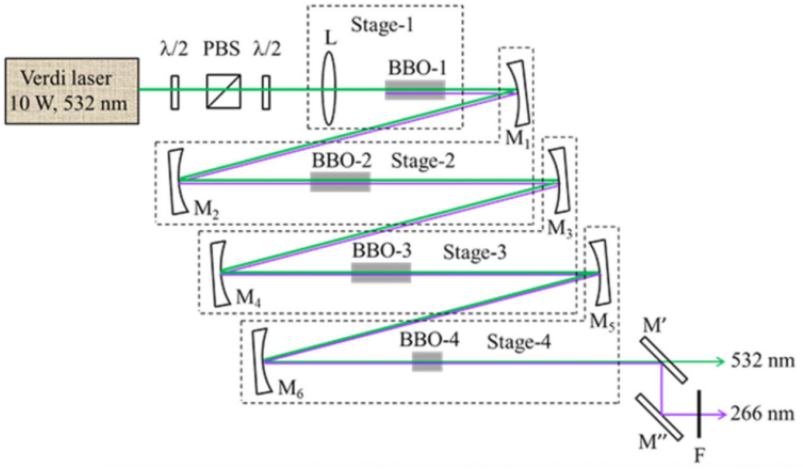

Figure 1.7: Multicrystal, single-pass second harmonic generation [114]. The multiple BBO crystals are aligned so each of them contributes to compensate birefringent walk-off (intensity distribution drifting away from the wavevector direction, section 3.2.7).

stages are needed in order to reach wavelengths around 200 nm. Frequency conversion can be obtained with non-linear crystals, such as LBO, BBO, KDP... but the current setups are rather complicated due to the fact that each conversion is done in a different resonant cavity. Removing the external resonators in order to simplify the system is also possible, but to deal with the reduced input power multiple passes or pulsed operation are often needed (see figure 1.7) [114]. In general, when working with nonlinear frequency conversion, a compromise is needed between continuous wave operation and high power.

Dye lasers usually provide a broad bandwidth, being especially suitable as tunable and pulsed lasers, although with many of the dyes being toxic (and of course not solid-state) working with them is inherently impractical. These lasers are also an example of cumbersome architecture and high cost. Another example of widely tunable, UV sources are frequency-converted Ti:sapphire lasers, with the advantage of working with a solid-state gain medium albeit also expensive (figure 1.8). Emission over a broad range of wavelengths has been shown [115–117], although the lower limit of their spectral coverage implies conversion into higher harmonics (e.g. 4^{th}, 5^{th}...) is required to reach

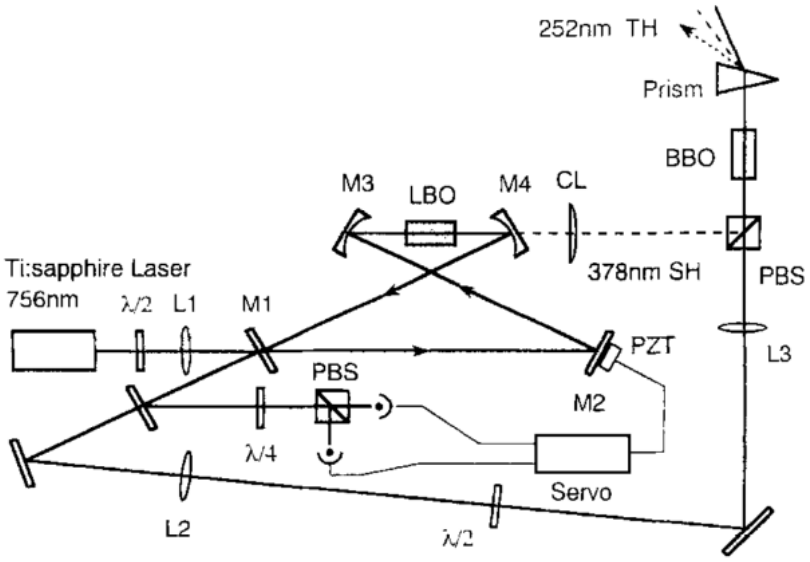

Figure 1.8: Frequency tripled Ti:sapphire laser. Neither of the nonlinear steps are integrated in the laser cavity resulting in a large, complex system. An enhancing resonator is used for high efficiency SHG, while sum-frequency mixing takes place in a single pass. Figure reproduced from [115].

deep UV emission. Similarly to dye lasers, Ti:Sapphire lasers often work in pulsed operation, for which they are especially suited given their very broad gain bandwidth.

Continuous wave, deep UV laser systems have already been reported, and we can find examples such as single frequency operation at 213 nm via sum frequency mixing (in an external enhancement cavity) of the outputs of an amplified 1064 nm Nd:YAG laser and an externally-quadrupled Nd:YVO4 laser to reach the fifth harmonic [118] (figure 1.9a), and the generation of over 2 mW at 194 nm via sum-frequency mixing of the amplified output of a 792 nm diode laser with the second harmonic of a 514 nm argon ion laser (frequency-doubled in an external enhancement cavity, see figure 1.9b) [119]. Both examples make use of actively stabilised external enhancement cavities (two and three cavities respectively) to maximise the optical fields inside the nonlinear crystals. This widely used technique gives very good results, but at the same time means dealing with very complex setups. Of particular note is the recent result by Ruhnke *et al.* of 16 µW CW at 222.5 nm via frequency doubling of a high power, single frequency GaN external cavity diode laser [120]. In contrast to previous examples, no enhancement

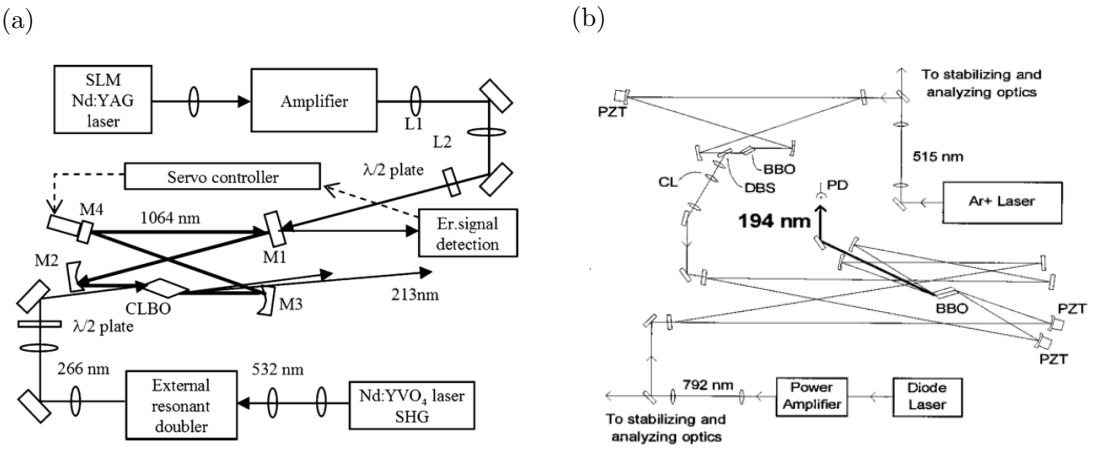

Figure 1.9: Sum-frequency setups using complex enhancing external resonators to produce emission in the deep UV. Figures reproduced from [118, 119].

cavity is used in this system, resulting in µW level output power. Starting with the short emission of GaN at 445 nm reduces to one the nonlinear conversion steps required to reach deep UV emission, simplifying systems based on infrared lasers that often need 4 or 5 conversion stages.

Kaneda *et al.* have demonstrated single frequency deep UV emission using an infrared SDL with multi-Watt output, making use of the already discussed external enhancing cavities to achieve efficient second and fourth harmonic generation in successive stages [88, 89]. This approach avoids introducing losses to the SDL at the expense of adding complexity to the setup, as can be seen in figure 1.10. The external cavity of SDLs with the strong intracavity fields stored within, together with the low optimum output coupling close to frequency conversion typical levels, has proven to be a very simple yet efficient design as long as the intracavity losses can be controlled [49, 121].

The intracavity tripling approach has been considered since at least the early 80s, especially with Nd: lasers [122–125]. The infrared starting wavelength means only the near ultraviolet can be reached in this manner, now competing with frequency doubling from visible SDLs, quickly improving nowadays [48, 126]. To the author's knowledge, there is only one demonstration of a tripled (infrared) SDL [127]. As with the previous

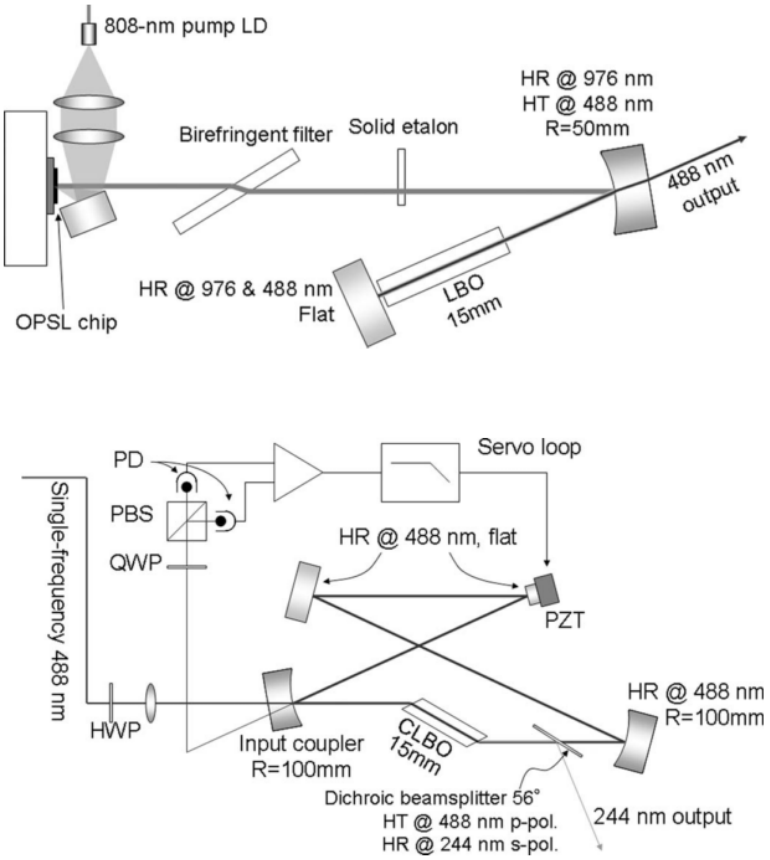

Figure 1.10: This SDL takes advantage of the strong intracavity fields for the first nonlinear step, requiring an enhancing external resonator to carry out the second nonlinear step. Figure reproduced from [88].

examples, the infrared fundamental wavelength means the wavelength achieved is in the near UV (355 nm) and, moreover, a full analysis of the optimisation of the nonlinear conversion is not reported. This previous work in frequency tripling certainly provides an encouraging precedent for our work but, as will be described in the following chapters, extending towards higher photon energies presents additional challenges.

1.3 Applications

As described in the previous sections, SDLs are not micro devices due to their optical pump and external cavity; akin to more conventional solid-state lasers. The straightforward conclusion is that these lasers cannot easily be part of integrated systems for mass produced consumer devices. SDLs are much more specialised devices that can provide solutions for scientific and industrial applications offering great capabilities such as excellent beam quality, both at low and high power, with surface emitting geometry satisfying the requirements for power scaling. The broad gain of the quantum well active region enables wide tunability, which together with engineered emission wavelength, ensures excellent wavelength flexibility.

This work is focused on extending the spectral coverage of SDLs into the deep ultraviolet region by means of intracavity nonlinear frequency conversion. Previous research has already shown excellent results converting the emission of SDLs from the infrared into the visible region and even the near ultraviolet. We aim to extend this capability to produce higher energy photons with two intracavity conversion stages, such that the visible red field of the SDL at 675 nm is transformed into emission at 225 nm, in the deep ultraviolet region of the electromagnetic spectrum.

Numerous applications can make use of lasers targeting electronic transitions over 4.5 eV, a region where electronic transitions of small molecules start to happen (e.g. organic compounds and nitrogen and oxygen reactive species). Spectroscopy in particular would benefit from a continuous-wave and tunable laser source in the deep UV, and the all-solid-state character and compact design make SDLs suitable for in-field measurements, given that current laser sources are costly and large enough to make in-field measurements cumbersome (eg. dye lasers pumped by harmonics of solid-state lasers) [128, 129].

Atmospheric and combustion spectroscopy, together with environmental sensing, are suggested as potential beneficiaries of this system, with important transitions occurring

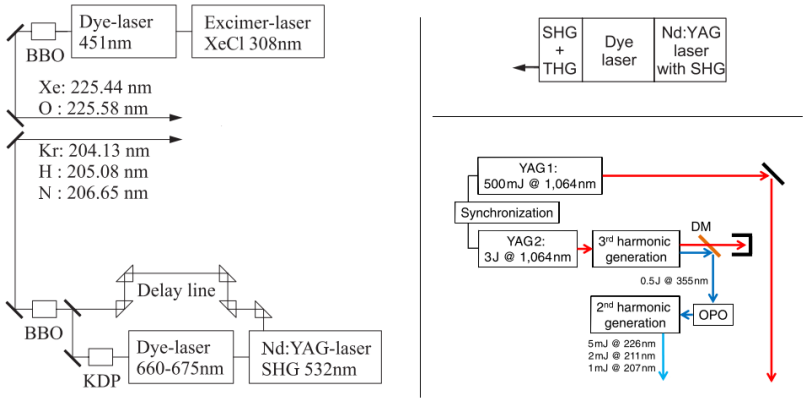

Figure 1.11: Some examples of current laser sources used in spectroscopy [131, 132, 134].

at the targeted wavelengths: nitric oxide (NO), a major pollutant in combustion processes [130], or two-photon resonance of atomic oxygen (O_2) present transitions around 225 nm [131, 132]. Study of metallic compounds is also possible at these wavelengths, with gold, for example, requiring probe photons over 5.1 eV [133]. Gas, excimer and dye lasers are typically employed (or a combination of them), which results in complex and expensive setups (figure 1.11). At the same time, most deep UV wavelengths are limited to pulsed operation.

Non-line of sight communications (NLOS) could also benefit from a compact and low power UVC laser source. Earth is naturally protected against incoming ultraviolet radiation from space by the atmosphere, minimizing interference (the region between 200 nm and 280 nm is called solar-blind), and atmospheric scattering provides a mechanism for NLOS transmission of information at such wavelengths [135]. Underwater communications may also consider this kind of laser source, also benefiting from its solar-blind wavelength [136, 137]. Research in this area, however, also requires significant effort on the development of suitable detectors given the required sensitivity [136].

1.4 Introduction to the work in this thesis

Using a semiconductor disk laser we propose a compact solution to reach wavelengths around 225 nm. A tunable, continuous-wave laser with potential for power scaling is developed. In addition to the broad gain that allows tuning over several nanometres, the wavelength-engineered semiconductor gain region means it will be possible to access an even wider range of wavelengths with a similar setup.

The following chapters will review the background and general theory required for this work, with Chapter 2 focused on semiconductor disk lasers. Semiconductor gain structure design is described, including strain and thermal management, together with a review of the characteristics that make these lasers so versatile. A preliminary characterization of the SDL in fundamental operation is also reported.

Chapter 3 delineates nonlinear frequency conversion theory. Starting with a brief description of nonlinear optics history and basics, and a review of the most important nonlinear optical processes, the mathematical description of second harmonic generation (SHG) and sum-frequency generation (SFG) is summarised. Both processes will be employed in our experiments and full understanding of them is crucial for optimum implementation.

Chapter 4 describes the design of the laser system, considerations and compromises, experiments and results. The design of the laser cavity is challenging for an all intracavity set-up, and a new software tool for laser design was developed in the process (described in Appendix A). The choice of nonlinear crystals is discussed, with options restricted by the limited availability for deep UV wavelengths. Two experimental setups were built to achieve intracavity tripling, and both are described and compared with the achieved results. Some improvements are also suggested at the end of the chapter.

Chapter 5 takes a closer look into the theoretical details of intracavity tripling and describes simulations carried out to understand the complex processes taking place and suggests further improvements to the system. Apart from the inherent limitations of the nonlinear processes at such short wavelengths, beam propagation and overlap were also of concern and both are analysed here, with the first part focusing on beam propagation and the second part, on limitations of the nonlinear process within our system. The process analysis becomes very complex due to the vast number of variables involved, and we tried to weight the effect of the most important ones on the third harmonic output power. Conclusions on system improvements are given at the end.

Finally, Chapter 6 concludes with an overview of the work and results described in this thesis and considers the future direction of the work. The main achievement is the creation of a tunable and continuous wave, all-solid-state laser source that can emit coherent radiation around 225 nm, which led to a publication in a peer-reviewed journal [80] (a List of Publications is included at the end). The output power is 78 µW, and the tuning range is almost 2 nm. The emission wavelength is potentially extendable to a wider range given the broad visible emission of SDLs. This is, to the best of our knowledge, the first implementation of intracavity tripling in a visible SDL and the shortest wavelength emitted from an SDL to date.

References

[1] A. Einstein. “Strahlungs-emission und absorption nach der quantentheorie”. In: *Deutsche Physikalische Gesellschaft* 18 (1916), pp. 318–323.

[2] A. Einstein. “Zur Quantentheorie der Strahlung”. In: *Physikalische Zeitschrift* 18 (1917), pp. 121–128.

[3] H. Kopfermann and R. Ladenburg. “Experimental Proof of Negative Dispersion”. In: *Nature* 122.3073 (Sept. 1928), pp. 438–439. DOI: 10.1038/122438a0.

[4] J. Weber. “Amplification of microwave radiation by substances not in thermal equilibrium”. In: *Transactions of the IRE Professional Group on Electron Devices* PGED-3.3 (June 1953), pp. 1–4. DOI: 10.1109/IREPGED.1953.6811068.

[5] A. Prokhorov and N. Basov. “Molecular generator and amplifier”. In: *Uspekhi Fizicheskih Nauk* 57.3 (1955), pp. 485–501.

[6] J. P. Gordon, H. J. Zeiger, and C. H. Townes. “Molecular microwave oscillator and new hyperfine structure in the microwave spectrum of NH_3”. In: *Physical Review* 95.1 (1954), pp. 282–284. DOI: 10.1103/PhysRev.95.282.

[7] N. Bloembergen. “Proposal for a New Type Solid State Maser”. In: *Physical Review* 104.2 (Oct. 1956), pp. 324–327. DOI: 10.1103/PhysRev.104.324.

[8] H. E. D. Scovil, G. Feher, and H. Seidel. “Operation of a Solid State Maser”. In: *Physical Review* 105.2 (Jan. 1957), pp. 762–763. DOI: 10.1103/PhysRev.105.762.

[9] A. L. Schawlow and C. H. Townes. “Infrared and Optical Masers”. In: *Physical Review* 112.6 (Dec. 1958), pp. 1940–1949. DOI: 10.1103/PhysRev.112.1940.

[10] G. Makhov, C. Kikuchi, J. Lambe, and R. W. Terhune. “Maser Action in Ruby”. In: *Physical Review* 109.4 (Feb. 1958), pp. 1399–1400. DOI: 10.1103/PhysRev.109.1399.

[11] C. Kikuchi, J. Lambe, G. Makhov, and R. W. Terhune. "Ruby as a maser material". In: *Journal of Applied Physics* 30.7 (1959), pp. 1061–1067. DOI: 10.1063/1.1776979.

[12] T. H. Maiman. "Optical and microwave-optical experiments in ruby". In: *Physical Review Letters* 4.11 (1960), pp. 564–566. DOI: 10.1103/PhysRevLett.4.564.

[13] E. Snitzer. "Optical maser action of Nd^{+3} in a barium crown glass". In: *Physical Review Letters* 7.12 (1961), pp. 444–446. DOI: 10.1103/PhysRevLett.7.444.

[14] A. Javan, W. R. Bennett, and D. R. Herriott. "Population Inversion and Continuous Optical Maser Oscillation in a Gas Discharge Containing a He-Ne Mixture". In: *Physical Review Letters* 6.3 (Feb. 1961), pp. 106–110. DOI: 10.1103/PhysRevLett.6.106.

[15] R. N. Hall, G. E. Fenner, J. D. Kingsley, T. J. Soltys, and R. O. Carlson. "Coherent Light Emission From GaAs Junctions". In: *Physical Review Letters* 9.9 (Nov. 1962), pp. 366–368. DOI: 10.1103/PhysRevLett.9.366.

[16] M. I. Nathan, W. P. Dumke, G. Burns, F. H. Dill, and G. Lasher. "Stimulated emission of radiation From GaAs p-n junctions". In: *Applied Physics Letters* 1.3 (Nov. 1962), pp. 62–64. DOI: 10.1063/1.1777371.

[17] T. M. Quist, R. H. Rediker, R. J. Keyes, W. E. Krag, B. Lax, A. L. McWhorter, and H. J. Zeigler. "Semiconductor maser of GaAs". In: *Applied Physics Letters* 1.4 (Dec. 1962), pp. 91–92. DOI: 10.1063/1.1753710.

[18] N. Holonyak and S. F. Bevacqua. "Coherent (visible) light emission from $Ga(As_{1-x}P_x)$ junctions". In: *Applied Physics Letters* 1.4 (Dec. 1962), pp. 82–83. DOI: 10.1063/1.1753706.

[19] Z. I. Alferov and R. Kazarinov. *Double heterostructure laser*. 1963.

[20] H. Kroemer. "A proposed class of hetero-junction injection lasers". In: *Proceedings of the IEEE* 51.12 (Dec. 1963), pp. 1782–1783. DOI: 10.1109/PROC.1963.2706.

[21] Z. I. Alferov, V. Andreev, E. Portnoi, and M. Trukan. "AlAs-GaAs heterojunction injection lasers with a low room-temperature threshold". In: *Sov Phys Semiconductors* 3.9 (1970), pp. 1107–1110.

[22] I. Hayashi, M. B. Panish, P. W. Foy, and S. Sumski. "Junction lasers which operate continuously at room temperature". In: *Applied Physics Letters* 17.3 (Aug. 1970), pp. 109–111. DOI: 10.1063/1.1653326.

[23] R. Dingle, W. Wiegmann, and C. H. Henry. "Quantum States of Confined Carriers in Very Thin $Al_xGa_{1-x}As$-GaAs-$Al_xGa_{1-x}As$ Heterostructures". In: *Physical Review Letters* 33.14 (Sept. 1974), pp. 827–830. DOI: 10.1103/PhysRevLett.33.827.

[24] J. P. van der Ziel, R. Dingle, R. C. Miller, W. Wiegmann, and W. A. Nordland. "Laser oscillation from quantum states in very thin GaAs-$Al_{0.2}Ga_{0.8}As$ multilayer structures". In: *Applied Physics Letters* 26.8 (1975), pp. 463–465. DOI: 10.1063/1.88211.

[25] R. C. Miller, R. Dingle, A. C. Gossard, R. A. Logan, W. A. Nordland, and W. Wiegmann. "Laser oscillation with optically pumped very thin GaAs–Al_xGa_{1-x} As multilayer structures and conventional double heterostructures". In: *Journal of Applied Physics* 47.10 (Oct. 1976), pp. 4509–4517. DOI: 10.1063/1.322422.

[26] E. Kuphal. "Liquid phase epitaxy". In: *Applied Physics A Solids and Surfaces* 52.6 (June 1991), pp. 380–409. DOI: 10.1007/BF00323650.

[27] A. Y. Cho and J. R. Arthur. "Molecular beam epitaxy". In: *Progress in Solid State Chemistry* 10.3 (1975), pp. 157–191. DOI: 10.1016/0079-6786(75)90005-9.

[28] J. R. Arthur. "Interaction of Ga and As_2 Molecular Beams with GaAs Surfaces". In: *Journal of Applied Physics* 39.8 (July 1968), pp. 4032–4034. DOI: 10.1063/1.1656901.

[29] A. Y. Cho. "Film Deposition by Molecular-Beam Techniques". In: *Journal of Vacuum Science and Technology* 8.5 (Sept. 1971), S31–S38. DOI: 10.1116/1.1316387.

[30] J. Coleman. "Metalorganic chemical vapor deposition for optoelectronic devices". In: *Proceedings of the IEEE* 85.11 (1997), pp. 1715–1729. DOI: 10.1109/5.649647.

[31] R. D. Dupuis and P. D. Dapkus. "Room-temperature operation of $Ga_{1-x}Al_xAs$/GaAs double-heterostructure lasers grown by metalorganic chemical vapor deposition". In: *Applied Physics Letters* 31.7 (Oct. 1977), pp. 466–468. DOI: 10.1063/1.89743.

[32] N. Holonyak, R. M. Kolbas, R. D. Dupuis, and P. D. Dapkus. "Room-temperature continuous operation of photopumped MO–CVD $Al_xGa_{1-x}As$–GaAs–Al_xGa_{1-x} As quantum–well lasers". In: *Applied Physics Letters* 33.1 (July 1978), pp. 73–75. DOI: 10.1063/1.90150.

[33] N. Holonyak, R. M. Kolbas, W. D. Laidig, B. A. Vojak, R. D. Dupuis, and P. D. Dapkus. "Lowthreshold continuous laser operation (300–337K) of multilayer MO-CVD $Al_xGa_{1-x}As$–GaAs quantum–well heterostructures". In: *Applied Physics Letters* 33.8 (Oct. 1978), pp. 737–739. DOI: 10.1063/1.90522.

[34] W. T. Tsang. "Low-current-threshold and high-lasing uniformity GaAs–$Al_xGa_{1-x}As$ double-heterostructure lasers grown by molecular beam epitaxy". In: *Applied Physics Letters* 34.7 (Apr. 1979), pp. 473–475. DOI: 10.1063/1.90839.

[35] W. T. Tsang. "Extremely low threshold (AlGa)As modified multiquantum well heterostructure lasers grown by molecular-beam epitaxy". In: *Applied Physics Letters* 39.10 (Nov. 1981), pp. 786–788. DOI: 10.1063/1.92583.

[36] W. T. Tsang. "Extremely low threshold (AlGa)As graded-index waveguide separate-confinement heterostructure lasers grown by molecular beam epitaxy". In: *Applied Physics Letters* 40.3 (Feb. 1982), pp. 217–219. DOI: 10.1063/1.93046.

[37] B. E. Jones. "ZnCdMgSe and AlGaInP multi-quantum well films for colour conversion and optically-pumped visible lasers". PhD thesis. University of Strathclyde, 2015, p. 201.

[38] H. Soda, K.-I. Iga, C. Kitahara, and Y. Suematsu. "GaInAsP/InP Surface Emitting Injection Lasers". In: *Japanese Journal of Applied Physics* 18.12 (Dec. 1979), pp. 2329–2330. DOI: 10.1143/JJAP.18.2329.

[39] W. B. Jiang, S. R. Friberg, H. Iwamura, and Y. Yamamoto. "High powers and subpicosecond pulses from an external-cavity surface-emitting InGaAs/InP multiple quantum well laser". In: *Applied Physics Letters* 58.8 (1991), pp. 807–809. DOI: 10.1063/1.104495.

[40] W. B. Jiang, R. Mirin, and J. E. Bowers. "Mode-locked GaAs vertical cavity surface emitting lasers". In: *Applied Physics Letters* 60.6 (1992), pp. 677–679. DOI: 10.1063/1.106562.

[41] J. V. Sandusky and S. R. J. Brueck. "A CW external-cavity surface-emitting laser". In: *IEEE Photonics Technology Letters* 8.3 (1996), pp. 313–315. DOI: 10.1109/68.481101.

[42] M. Kuznetsov, F. Hakimi, R. Sprague, and A. Mooradian. "High-Power (0.5W CW) Diode-Pumped Vertical-External-Cavity Surface-Emitting Semiconductor Lasers with Circular TEM_{00} Beams". In: *IEEE Photonics Technology Letters* 9.8 (1997), pp. 1063–1065. DOI: 10.1109/68.605500.

[43] T. D. Raymond, W. J. Alford, M. H. Crawford, and A. A. Allerman. "Intracavity frequency doubling of a diode-pumped external-cavity surface-emitting semiconductor laser." In: *Optics letters* 24.16 (1999), pp. 1127–9. DOI: 10.1364/OL.24.001127.

[44] M. Holm, D. Burns, A. Ferguson, and M. Dawson. "Actively stabilized single-frequency vertical-external-cavity AlGaAs laser". In: *IEEE Photonics Technology Letters* 11.12 (1999), pp. 1551–1553. DOI: 10.1109/68.806843.

[45] W. J. Alford, T. D. Raymond, and A. A. Allerman. "High power and good beam quality at 980 nm from a vertical external-cavity surface-emitting laser". In: *Journal of the Optical Society of America B* 19.4 (2002), p. 663. DOI: 10.1364/JOSAB.19.000663.

[46] M. Mueller, N. Linder, C. Karnutsch, W. Schmid, K. P. Streubel, J. Luft, S.-S. Beyertt, A. Giesen, and G. H. Doehler. "Optically pumped semiconductor thin-disk laser with external cavity operating at 660 nm". In: *Symposium on Integrated Optoelectronic Devices*. Ed. by C. Lei and S. P. Kilcoyne. San Jose: SPIE, June 2002, p. 265. DOI: 10.1117/12.469242.

[47] J. E. Hastie, S. Calvez, M. D. Dawson, T. Leinonen, A. Laakso, J. Lyytikäinen, and M. Pessa. "High power CW red VECSEL with linearly polarized TEM_{00} output beam". In: *Optics Express* 13.1 (Jan. 2005), p. 77. DOI: 10.1364/OPEX.13.000077.

[48] J. E. Hastie, L. G. Morton, A. J. Kemp, M. D. Dawson, A. B. Krysa, and J. S. Roberts. "Tunable ultraviolet output from an intracavity frequency-doubled red vertical-external-cavity surface-emitting laser". In: *Applied Physics Letters* 89.6 (Aug. 2006), p. 061114. DOI: 10.1063/1.2236108.

[49] S. Calvez, J. E. Hastie, M. Guina, O. G. Okhotnikov, and M. D. Dawson. "Semiconductor disk lasers for the generation of visible and ultraviolet radiation". In: *Laser & Photonics Review* 3.5 (Sept. 2009), pp. 407–434. DOI: 10.1002/lpor.200810042.

[50] N. Schulz, J. M. Hopkins, M. Rattunde, D. Burns, and J. Wagner. "High-brightness long-wavelength semiconductor disk lasers". In: *Laser and Photonics Reviews* 2.3 (July 2008), pp. 160–181. DOI: 10.1002/lpor.200710037.

[51] R. Debusmann, N. Dhidah, V. Hoffmann, L. Weixelbaum, U. Brauch, T. Graf, M. Weyers, and M. Kneissl. "InGaN-GaN disk laser for blue-violet emission wavelengths". In: *IEEE Photonics Technology Letters* 22.9 (2010), pp. 652–654. DOI: 10.1109/LPT.2010.2043668.

[52] B. Heinen, T.-L. Wang, M. Sparenberg, A. Weber, B. Kunert, J. Hader, S. Koch, J. Moloney, M. Koch, and W. Stolz. "106 W continuous-wave output power from vertical-external-cavity surface-emitting laser". In: *Electronics Letters* 48.9 (2012), p. 516. DOI: 10.1049/el.2012.0531.

[53] P. Holl, M. Rattunde, S. Adler, S. Kaspar, W. Bronner, A. Bachle, R. Aidam, and J. Wagner. "Recent Advances in Power Scaling of GaSb-Based Semiconductor Disk Lasers". In: *IEEE Journal of Selected Topics in Quantum Electronics* 21.6 (Dec. 2015). DOI: 10.1109/JSTQE.2015.2414919.

[54] B. W. Tilma, M. Mangold, C. A. Zaugg, S. M. Link, D. Waldburger, A. Klenner, A. S. Mayer, E. Gini, M. Golling, and U. Keller. "Recent advances in ultrafast semiconductor disk lasers". In: *Light: Science & Applications* 4.7 (July 2015), e310. DOI: 10.1038/lsa.2015.83.

[55] K. Bongs, V. Boyer, M. A. Cruise, A. Freise, M. Holynski, J. Hughes, A. Kaushik, Y.-H. Lien, A. Niggebaum, M. Perea-Ortiz, P. Petrov, S. Plant, Y. Singh, A. Stabrawa, D. J. Paul, M. Sorel, D. R. S. Cumming, J. H. Marsh, R. W. Bowtell, M. G. Bason, R. P. Beardsley, R. P. Campion, M. J. Brookes, T. Fernholz, T. M. Fromhold, L. Hackermuller, P. Krüger, X. Li, J. O. Maclean, C. J. Mellor, S. V. Novikov, F. Orucevic, A. W. Rushforth, N. Welch, T. M. Benson, R. D. Wildman, T. Freegarde, M. Himsworth, J. Ruostekoski, P. Smith, A. Tropper, P. F. Griffin, A. S. Arnold, E. Riis, J. E. Hastie, D. Paboeuf, D. C. Parrotta, B. M. Garraway, A. Pasquazi, M. Peccianti, W. Hensinger, E. Potter, A. H. Nizamani, H. Bostock, A. Rodriguez Blanco, G. Sinuco-Leon, I. R. Hill, R. A. Williams, P. Gill, N. Hempler, G. P. A. Malcolm, T. Cross, B. O. Kock, S. Maddox, and P. John. "The UK National Quantum Technologies Hub in sensors and metrology (Keynote Paper)". In: *SPIE 9900 Quantum Optics* 9900 (2016), p. 990009. DOI: 10.1117/12.2232143.

[56] Coherent. *Verdi G-Series Family.* https://cohrcdn.azureedge.net/assets/pdf/Verdi-G-Series-Family-Data-Sheet.pdf. 2013.

[57] Coherent. *Verdi V-Series Family.* https://cohrcdn.azureedge.net/assets/pdf/Verdi-Family-Data-Sheet.pdf. 2011.

[58] A. Sirbu, N. Volet, A. Mereuta, J. Lyytikäinen, J. Rautiainen, O. Okhotnikov, J. Walczak, M. Wasiak, T. Czyszanowski, A. Caliman, Q. Zhu, V. Iakovlev, and E. Kapon. "Wafer-Fused Optically Pumped VECSELs Emitting in the 1310-nm

and 1550-nm Wavebands". In: *Advances in Optical Technologies* 2011 (2011), p. 8. DOI: 10.1155/2011/209093.

[59] A. Sirbu, A. Rantamäki, E. J. Saarinen, V. Iakovlev, A. Mereuta, J. Lyytikäinen, A. Caliman, N. Volet, O. G. Okhotnikov, and E. Kapon. "High performance wafer-fused semiconductor disk lasers emitting in the 1300 nm waveband". In: *Optics Express* 22 (Dec. 2014), p. 29398. DOI: 10.1364/OE.22.029398.

[60] A. Rantamäki, A. Sirbu, A. Mereuta, E. Kapon, and O. G. Okhotnikov. "3 W of 650 nm red emission by frequency doubling of wafer-fused semiconductor disk laser". In: *Optics Express* 18 (Sept. 2010), p. 21645. DOI: 10.1364/OE.18.021645.

[61] J. Lyytikainen, J. Rautiainen, A. Sirbu, V. Iakovlev, A. Laakso, S. Ranta, M. Tavast, E. Kapon, and O. G. Okhotnikov. "High-Power 1.48-μm Wafer-Fused Optically Pumped Semiconductor Disk Laser". In: *IEEE Photonics Technology Letters* 23 (July 2011), pp. 917–919. DOI: 10.1109/LPT.2011.2143399.

[62] S. J. McGinily, R. Abram, K. S. Gardner, E. Riis, A. I. Ferguson, and J. S. Roberts. "Novel Gain Medium Design for Short-Wavelength Vertical-External-Cavity Surface-Emitting Laser". In: *IEEE Journal of Quantum Electronics* 43.6 (June 2007), pp. 445–450. DOI: 10.1109/JQE.2007.895666.

[63] J. Rautiainen, J. Lyytikäinen, A. Sirbu, A. Mereuta, A. Caliman, E. Kapon, and O. G. Okhotnikov. "2.6 W optically-pumped semiconductor disk laser operating at 157-μm using wafer fusion". In: *Optics Express* 16 (Dec. 2008), p. 21881. DOI: 10.1364/OE.16.021881.

[64] M. Schmid, S. Benchabane, F. Torabi-Goudarzi, R. Abram, A. I. Ferguson, and E. Riis. "Optical in-well pumping of a vertical-external-cavity surface-emitting laser". In: *Applied Physics Letters* 84.24 (June 2004), pp. 4860–4862. DOI: 10.1063/1.1760887.

[65] D. Burns, J.-M. Hopkins, A. J. Kemp, B. Rösener, N. Schulz, C. Manz, K. Köhler, M. Rattunde, and J. Wagner. "Recent developments in high-power short-wave mid-infrared semiconductor disk lasers". In: *Solid State Lasers XVIII: Technology*

and Devices. Ed. by W. A. Clarkson, N. Hodgson, and R. K. Shori. Vol. 7193. SPIE, Feb. 2009, p. 719311. DOI: 10.1117/12.811977.

[66] J.-M. Hopkins, A. J. Maclean, D. Burns, E. Riis, N. Schulz, M. Rattunde, C. Manz, K. Köhler, and J. Wagner. "Tunable, Single-frequency, Diode-pumped 2.3μm VECSEL". In: *Optics Express* 15.13 (2007), p. 8212. DOI: 10.1364/OE.15.008212.

[67] J. Nikkinen, J. Paajaste, R. Koskinen, S. Suomalainen, and O. G. Okhotnikov. "GaSb-Based Semiconductor Disk Laser With 130-nm Tuning Range at 2.5 μm". In: *IEEE Photonics Technology Letters* 23 (June 2011), pp. 777–779. DOI: 10.1109/LPT.2011.2122249.

[68] B. Rösener, M. Rattunde, R. Moser, S. Kaspar, T. Töpper, C. Manz, K. Köhler, and J. Wagner. "Continuous-wave room-temperature operation of a 28μm GaSb-based semiconductor disk laser". In: *Optics Letters* 36 (Feb. 2011), p. 319. DOI: 10.1364/OL.36.000319.

[69] A. Härkönen, J. Rautiainen, M. Guina, J. Konttinen, P. Tuomisto, L. Orsila, M. Pessa, and O. G. Okhotnikov. "High power frequency doubled GaInNAs semiconductor disk laser emitting at 615 nm". In: *Optics Express* 15.6 (2007), p. 3224. DOI: 10.1364/OE.15.003224.

[70] V.-M. Korpijärvi, T. Leinonen, J. Puustinen, A. Härkönen, and M. D. Guina. "11 W single gain-chip dilute nitride disk laser emitting around 1180 nm". In: *Optics Express* 18.25 (Nov. 2010), pp. 25633–25641. DOI: 10.1364/oe.18.025633.

[71] M. Guina, ed. *8W GaInNAs VECSEL emitting at 615 nm*. Vol. 22. 6. Mar. 2015, p. 934909. DOI: 10.1117/12.2079162.

[72] J. Rautiainen, A. Härkönen, V.-M. Korpijärvi, P. Tuomisto, M. Guina, and O. G. Okhotnikov. "2.7 W tunable orange-red GaInNAs semiconductor disk laser". In: *Optics Express* 15.26 (2007), p. 18345. DOI: 10.1364/oe.15.018345.

[73] J.-M. Hopkins, S. Smith, C. W. Jeon, H. Sun, D. Burns, S. Calvez, M. D. Dawson, T. Jouhti, and M. Pessa. "0.6 W CW GaInNAs vertical external-cavity surface

emitting laser operating at 1.32 μm". In: *Electronics Letters* 40.1 (2004), p. 30. DOI: 10.1049/el:20040049.

[74] J. Konttinen, A. Härkönen, P. Tuomisto, M. Guina, J. Rautiainen, M. Pessa, and O. Okhotnikov. "High-power (>1 W) dilute nitride semiconductor disk laser emitting at 1240 nm". In: *New Journal of Physics* 9.5 (May 2007), p. 140. DOI: 10.1088/1367-2630/9/5/140.

[75] S. Vetter, S. Calvez, M. Dawson, F. Fusari, A. Lagatsky, W. Sibbett, C. Brown, V.-M. Korpijarvi, M. Guina, B. Richards, G. Jose, and A. Jha. "1213nm semiconductor disk laser pumping of a Tm^{3+}-doped tellurite glass laser". In: *LEOS 2008 - 21st Annual Meeting of the IEEE Lasers and Electro-Optics Society*. IEEE, Nov. 2008, pp. 840–841. DOI: 10.1109/leos.2008.4688883.

[76] P. J. Schlosser, D. C. Parrotta, V. G. Savitski, A. J. Kemp, and J. E. Hastie. "Intracavity Raman conversion of a red semiconductor disk laser using diamond". In: *Optics Express* 23.7 (Mar. 2015), p. 8454. DOI: 10.1364/oe.23.008454.

[77] H. Kahle, R. Bek, M. Heldmaier, T. Schwarzbäck, M. Jetter, and P. Michler. "High optical output power in the UVA range of a frequency-doubled, strain-compensated AlGaInP-VECSEL". In: *Applied Physics Express* 7.9 (Sept. 2014), p. 092705. DOI: 10.7567/APEX.7.092705.

[78] C. M. N. Mateo, U. Brauch, H. Kahle, R. Bek, T. Schwarzbäck, M. Jetter, M. Abdou Ahmed, P. Michler, and T. Graf. "Efficiency and power scaling of in-well and multi-pass pumped AlGaInP VECSELs". In: *SPIE 9734*. Ed. by K. G. Wilcox. Mar. 2016, p. 973410. DOI: 10.1117/12.2212162.

[79] T. Schwarzbäck, H. Kahle, M. Jetter, and P. Michler. "Frequency doubled AlGaInP-VECSEL with high output power at 331 nm and a large wavelength tuning range in the UV". In: ed. by K. Panajotov, M. Sciamanna, A. Valle, and R. Michalzik. June 2012, 84320W. DOI: 10.1117/12.922584.

[80] J. M. Rodríguez-García, D. Pabœuf, and J. E. Hastie. "Tunable, CW Laser Emission at 225 nm via Intracavity Frequency Tripling in a Semiconductor Disk

Laser". In: *IEEE Journal of Selected Topics in Quantum Electronics* 23.6 (Nov. 2017), pp. 1–8. DOI: 10.1109/JSTQE.2017.2696882.

[81] S. Baumgärtner, H. Kahle, R. Bek, T. Schwarzbäck, M. Jetter, and P. Michler. "Comparison of AlGaInP-VECSEL gain structures". In: *Journal of Crystal Growth* 414 (Mar. 2014), pp. 219–222. DOI: 10.1016/j.jcrysgro.2014.10.016.

[82] T. Schwarzbäck, M. Eichfelder, W.-M. Schulz, R. Roßbach, M. Jetter, and P. Michler. "Short wavelength red-emitting AlGaInP-VECSEL exceeds 1.2 W continuous-wave output power". In: *Applied Physics B* 102.4 (Mar. 2011), pp. 789–794. DOI: 10.1007/s00340-010-4213-5.

[83] J. Paajaste, S. Suomalainen, R. Koskinen, A. Härkönen, M. Guina, and M. Pessa. "High-power and broadly tunable GaSb-based optically pumped VECSELs emitting near 2μm". In: *Journal of Crystal Growth* 311.7 (Mar. 2009), pp. 1917–1919. DOI: 10.1016/j.jcrysgro.2008.10.071.

[84] M. Hoffmann, O. D. Sieber, V. J. Wittwer, I. L. Krestnikov, D. A. Livshits, Y. Barbarin, T. Südmeyer, and U. Keller. "Femtosecond high-power quantum dot vertical external cavity surface emitting laser". In: *Optics Express* 19 (Apr. 2011), p. 8108. DOI: 10.1364/OE.19.008108.

[85] A. R. Albrecht, C. P. Hains, T. J. Rotter, A. Stintz, K. J. Malloy, G. Balakrishnan, and J. V. Moloney. "High power 1.25 μm InAs quantum dot vertical external-cavity surface-emitting laser". In: *Journal of Vacuum Science Technology B: Microelectronics and Nanometer Structures* 29.3 (2011), p. 03C113. DOI: 10.1116/1.3555379.

[86] M. Butkus, K. G. Wilcox, J. Rautiainen, O. G. Okhotnikov, S. S. Mikhrin, I. L. Krestnikov, A. R. Kovsh, M. Hoffmann, T. Südmeyer, U. Keller, and E. U. Rafailov. "High-power quantum-dot-based semiconductor disk laser". In: *Optics Letters* 34 (June 2009), p. 1672. DOI: 10.1364/OL.34.001672.

[87] T. D. Germann, A. Strittmatter, U. W. Pohl, D. Bimberg, J. Rautiainen, M. Guina, and O. G. Okhotnikov. "Quantum-dot semiconductor disk lasers". In:

Journal of Crystal Growth 310.23 (2008), pp. 5182–5186. DOI: 10.1016/j.jcrysgro.2008.07.004.

[88] Y. Kaneda, J. M. Yarborough, L. Li, N. Peyghambarian, L. Fan, C. Hessenius, M. Fallahi, J. Hader, J. V. Moloney, Y. Honda, M. Nishioka, Y. Shimizu, K. Miyazono, H. Shimatani, M. Yoshimura, Y. Mori, Y. Kitaoka, and T. Sasaki. "Continuous-wave all-solid-state 244 nm deep-ultraviolet laser source by fourth-harmonic generation of an optically pumped semiconductor laser using $CsLiB_6O_{10}$ in an external resonator". In: *Optics Letters* 33.15 (July 2008), p. 1705. DOI: 10.1364/ol.33.001705.

[89] Y. Kaneda, J. M. Yarborough, Y. Merzlyak, A. Yamaguchi, K. Hayashida, N. Ohmae, and H. Katori. "Continuous-wave, single-frequency 229 nm laser source for laser cooling of cadmium atoms". In: *Optics Letters* 41.4 (Feb. 2016), p. 705. DOI: 10.1364/OL.41.000705.

[90] J. Rautiainen, I. Krestnikov, J. Nikkinen, and O. G. Okhotnikov. "2.5 W orange power by frequency conversion from a dual-gain quantum-dot disk laser". In: *Optics Letters* 35 (June 2010), p. 1935. DOI: 10.1364/OL.35.001935.

[91] D. C. Parrotta, A. J. Kemp, M. D. Dawson, and J. E. Hastie. "Multiwatt, Continuous-Wave, Tunable Diamond Raman Laser With Intracavity Frequency-Doubling to the Visible Region". In: *IEEE Journal of Selected Topics in Quantum Electronics* 19.4 (July 2013), pp. 1400108–1400108. DOI: 10.1109/jstqe.2013.2249046.

[92] D. C. Parrotta, R. Casula, J.-P. Penttinen, T. Leinonen, A. J. Kemp, M. Guina, and J. E. Hastie. "InGaAs-QW VECSEL emitting >1.300-nm via intracavity Raman conversion". In: *Vertical External Cavity Surface Emitting Lasers (VECSELs) VI*. Ed. by K. G. Wilcox. SPIE, Mar. 2016. DOI: 10.1117/12.2217593.

[93] J. Lin, H. M. Pask, D. J. Spence, C. J. Hamilton, and G. P. A. Malcolm. "Continuous-wave VECSEL Raman laser with tunable lime-yellow-orange output". In: *Optics Express* 20.5 (Feb. 2012), p. 5219. DOI: 10.1364/oe.20.005219.

[94] J. L. A. Chilla, S. D. Butterworth, A. Zeitschel, J. P. Charles, A. L. Caprara, M. K. Reed, and L. Spinelli. "High-power optically pumped semiconductor lasers". In: *Solid State Lasers XIII: Technology and Devices*. Ed. by R. Scheps and H. J. Hoffman. Vol. 5332. SPIE, July 2004, pp. 143–150. DOI: 10.1117/12.549003.

[95] E. Kantola, T. Leinonen, S. Ranta, M. Tavast, and M. Guina. "High-efficiency 20 W yellow VECSEL". In: *Optics Express* 22.6 (2014), pp. 77–81. DOI: 10.1364/OE.22.006372.

[96] S. S. Beyertt, M. Zorn, T. Kübler, H. Wenzel, M. Weyers, A. Giesen, G. Tränkle, and U. Brauch. "Optical in-well pumping of a semiconductor disk laser with high optical efficiency". In: *IEEE Journal of Quantum Electronics* 41.12 (2005), pp. 1439–1449. DOI: 10.1109/JQE.2005.858794.

[97] F. Demaria, S. Lorch, S. Menzel, M. Riedl, F. Rinaldi, R. Rosch, and P. Unger. "Design of highly-efficient high-power optically-pumped semiconductor disk lasers". In: *IEEE Journal of Selected Topics in Quantum Electronics* 15.3 (May 2009), p. 5. DOI: 10.1109/islc.2008.4636048.

[98] L. Fan, M. Fallahi, J. T. Murray, R. Bedford, Y. Kaneda, A. R. Zakharian, J. Hader, J. V. Moloney, W. Stolz, and S. W. Koch. "Tunable high-power high-brightness linearly polarized vertical-external-cavity surface-emitting lasers". In: *Applied Physics Letters* 88.2 (2006), pp. 1–3. DOI: 10.1063/1.2164921.

[99] L. Fan, C. Hessenius, M. Fallahi, J. Hader, H. Li, J. V. Moloney, W. Stolz, S. W. Koch, J. T. Murray, and R. Bedford. "Highly strained InGaAsGaAs multiwatt vertical-external-cavity surface-emitting laser emitting around 1170 nm". In: *Applied Physics Letters* 91.13 (2007), pp. 2005–2008. DOI: 10.1063/1.2790838.

[100] A. Garnache, A. A. Kachanov, F. Stoeckel, and R. Houdré. "Diode-pumped broadband vertical-external-cavity surface-emitting semiconductor laser applied to high-sensitivity intracavity absorption spectroscopy". In: *Journal of the Optical Society of America B* 17.9 (2000), pp. 1589–1598. DOI: 10.1364/JOSAB.17.001589.

[101] K. S. Kim, J. R. Yoo, S. H. Cho, S. M. Lee, S. J. Lim, J. Y. Kim, J. H. Lee, T. Kim, and Y. J. Park. "1060 nm vertical-external-cavity surface-emitting lasers with an optical-to-optical efficiency of 44% at room temperature". In: *Applied Physics Letters* 88.9, 091107 (Feb. 2006), p. 091107. DOI: 10.1063/1.2181272.

[102] A. Laurain, M. Myara, G. Beaudoin, I. Sagnes, and A. Garnache. "Multiwatt-power highly-coherent compact single-frequency tunable vertical-external-cavity-surface-emitting-semiconductor-laser." In: *Optics Express* 18.14 (June 2010), pp. 14627–14636. DOI: 10.1364/OE.18.014627.

[103] A. Laurain, C. Mart, J. Hader, J. V. Moloney, B. Kunert, and W. Stolz. "15 W Single Frequency Optically Pumped Semiconductor Laser With Sub-Megahertz Linewidth". In: *IEEE Photonics Technology Letters* 26.2 (Jan. 2014), pp. 131–133. DOI: 10.1109/LPT.2013.2290062.

[104] S. Lutgen, T. Albrecht, P. Brick, W. Reill, J. Luft, and W. Späth. "8-W high-efficiency continuous-wave semiconductor disk laser at 1000 nm". In: *Applied Physics Letters* 82, 3620 (May 2003), p. 3620. DOI: 10.1063/1.1579137.

[105] A. Rantamaki, A. Chamorovskiy, J. Lyytikainen, and O. Okhotnikov. "4.6-W Single Frequency Semiconductor Disk Laser With <75-kHz Linewidth". In: *IEEE Photonics Technology Letters* 24.16 (Aug. 2012), pp. 1378–1380. DOI: 10.1109/lpt.2012.2204736.

[106] B. Rudin, A. Rutz, M. Hoffmann, D. J. Maas, A.-R. Bellancourt, E. Gini, T. Südmeyer, and U. Keller. "Highly efficient optically pumped vertical-emitting semiconductor laser with more than 20 W average output power in a fundamental transverse mode". In: *Optics Letters* 33 (Nov. 2008), p. 2719. DOI: 10.1364/OL.33.002719.

[107] T.-L. Wang, Y. Kaneda, J. M. Yarborough, J. Hader, J. V. Moloney, A. Chernikov, S. Chatterjee, S. W. Koch, B. Kunert, and W. Stolz. "High-Power Optically Pumped Semiconductor Laser at 1040 nm". In: *IEEE Photonics Technology Letters* 22 (May 2010), pp. 661–663. DOI: 10.1109/LPT.2010.2043731.

[108] E. G. H. Lindberg M. Strassner and A. Larsson. "0.8 W optically pumped vertical external cavity surface emitting laser operating CW at 1550 nm". In: *Electronics Letters* 40.10 (May 2004), pp. 601–602. DOI: 10.1049/el:20040435.

[109] P. J. Schlosser, J. E. Hastie, S. Calvez, A. B. Krysa, and M. D. Dawson. "InP/AlGaInP quantum dot semiconductor disk lasers for CW TEM_00 emission at 716 - 755 nm". In: *Optics Express* 17 (Nov. 2009), p. 21782. DOI: 10.1364/OE.17.021782.

[110] T. Schwarzbäck, R. Bek, F. Hargart, C. A. Kessler, H. Kahle, E. Koroknay, M. Jetter, and P. Michler. "High-power InP quantum dot based semiconductor disk laser exceeding 1.3 W". In: *Applied Physics Letters* 102.9, 092101 (Mar. 2013), p. 092101. DOI: 10.1063/1.4793299.

[111] M. Rahim, M. Arnold, F. Felder, K. Behfar, and H. Zogg. "Midinfrared lead-chalcogenide vertical external cavity surface emitting laser with 5 µm wavelength". In: *Applied Physics Letters* 91.15 (2007), pp. 83–86. DOI: 10.1063/1.2798254.

[112] S. Galtier, F. Nez, L. Julien, and F. Biraben. "Ultraviolet continuous-wave laser source at 205 nm for hydrogen spectroscopy". In: *Optics Communications* 324 (Aug. 2014), pp. 34–37. DOI: 10.1016/j.optcom.2014.03.018.

[113] M. C. Storrie-Lombardi, W. F. Hug, G. D. McDonald, A. I. Tsapin, and K. H. Nealson. "Hollow cathode ion lasers for deep ultraviolet Raman spectroscopy and fluorescence imaging". In: *Review of Scientific Instruments* 72.12 (Dec. 2001), pp. 4452–4459. DOI: 10.1063/1.1369627.

[114] K. Devi, S. Parsa, and M. Ebrahim-Zadeh. "Continuous-wave, single-pass, single-frequency second-harmonic-generation at 266 nm based on birefringent-multicrystal scheme". In: *Optics Express* 24.8 (2016), p. 8763. DOI: 10.1364/OE.24.008763.

[115] S. Sayama and M. Ohtsu. "Tunable UV CW generation by frequency tripling of a Ti:sapphire laser". In: *Optics Communications* 137.4-6 (May 1997), pp. 295–298. DOI: 10.1016/S0030-4018(96)00799-7.

[116] F. Huang, Q. Lou, T. Yu, J. Dong, B. Lei, and Y. Wei. "Tunable solid state UV laser". In: *Optics & Laser Technology* 33.2 (Mar. 2001), pp. 111–115. DOI: 10.1016/S0030-3992(00)00128-6.

[117] X. Zhang, Z. Wang, G. Wang, Y. Zhu, Z. Xu, and C. Chen. "Widely tunable and high-average-power fourth-harmonic generation of a Ti:sapphire laser with a KBBOF prism-coupled device". In: *Optics Letters* 34.9 (May 2009), p. 1342. DOI: 10.1364/OL.34.001342.

[118] J. Sakuma, Y. Asakawa, T. Sumiyoshi, and H. Sekita. "High-Power CW Deep-UV Coherent Light Sources Around 200 nm Based on External Resonant Sum-Frequency Mixing". In: *IEEE Journal of Selected Topics in Quantum Electronics* 10.6 (Nov. 2004), pp. 1244–1251. DOI: 10.1109/JSTQE.2004.837711.

[119] D. J. Berkeland, F. C. Cruz, and J. C. Bergquist. "Sum-frequency generation of continuous-wave light at 194 nm". In: *Applied Optics* 36.18 (June 1997), p. 4159. DOI: 10.1364/AO.36.004159.

[120] N. Ruhnke, A. Müller, B. Eppich, R. Güther, M. Maiwald, B. Sumpf, G. Erbert, and G. Tränkle. "Single-pass UV generation at 222.5 nm based on high-power GaN external cavity diode laser". In: *Optics Letters* 40.9 (May 2015), p. 2127. DOI: 10.1364/OL.40.002127.

[121] A. Rahimi-Iman. "Recent advances in VECSELs". In: *Journal of Optics* 18.9 (Sept. 2016), p. 093003. DOI: 10.1088/2040-8978/18/9/093003.

[122] R. S. Craxton. "Theory of high efficiency third harmonic generation of high power Nd-glass laser radiation". In: *Optics Communications* 34.3 (Sept. 1980), pp. 474–478. DOI: 10.1016/0030-4018(80)90420-4.

[123] R. Wu. "High-efficiency and compact blue source: intracavity frequency tripling by using LBO and BBO without the influence of birefringence". In: *Applied Optics* 32.6 (Feb. 1993), p. 971. DOI: 10.1364/AO.32.000971.

[124] Z. Sun, R. Li, Y. Bi, X. Yang, Y. Bo, W. Hou, X. Lin, H. Zhang, D. Cui, and Z. Xu. "Generation of 4.3-W coherent blue light by frequency-tripling of a side-

pumped Nd:YAG laser in LBO crystals". In: *Optics Express* 12.26 (2004), p. 6428. DOI: 10.1364/OPEX.12.006428.

[125] B.-T. Zhang, H.-T. Huang, J.-F. Yang, J.-L. He, C.-H. Zuo, J.-L. Xu, X.-Q. Yang, and S. Zhao. "Generation of 7.8W at 355nm from an efficient and compact intracavity frequency-tripled Nd:YAG laser". In: *Optics Communications* 283.11 (June 2010), pp. 2369–2372. DOI: 10.1016/j.optcom.2010.01.067.

[126] H. Kahle, C. M. N. Mateo, U. Brauch, R. Bek, T. Schwarzbäck, M. Jetter, T. Graf, and P. Michler. "Gain chip design, power scaling and intra-cavity frequency doubling with LBO of optically pumped red-emitting AlGaInP-VECSELs". In: *SPIE 9734*. Vol. 49. Mar. 2016. DOI: 10.1117/12.2209305.

[127] Q.-z. Shu, A. L. Caprara, J. D. Berger, D. W. Anthon, H. Jerman, and L. Spinelli. "Intracavity-tripled optically-pumped semiconductor laser at 355 nm". In: *Lasers and Applications in Science and Engineering*. Ed. by W. A. Clarkson, N. Hodgson, and R. K. Shori. Vol. 7193. San Jose: SPIE, Feb. 2009, p. 719319. DOI: 10.1117/12.816073.

[128] D. Yu, C. Dong, L. Zhang, M. Cheng, L. Hu, Y. Du, Q. Zhu, and C. Zhang. "Resonant two-photon ionization spectroscopy of the ^{35}Cl and ^{37}Cl isotopomers of cis and trans 3-chloro-4-fluoroanisole". In: *Journal of Molecular Structure* 1000.1-3 (Aug. 2011), pp. 92–98. DOI: 10.1016/j.molstruc.2011.05.058.

[129] M. N. Fiddler, I. Begashaw, M. A. Mickens, M. S. Collingwood, Z. Assefa, and S. Bililign. "Laser Spectroscopy for Atmospheric and Environmental Sensing". In: *Sensors* 9.12 (Dec. 2009), pp. 10447–10512. DOI: 10.3390/s91210447.

[130] C. Schulz, V. Sick, J. Heinze, and W. Stricker. "Laser-induced-fluorescence detection of nitric oxide in high-pressure flames with A–X(0, 2) excitation". In: *Applied Optics* 36.15 (May 1997), p. 3227. DOI: 10.1364/AO.36.003227.

[131] K. Niemi, V. S.-v. der Gathen, and H. F. Döbele. "Absolute calibration of atomic density measurements by laser-induced fluorescence spectroscopy with two-photon excitation". In: *Journal of Physics D: Applied Physics* 34.15 (Aug. 2001), pp. 2330–2335. DOI: 10.1088/0022-3727/34/15/312.

[132] K. Niemi, V. S.-v. D. Gathen, and H. F. Döbele. "Absolute atomic oxygen density measurements by two-photon absorption laser-induced fluorescence spectroscopy in an RF-excited atmospheric pressure plasma jet". In: *Plasma Sources Science and Technology* 14.2 (May 2005), pp. 375–386. DOI: 10.1088/0963-0252/14/2/021.

[133] W. S. Fann, R. Storz, H. W. K. Tom, and J. Bokor. "Direct measurement of nonequilibrium electron-energy distributions in subpicosecond laser-heated gold films". In: *Physical Review Letters* 68.18 (May 1992), pp. 2834–2837. DOI: 10.1103/PhysRevLett.68.2834.

[134] A. Laurain, M. Scheller, and P. Polynkin. "Low-Threshold Bidirectional Air Lasing". In: *Physical Review Letters* 113.25 (Dec. 2014), p. 253901. DOI: 10.1103/PhysRevLett.113.253901.

[135] R. J. Drost and B. M. Sadler. "Survey of ultraviolet non-line-of-sight communications". In: *Semiconductor Science and Technology* 29.8 (June 2014), p. 084006. DOI: 10.1088/0268-1242/29/8/084006.

[136] D. Kedar. "Subsea ultraviolet solar-blind broadband free-space optics communication". In: *Optical Engineering* 48.4 (Apr. 2009), p. 046001. DOI: 10.1117/1.3120482.

[137] S. Arnon and D. Kedar. "Non-line-of-sight underwater optical wireless communication network". In: *Journal of the Optical Society of America A* 26.3 (Mar. 2009), p. 530. DOI: 10.1364/JOSAA.26.000530.

CHAPTER 2

Semiconductor Disk Lasers

2.1 Introduction

A semiconductor disk laser (SDL) consists of a semiconductor gain mirror and an external laser cavity. The semiconductor gain mirror is composed of a highly reflective Bragg mirror and an active region, usually based on quantum wells. The external laser cavity can be designed to target various operating regimes, e.g. single frequency or passively-modelocked short pulse operation, but must be high finesse: SDLs are low gain devices and as such do not tolerate high losses. Having the laser cavity external to the semiconductor structure allows for laser customisation via cavity distances, mirrors and intracavity elements, which greatly increases the flexibility of this device. SDLs are usually optically pumped, not requiring any doping of the semiconductor materials. Both pumping and laser oscillation happen perpendicular to the plane of the semiconductor layers, referred to as the vertical direction with respect to epitaxial growth. Another name for this device that reflects the aforementioned characteristics is vertical-external-cavity surface-emitting laser, or VECSEL.

2.2 Design

SDL gain structures are epitaxially grown on a suitable semiconductor substrate by microfabrication techniques such as metal organic chemical vapour deposition or molecular-beam epitaxy. The general laser architecture is shown in figure 2.1. The DBR and active region are grown using material compositions matching the lattice constant of the substrate (although a small amount of strain may be desired in the gain region as will be explained later on). A layer to confine the electrons within the gain region is needed and, depending on its composition (e.g. aluminium may be used to increase the bandgap), a capping layer will be added to prevent oxidation.

The order in which the DBR and gain region are grown over the substrate usually depends on the technique to be used for thermal management (see section 2.2.4). For example, our samples are grown with the DBR deposited on the substrate first and the gain region on top. With this distribution, if the DBR material is not a good thermal conductor, or its required thickness results in a significant thermal resistance, heat can be extracted directly from the gain region using a transparent bonded heatspreader on top of the structure. Since the route for heat extraction is through the top of the structure this growth order eliminates the need for sample post processing, as removal of the substrate is not required.

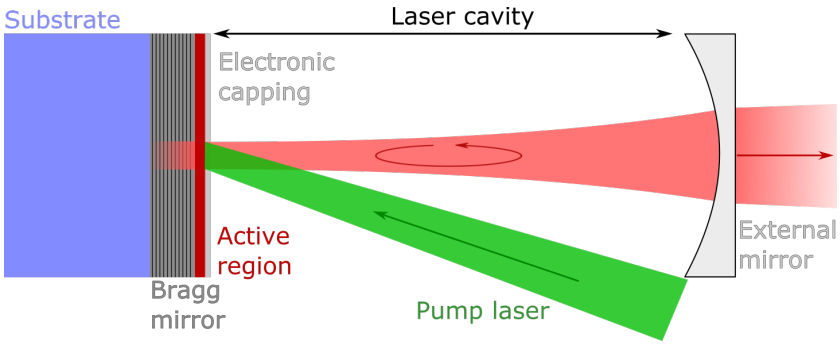

Figure 2.1: Schematic of a semiconductor disk laser.

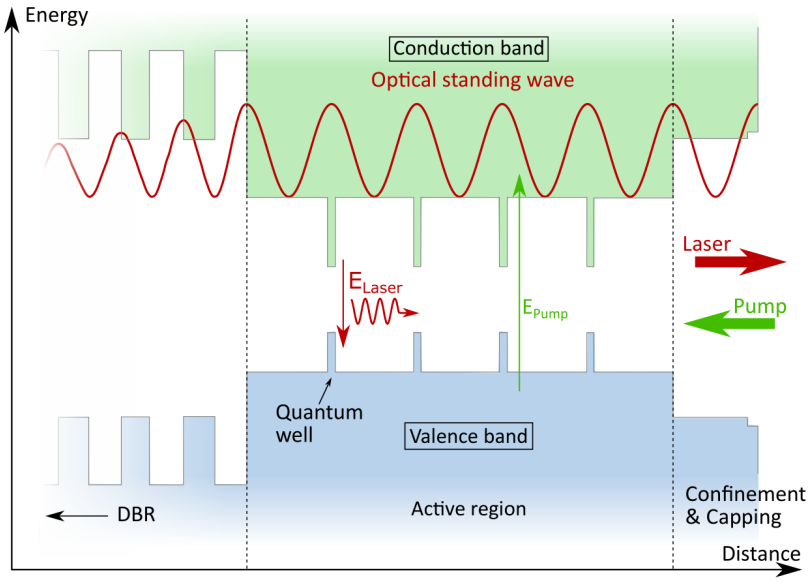

Figure 2.2: Semiconductor bandgap diagram of a typical SDL gain structure featuring the different layers described in the text (DBR, active region and capping). Pump absorption occurs in the barriers and laser emission happens from quantum wells. The quantum wells are positioned at the antinodes of the standing wave, in RPG configuration, as described in the text. Illustration from Jones [5].

2.2.1 Active region

The active region of an SDL (figure 2.2) consists of several quantum wells, separated by barriers, with a total thickness enough to absorb most of the pump power [1, 2]. The emitted light is totally reflected at the DBR and partially reflected at the air interface, effectively creating a subcavity within the gain region and giving rise to a standing wave. In order to maximize laser gain, the active region should be designed so the quantum wells are positioned at the antinodes of such standing wave, in what is known as resonant periodic gain configuration (RPG) [3]. The confinement window, transparent for the pump and laser wavelengths, acts as an electronic barrier to confine the carriers and prevents their loss through the surface via non-radiative recombination [4].

The thickness of this confinement window can be chosen so the Fabry-Perot subcavity between the semiconductor surface and the DBR matches a resonant design for increased gain and reduced threshold, but an anti-resonant configuration (subcavity odd multiple of $\lambda/4$) may be preferred for increased gain bandwidth, e.g. for short pulse modelocking [4, 6]. These designs correspond to the chip surface at, respectively, an antinode or a node of the optical field. Resonant configuration increases the effective gain, which in turn increases tolerance to losses, allowing for higher output couplers or more intracavity elements. At the same time, this configuration narrows the gain bandwidth, reducing the tuning range of the laser. Anti-resonant configuration, on the other hand, maximizes the tuning range, but with no gain enhancement the threshold is higher and loss tolerance decreases. The field node at the chip surface reduces scattering losses caused by on-surface dust deposition, while this scattering is maximized with resonant configuration. Further details can be found here [6] and here [7].

Generally SDLs are designed so pump absorption occurs in the barriers. Since the energy difference between the quantum wells and the barriers must be enough to confine the electrons, this sets a lower limit to the minimum quantum defect possible (i.e. the difference between pump and emission photon energies). During laser operation, this energy difference is translated into heat and must be taken into account when designing the SDL. In order to minimise the quantum defect (and thus the pump-induced temperature increase), in-well absorption devices have also been demonstrated [8–10]. Given the short length of the quantum wells, in-well absorption requires multi-pass systems to achieve efficient pump absorption. This would set another condition for the DBR, now required to reflect the pump wavelength as well as the emission wavelength [9], adding complexity to the design and manufacture of this part of the structure. Barrier pumping therefore simplifies the design, while the extra heat is still controllable. When designing the SDL structure care must be taken to ensure nearly all the pump will be absorbed by the barriers, making use of all the available power and minimising the pump that reaches the DBR (where it is absorbed, depositing heat).

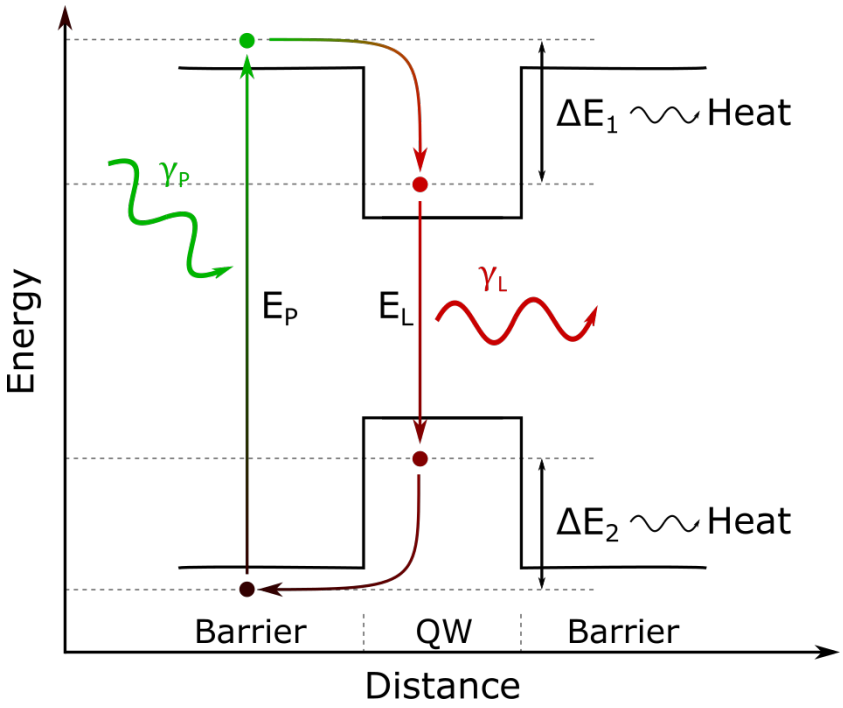

Figure 2.3: Pump absorption and laser emission energy diagram. The photon γ_P (with energy E_P) is absorbed at the barrier, promoting an electron from the valence band to the conduction band. Said electron falls into the quantum well, losing some energy non-radiatively. When the electron then falls back to the valence band, a photon (γ_L) is emitted, with energy E_L.

The laser process in terms of photon – electron interaction is described in figure 2.3. The carriers produced in the barriers when pump photons are absorbed diffuse to the lower energy quantum wells. The electrons trapped in a quantum well are distributed in quantized energy levels that can be obtained by solving Schrödinger's equation for a finite quantum well. The composition of the quantum wells has to be chosen so the bandgap energy matches closely the energy of the emission we would like to achieve, although temperature effects also have to be taken into account when designing the device. As fermions, electrons in the conduction band (and holes in the valence band) follow the Fermi-Dirac distribution which, together with the density of available states, gives a range of possible transition energies that correspond to a broad range of wavelengths. It is this carrier distribution that gives SDLs the capability of wide wavelength tuning. As explained before, the tuning range can be enhanced by means of an antiresonant design of the chip microcavity.

Since gain occurs in the quantum wells, and a typical SDL will only have around a dozen of nanometre-thick quantum wells, the actual length over which gain takes place is generally on the order of a hundred nanometres. SDLs are thus low gain devices, which tolerate very few intracavity losses. For this reason optimum output coupling is usually under 10 %. As a result, the intracavity fields are on the order of tens, if not hundreds or even thousands of Watts. The strong magnitude of the intracavity fields suits the requirement of several nonlinear processes, in particular frequency conversion (either second or third order). The low optimum output coupling corresponds to easily achievable nonlinear conversion factors. SDLs have proven to be excellent devices for nonlinear frequency conversion [11–13].

2.2.2 Quantum wells as gain medium

As introduced in Chapter 1, quantum wells present many improvements over bulk semiconductors as laser gain media, such that semiconductor LEDs and lasers are now almost entirely QW-based devices (with even increased confinement, e.g. quantum dots, also now very common –e.g. [14]–). These advantages are:

- The quantum confinement inside the quantum wells keeps the density of states of electrons and holes localized near the band edges. At the same time, the degeneracy between the valence band states (heavy hole band and light hole band [15]) is removed and the probability of non-radiative transitions (such as Auger recombination) is reduced [16]. This lowers the carrier density required for population inversion, lowering the laser threshold.

- Confining the electrons favours certain optical transitions, increasing the gain and allowing polarization sensitive devices [17]. Quantum wells also trap electrons better than bulk semiconductors, reducing leakage currents.

- The transition energy between conduction and valence band can be fine-tuned by adjusting the width of the quantum wells, providing a method to tailor specific wavelength ranges maintaining the same semiconductor material. This is on top of the straightforward modification of the energy bandgap by modifying the semiconductor components, also possible in bulk devices.

- Since the thickness of the quantum wells is so small (<10 nm) strain can be easily accommodated by the structure, maintaining good growth quality [18]. This allows for a wider range of semiconductor alloys to be used and, in addition, modification of the valence band structure, that can make the heavy hole band symmetrical to the conduction band, thus further reducing the threshold. At the same time the separation between heavy hole and light hole bands increases [19].

Strain

During epitaxial growth, each layer deposited must match the lattice spacing of the substrate. If the intrinsic lattice constant of the deposited material, a, is different from the substrate lattice constant, a_0, the new layer will be under strain; compressive strain for $a > a_0$, tensile strain for $a < a_0$. Small amounts of strain can be accommodated elastically; however, once the strained layer reaches a critical thickness, as defined by Matthews and Blakeslee [18], misfit dislocations start to form and crystal break becomes more probable. Some amount of controlled strain may however be desirable, as suggested by Adams [16] and Yablonovitch and Kane [20]. Small amounts of strain can produce several advantages, such as reducing the effective mass in the valence band and polarising the gain to match the orientation of the laser cavity. Where strained layers must be incorporated in a heterostructure, strain compensation may be used to minimise the stress over the whole structure [21] by balancing tensile and compressive strain layers.

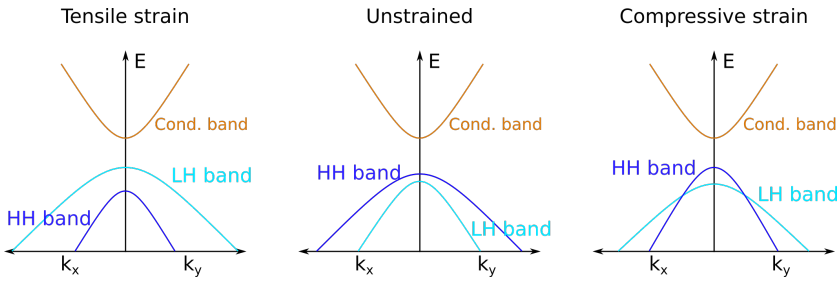

Figure 2.4: Simplified band geometry in a quantum well semiconductor, featuring the heavy hole and light hole bands distortion caused by tensile and compressive strain, compared to the unstrained case.

The band structure of a bulk semiconductor is usually very complex, but around the (direct) bandgap there are three bands especially relevant, as depicted in figure 2.4. One is the conduction band, made of s orbitals, that gets populated by excited electrons. The valence band, made of p orbitals, is composed by the so called heavy hole and light hole sub-bands, degenerated at the Brillouin zone centre for bulk semiconductors. This degeneracy is lifted by the carrier confinement in a quantum well. A third valence sub-band, called the split-off band, will not be considered here. As shown in figure 2.4, for unstrained quantum wells the heavy hole band is the ground state and, as the carrier dispersion depends on effective mass, does not match the conduction band. At lower energy, the light hole band does, on the other hand, present close symmetry to the conduction band. Compressive strain can modify the band geometry to achieve close symmetry between the conduction band and the heavy hole band near the band edge.

Conduction and valence band symmetry is of paramount importance for laser threshold. Since the density of states in QWs is proportional to the carriers' effective mass, the density of states at the top of the valence band will be in general much higher than at the bottom of the conduction band, thus more carriers must be injected to achieve population inversion. Strain modifies the valence band geometry (i.e. the effective mass of the holes) so the heavy hole band can be taken closer to symmetry with the conduction band, thus reducing the number of carriers required to achieve population inversion and thus lowering laser threshold.

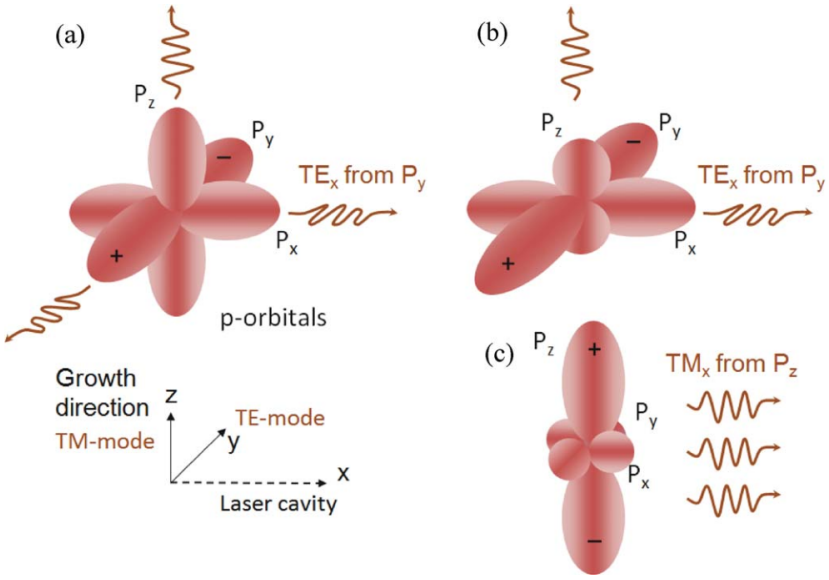

Figure 2.5: TE and TM emission as a result of conduction band electrons recombining with valence band holes in p-orbitals for unstrained (a), compressive (b) and tensile (c) strain. Adapted from Adams [17].

Since carrier distribution in quantum wells is not symmetric in k-space, selection rules favour some optical transitions over others. In particular, stimulated absorption / emission between the conduction band and the heavy hole band is only allowed if the electric field has a component in the plane of the quantum well (transverse electric field, TE). In the same way, transitions to the light hole band are allowed for both transverse electric and transverse magnetic (TM) modes, with TM transitions being stronger than TE transitions. Strain can modify the band structure to favour transitions to a certain band allowing, together with selection rules, for devices to be designed to work for a certain polarization of the light, as represented in figure 2.5 [17]. Since SDLs are vertically-emitting lasers, TE transitions result in unpolarised emission.

In particular, our compressive strained samples favour electronic transitions from conduction band to heavy hole band, increasing the gain at TE mode. The emission polarisation is however not defined by this design, since both X and Y polarisations contribute to the emission in the Z direction (part (b) of figure 2.5).

2.2.3 DBR

A distributed Bragg reflector is a dielectric mirror capable of very high reflectivity (over 99.9 %) for a narrow range around a central wavelength ($\lambda_0 \pm 5\%\lambda_0$) [22]. The mirror is made of several layers of two alternating dielectric materials, transparent for the desired wavelength and with different refractive indices (e.g. AlAs/AlGaAs), as depicted in figure 2.6. Each layer has a thickness of a quarter wavelength so, considering that reflections occurring at the interface between lower and higher refractive index (and not in reverse order) suffer a π phase shift, the reflections from all layers add up in phase. Designing a high quality DBR requires finding the correct material composition so the index contrast over a particular number of layers provides near perfect reflection of the laser wavelength. At the same time, the lattice constant must match that of the substrate to avoid strain tensions.

As can be seen in figure 2.7, alternating for example AlAs / GaAs layers provides a large refractive index contrast while the lattice constant remains practically unchanged. These two materials, or their compounds, are probably the most common choices for visible and near infrared SDLs. The materials available for deeper IR emission (e.g. $\sim$2 µm) present larger lattice constants, and antimony compounds usually take predominance.

Given the low gain of SDL devices (due to the nanometre-thick gain length), close to 100 % reflectivity is necessary for every non output coupler mirror in order to achieve threshold. DBRs thus provide the required high reflectivity, and its monolithic growth embedded into the semiconductor structure implies no post-processing (such as adding HR coatings) is needed in this respect. With this geometry, the structure will commonly be positioned as an end mirror of the laser cavity, although other schemes have also been demonstrated [25, 26]. Overall, DBR design is a challenging process that has often limited the development of SDLs in a broader range of materials (e.g. [27]).

(a)

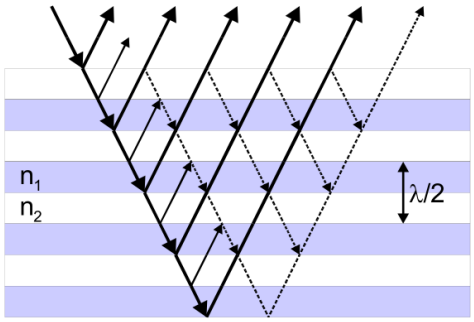

(b)

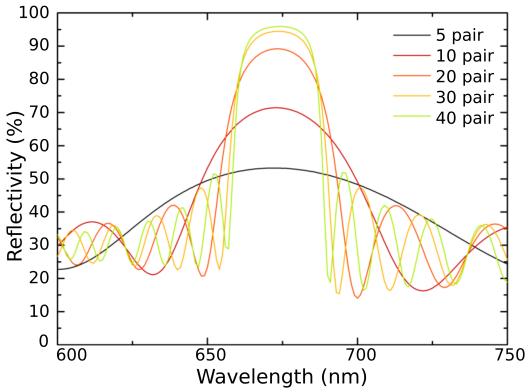

Figure 2.6: DBR alternating layers (a) and corresponding reflectivity (b). Images from [5, 23].

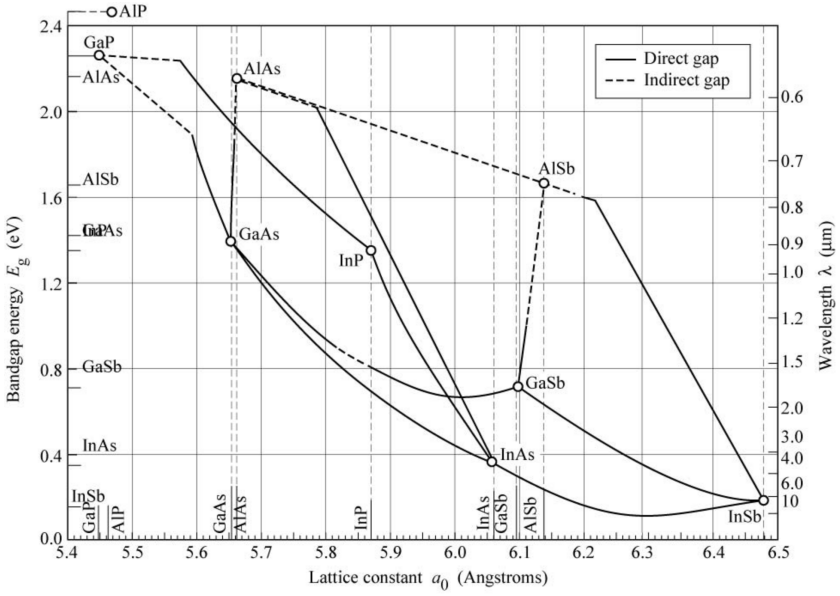

Figure 2.7: Bandgap energies and lattice constants of various III-V semiconductors at room temperature. Image from [24].

2.2.4 Thermal management

As in other solid state lasers, the pump-induced temperature rise limits the efficiency of SDLs, and therefore heat extraction is critical in these devices. As one increases the pump power, the temperature increases inside the active region and reduces the

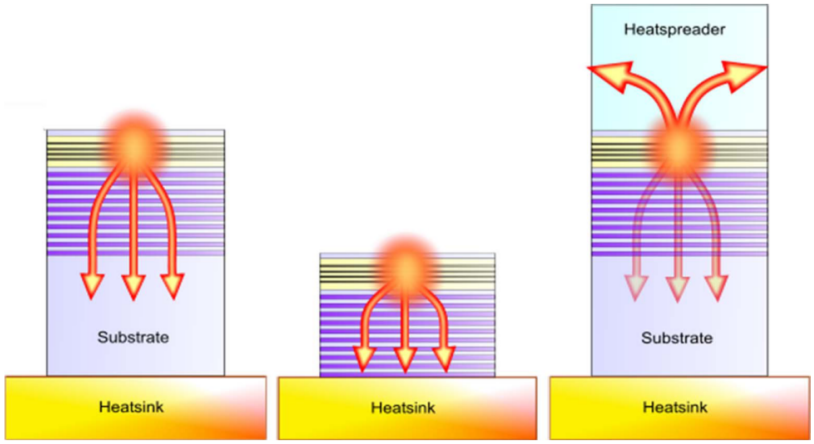

Figure 2.8: Comparison of different thermal management techniques. Considering the high thermal resistivity of our DBR, heat extraction from top by means of a heatspreader is preferred [28].

quantum well emission efficiency (carrier leakage increases with temperature). At the same time the bandgap is reduced, shifting the emission to longer wavelengths. Finally, the RPG wavelength and subcavity resonance are also shifted to longer wavelengths due to the change in the optical path. Since the mechanisms that govern the wavelength shift in the resonances and quantum well emission are different, it is no surprise that the shifting rate with temperature is different for both effects. It has already been described how a RPG design for a particular wavelength reduces threshold at that wavelength, which ideally matches the quantum well peak emission. Given the wavelength shift, SDLs have to be designed with temperature effects in mind, so the wavelength of the quantum well peak gain and the RPG will match at the desired pump power.

SDL gain structures are typically clamped in an actively cooled mount, but the extraction of the heat from the active region has being tackled in several ways, shown in figure 2.8. Simply clamping the chip in a mount means heat extraction occurs after passing through the DBR (and maybe the substrate depending on the growth order), which can present high thermal resistivity, thus reducing the efficiency of the cooling. For this reason the chip is sometimes treated to remove the substrate [29] so the active region is as close as possible to the heatsink. The main alternative to this method is using a transparent heatspreader with high thermal conductivity (e.g. sapphire, dia-

mond...) bonded to the chip surface [30, 31] so the heat is extracted from the top rather than from the bottom of the structure. This approach has proven to be very efficient at any wavelength, since it bypasses the thermal impedance of the DBR, while making post-processing unnecessary [28] and it is the preferred method in this work.

2.3 Characteristics of SDLs

2.3.1 Pump flexibility

SDLs are usually optically pumped, unlike other types of semiconductor lasers and similarly to conventional diode-pumped solid-state lasers. However, SDLs do not present the strict requirements of conventional lasers. The absorption length of a SDL can be shorter than a micrometre, effectively a single plane, thus reducing the requirements on the spatial brightness of the pump laser. Moreover, absorption takes place for pump energies above barrier bandgap energy, as opposed to the excitation of a particular electronic transition. Hence, SDLs do not require a pump with high spectral brightness either. Therefore the quality of the pump laser is not an important factor, and nevertheless the output of an SDL output can still offer high beam quality. In this respect, optically pumped SDLs convert poor quality pump lasers into a high quality output laser, in what can be thought as an effective mode converter [32].

2.3.2 Power scaling

SDL optical pumping simplifies power scaling: an increase in pump power should be accompanied by an increase in the pumped surface area of the semiconductor chip [33]. The external cavity can be adjusted for a larger beam spot at the SDL while maintaining excellent beam quality. At the same time optical intensity is never too high to induce

damage on the semiconductor chip. With this method heat is also distributed over a larger area for high pump powers, easing sample cooling.

Nevertheless, thermal effects on very large pump areas are still the main limitation towards higher output powers [28]: too large an increase of the temperature will detune the quantum wells and the RPG, causing a drop in the laser output in what is known as thermal rollover. The active region should therefore be designed with the maximum pump power in mind, so the subcavity resonance wavelength matches the quantum well peak emission avoiding this effect. Recent research has targeted thermal management and power scaling [34, 35], and over 100 W of output power in CW operation have previously been demonstrated [36].

2.3.3 Beam quality

One of the main advantages of SDLs is the high beam quality of the output, which can be achieved relatively simply thanks to the external optics and negligible thermal lensing inside the semiconductor [37]. The optics can be aligned to produce a circularly symmetric TEM_{00} mode, with near-diffraction-limited divergence. Beam quality factor (M^2) lower than 1.3 is a common standard for SDL builds. As this parameter is a measure of the similarity to a Gaussian beam, SDLs can be considered to produce a Gaussian profile under most approximations, which greatly simplifies any required calculation (starting from cavity design). When high power is preferred over beam quality, a trade-off is possible.

2.3.4 Wavelength flexibility

SDLs feature impressive wavelength flexibility: a single chip can generally be tuned over a range of $> 300\,\mathrm{cm}^{-1}$ ($\sim$9 THz) [38–40]. SDL design can also be adjusted to target different wavelengths with the same materials, via quantum well width, material

strain and composition. If on top of that we consider the different materials available for semiconductor emission, the actual coverage of SDLs by means of direct emission is impressive. To date, emission has been shown from 640 nm and extending through the near infrared [4, 41] (see figure 1.6), with pioneering demonstrations at wavelengths as short as 400 nm [42]. Nonlinear frequency up- and down-conversion, for which SDLs are particularly well suited, extends the fundamental coverage into the ultraviolet and far-infrared.

2.3.5 Pulsed operation

Due to the semiconductor character of the active region electron lifetimes in the excited states are very short (order of nanoseconds), making SDLs poor at energy storage in the gain region and not really suitable for Q-switching. An alternative method, however, is to store the energy in the laser cavity and achieve high power pulses via cavity dumping [43]. The wide bandwidth means SDLs are good candidates for modelocking [44, 45]. In order to reduce losses caused by spontaneous emission between pulses, the external cavities in these setups are usually designed to be as short as possible. While pulsed operation can be achieved by means of a pulsed pump (active modelocking), passive modelocking has also been carried out by means of a semiconductor saturable absorber mirror (SESAM) [46, 47], and recently a device integrating the active region and the saturable absorber, as well as the DBR, has been presented (MIXSEL) [48, 49]. Work in this topic has been extensive for the last 15 years and performance is rapidly increasing [50], showing so far pulses as short as ∼100 fs [51], repetition rates ∼50 GHz or 100 GHz with a MIXSEL [52, 53] and peak powers over 4 kW [54].

2.3.6 Narrow linewidth

Narrow linewidth single frequency operation in SDLs is almost as old as the device itself, having been demonstrated for the first time by Holm *et al.* in 1999 [55], where

rms frequency noise of 3 kHz over 3.5 s at 870 nm was demonstrated, achieved with active stabilization and making use of the external cavity to insert filtering optics (Lyot filter and etalon) to narrow the operating wavelength. The high-Q external cavity is very suitable for narrow, single frequency operation, and free-running laser linewidths down to 21 kHz have been demonstrated [56]. Active stabilization can be used to further narrow the linewidth while extending the sampling time, locking the laser frequency to an external reference, such as a stable Fabry-Perot cavity or spectroscopic feature. Several electronic stabilisation techniques are available (e.g. [57, 58]); the most common implementation for SDLs is to generate an error signal that can be applied to a piezoelectric cavity mounted mirror to provide fast feedback to the laser cavity. Moreover, high precision wavelength tuning has also been demonstrated, with tune steps on the order of picometres, together with narrow linewidth (11 kHz at 690 nm) operation [59].

2.3.7 Intracavity operation

Another advantage derived from the external cavity is ease of access to the intracavity beam (as opposed to common semiconductor monolithic lasers). It has already been mentioned how, being low gain devices due to the extremely short gain region, SDLs require high reflective mirrors, allowing only for a few percent transmission through the output coupler. A consequence is that optical power inside the cavity is generally very high, typically over 100 W, and specially with high pump power one can reach the kilowatt level [36].

We can make use of this intense intracavity field for several applications. In particular this thesis is focused on frequency conversion processes, which show a strong dependence on the intensity of the input fields (as will be described in the next chapter). This means higher input fields produce higher efficiency in the frequency conversion process. Often this is achieved by using pulsed lasers, but frequency conversion in continuous-wave operation requires complex setups to increase the otherwise low efficiency. By building

the system so the frequency conversion process takes place inside the laser cavity we can boost the conversion efficiency thanks to the enormous amounts of circulating optical power. Moreover, the conversion efficiency commonly takes values close to the optimum output coupling of the SDL systems, further extending the qualities of SDLs for intracavity frequency conversion.

As already mentioned, the external cavity also allows for saturable absorbers, absorption cells, or, very interestingly, intracavity optics such as birefringent filters (BRFs), etalons, gratings, etc., that increase the control we have over the longitudinal modes of the laser and its spectral frequency. For example, a BRF will be used in our system to narrow and tune the operating wavelength, while intracavity nonlinear crystals will produce frequency conversion.

2.3.8 Noise

SDLs are inherently low noise devices. Other solid-state lasers with long resonating cavities present dynamic fluctuations in the longitudinal mode structure, the so called green noise. This noise is accentuated in the presence of nonlinear harmonic generation due to direct dynamic interaction between different longitudinal modes in the nonlinear crystal. This problem appears in particular in the very common frequency doubling process from infrared laser output at 1064 nm to green emission at 532 nm, from which the name comes. The poor gain storage of SDLs due to the very short upper state lifetime (nanoseconds, opposed to the microseconds of other solid-state lasers) fixes the longitudinal modes, effectively removing the source of the problem [60].

2.4 Introduction to the experimental work

2.4.1 AlGaInP-based SDL for red emission

The samples used during this work are red emitting, GaInP-based SDL gain structures, designed in the Institute of Photonics at the University of Strathclyde and grown via MOCVD by Andrey Krysa at the EPSRC National Centre for III-V Semiconductors at the University of Sheffield. The design aimed to keep the structure as simple as possible, and no strain compensation was incorporated. They feature a resonant subcavity for improved effective gain.

The structure is grown on a GaAs substrate, which fixes the lattice constant just over 5.65 Å. The DBR structure that follows, maintaining this lattice constant, features 40 layers of alternating AlAs / $Al_{0.45}Ga_{0.55}As$ (with refractive indices of 3.07 and 3.5 respectively) for a total thickness of 4.2 µm. A simpler AlAs / GaAs design is not possible since the smaller GaAs bandgap (∼1.4 eV) means the laser photons would be absorbed by this material. This DBR structure presents high reflectivity for over 20 nm around a central wavelength of ∼675 nm at operational temperature.

The gain region consists of ten pairs of quantum wells, positioned at the antinodes of the optical field in RPG configuration as depicted in figure 2.9. The quantum wells are made of 6-nm-thick $Ga_{0.46}In_{0.54}P$ layers (bandgap ∼1.8 eV), sandwiched between $(Al_{0.6}Ga_{0.4})_{0.51}In_{0.49}P$ layers that act as barriers (bandgap ∼2.3 eV). The QW pairs are separated from each other by 82.5 nm thick barriers, plus 7-nm-thick separation between in-pair QWs. While the lattice constant of the barriers matches that of the substrate and DBR, it is marginally larger in the case of the QW layers, causing the quantum wells to be under compressive strain, favouring vertical TE emission.

The total thickness of the gain region is calculated to absorb all of the incident pump photons at 532 nm. As described in section 2.2.1, this approach makes use of the full

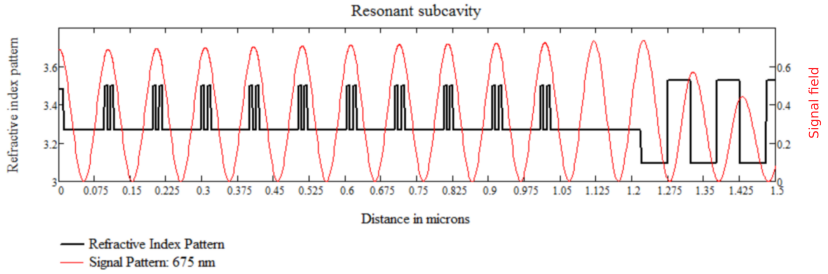

Figure 2.9: Structure of the gain region of our SDL showing the variation in refractive index with distance.

pump power while keeping the DBR design as simple as possible (no need to reflect the pump and no temperature increase caused by pump absorption). The absorption of the pump photons generates carriers in the conduction band that relax into the quantum wells. The QW thickness is chosen for emission at the design wavelength of around 675 nm at operating temperature. The pump is absorbed in the barriers, for an absorption length of ∼1 µm, while laser gain, which happens in the quantum wells, takes place within a total gain length of only 120 nm.

Lastly, an extra 86 nm barrier prevents non-radiative electronic recombination, and a 10 nm cap layer protects the active region from oxidation. The total thickness of the wafer is under 6 µm, most of which corresponds to the DBR.

The heatspreader used for thermal control, a 500-µm-thick diamond disk in our case, is bonded on top of the semiconductor structure, meaning it will be inside the laser cavity. The Fresnel losses the pump beam suffers when entering the semiconductor region are lowered by the inclusion of a diamond block given the lower refractive index ($n_{\text{diamond}} \sim 2.4$, $n_{\text{cap}} \sim 3.5$). The block can also act as a Fabry-Perot microcavity affecting the free spectral range of the laser if its surfaces are plano-parallel instead of wedged. Anti-reflection coatings have previously been used, but different diamonds with different coatings are needed for the various wavelengths we work with, greatly reducing the flexibility and increasing the costs of re-using the heatspreaders for other experimental set-ups.

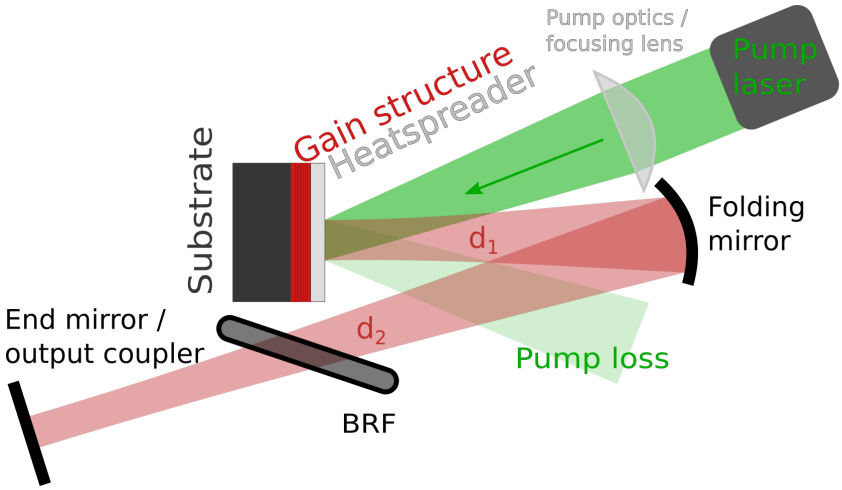

Figure 2.10: Schematic of the green-pumped AlGaInP SDL. The pump beam is steered around the SDL cavity folding mirror (angle exaggerated to stress the reflection loss).

2.4.2 Pump setup

The pump light is provided by a commercial Verdi laser that operates at 532 nm, offering up to 5.5 W of power working in continuous-wave. It consists of a diode pumped solid state laser (Nd:YVO_4) emitting at 1064 nm, frequency doubled to its second harmonic [61]. This pump source is nowadays being replaced by SDL based solutions [62], an example of the commercial applications of these multifaceted devices.

Considering the limitation that the pump beam (and its reflection) has to pass around the folding mirror of the SDL cavity, the angle of incidence is kept as small as possible. Due to the uncoated diamond heatspreader, approximately 18 % of the pump is reflected away from the SDL and lost, as seen in figure 2.10. This loss could be minimised via anti-reflection coating, but would mean each diamond would only suit one operational wavelength (inconvenient since our group works with different wavelengths); therefore, in order to present the performance of the SDL with respect to input power, future references to pump power take this loss into account, yielding a maximum input power of 4.51 W instead of the original 5.50 W.

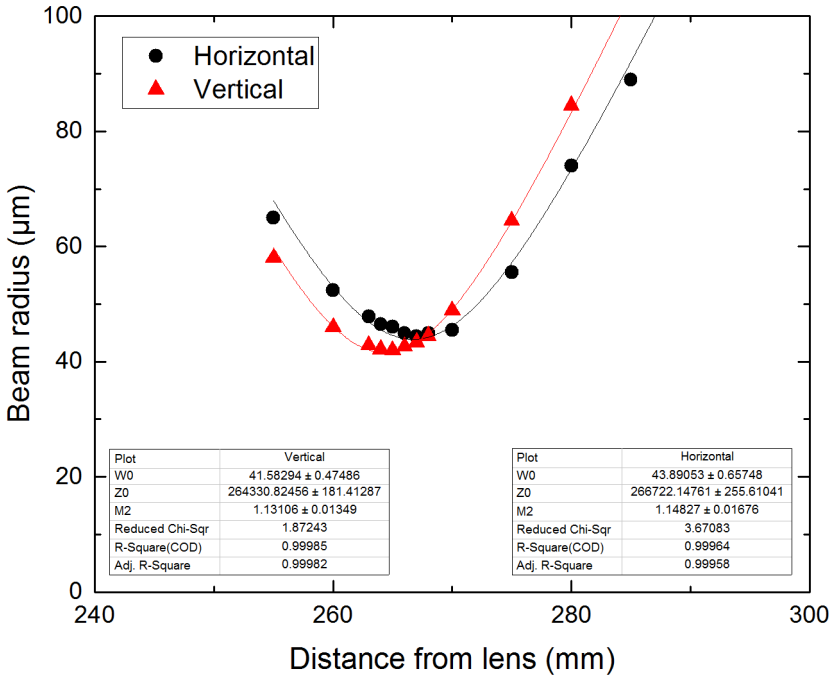

Figure 2.11: Pump focusing. The SDL sample will be positioned at the waist of the pump beam, ∼270 mm away from the focusing lens. The pump beam is focused to ∼44 µm (horizontal axis) and ∼42 µm (vertical axis).

The output of this pump laser is focused to a size of ∼43 µm radius by means of a 300 mm focusing lens. The M^2 fitting presented in figure 2.11 shows the measured beam radius for the horizontal and vertical axes. Both horizontal and vertical M^2 values are < 1.2, although there is a small separation in the longitudinal axis between both waists. As described earlier in this chapter, this is not a problem that would significantly affect the SDL beam quality since these semiconductor devices are not volume absorbers. The particular pump spot size is chosen so the SDL thermal rollover point roughly matches the maximum available pump power: a smaller size would result in reaching thermal rollover with lower pump powers (thus not being able to use all power available) while a larger size would mean higher threshold and lower maximum output power.

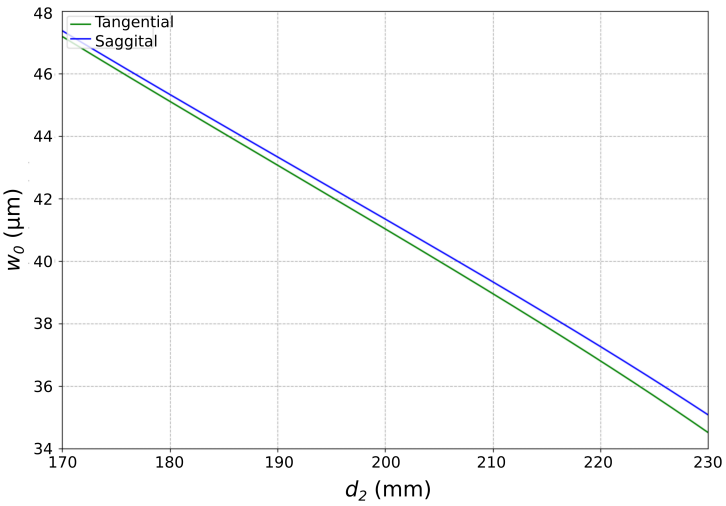

Figure 2.12: Calculated fundamental beam size at the SDL gain structure as a function of the length of the second arm of the laser cavity. The different horizontal and vertical components are caused by the angle in the folding mirror.

2.4.3 Three mirror cavity

The SDL sample has been characterised in a three mirror cavity, as previously sketched in figure 2.10, in order to investigate optimum mode-matching for the future tripling cavity design. This cavity has been designed so that altering distance d_2 modifies the intracavity beam size at the SDL (as seen in figure 2.12), since good agreement between pump spot size and laser intracavity mode size is mandatory for optimum laser operation (mode matching).

Measurement of the power leakage through an HR mirror for increasing distance d_2 shows that maximum power is achieved with a laser mode size of $\sim$41 µm (figure 2.13), which is just smaller than the pump beam size. This beam size ratio of $\sim$1 helps optimise both output power and beam quality. Pump sizes larger than the TEM_{00} mode size can trigger higher order transverse mode oscillation, with subsequent beam quality degradation; smaller pump sizes, on the other hand, ensure high beam quality with only fundamental mode oscillation, but cause higher threshold and lower maximum

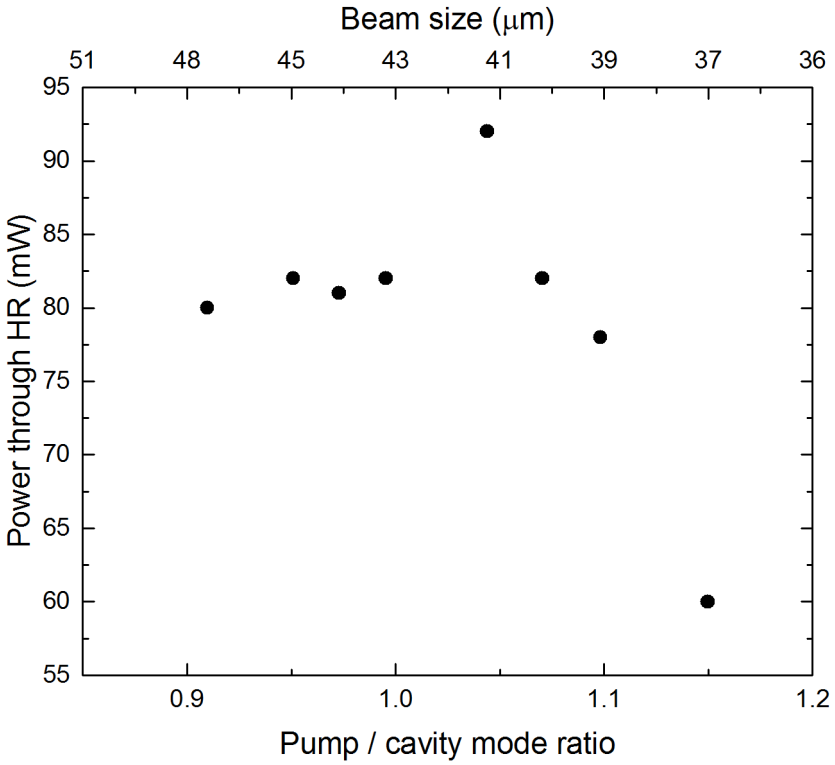

Figure 2.13: Fundamental power from HR leakage as a function of the pump / cavity mode ratio at the SDL gain structure. The pump size is ∼43 µm, as shown in figure 2.11. The maximum output power was achieved for a beam size of ∼41 µm.

output power. A detailed investigation of the cavity mode versus pump mode effects has been carried out by Maclean *et al.* [28]. This measurement was taken at a pump power of 4 W (input power of 3.28 W) on a 3-mirror cavity with high reflective mirrors and distance $d_1 = 61$ mm. Distance d_2 varied from 175 mm to 220 mm. The heatsink temperature was kept constant at 2 °C.

A more detailed look at this issue is shown in figure 2.14, where power transfers for different mode size have been taken with a HR mirror ($T = 0.086\,\%$). In particular measurements for mode sizes of ∼46 µm and ∼41 µm, larger and smaller than the pump spot size, have been carried out, obtaining higher efficiency and output power with a mode size of ∼41 µm. While the threshold power is 12 % higher for the smaller mode size, the slope efficiency is almost 50 % higher, with a 33 % increase in the output power.

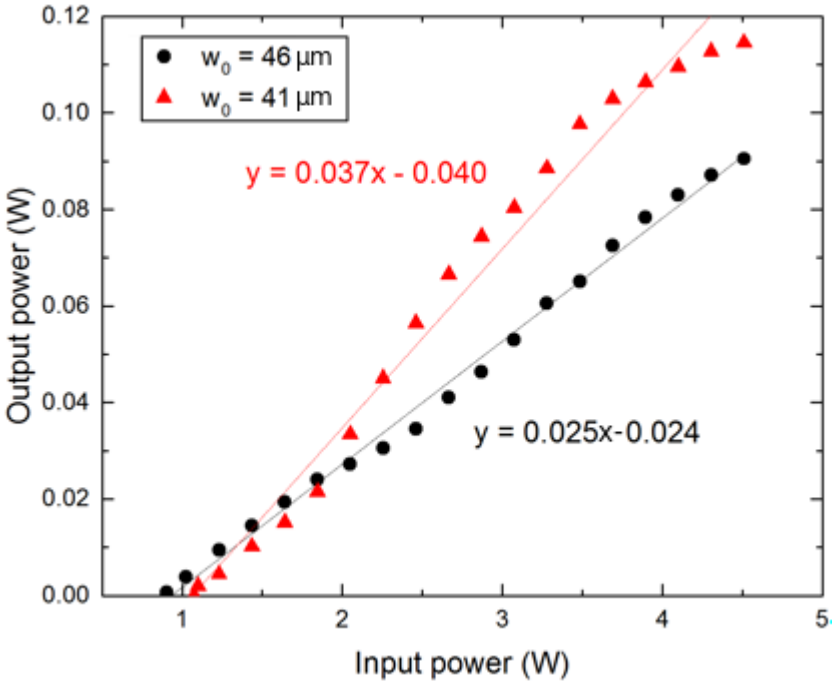

Figure 2.14: Fundamental output power as a function of input power for different beam sizes. As before, w_0 ~41 µm offers higher power.

It can also be noted the reduction in the slope for values of input power over 4 W, caused by thermal rollover as described in section 2.4.2.

We design the laser cavities to have a mode size at the SDL gain structure of ~41 µm from this point forward, but we will face some constraints, mostly regarding space, that will limit the cavity design. It should be taken into account that we are working with an experimental setup with standard off-the-shelf opto-mechanical mounts for the purpose of a proof of concept. Problems caused by space limitation could be solved in a future system with custom designed, compact components.

In order to further characterize our SDL sample we have carried out power transfer measurements of the output power with several output couplers, shown in figure 2.15. The maximum output power, achieved with a 3 % output coupler, was 0.87 W with 4.5 W of input power; featuring a slope efficiency of 25 %, similar to, and arguably a

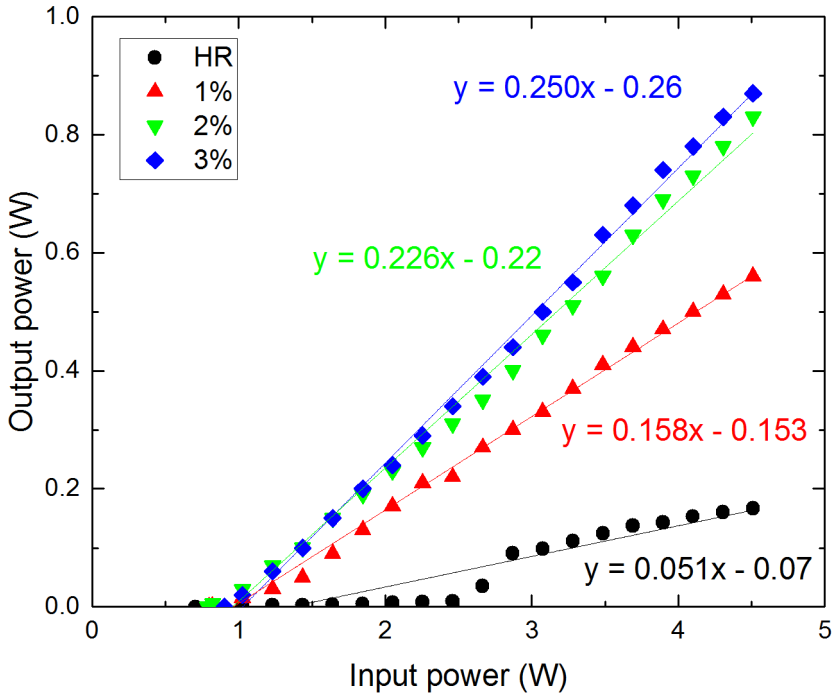

Figure 2.15: Power transfer measurements for different output couplers.

small improvement over, previous results [63, 64]. The strange shape of the HR curve was probably caused by a jump in the cavity mode.

The slope efficiencies (η_0) obtained with the power transfer can be used, together with the output coupler values, to conduct a Caird analysis [65] so the contribution of the parasitic losses of the cavity can be found, together with the internal quantum efficiency. A relationship exists between the inverses of the slope efficiency (η_0^{-1}) and the cavity output coupling (OC^{-1}):

$$\frac{1}{\eta_0} = \frac{1}{\eta_{\mathrm{lim}}} + \frac{L}{\eta_{\mathrm{lim}}} \frac{1}{\mathrm{OC}} \tag{2.1}$$

In this equation, L describes the cavity losses and OC corresponds to the output coupling value of the output mirror. The limiting slope efficiency (η_{lim}) corresponds to the slope efficiency that can be achieved in the absence of passive losses, as described

in [65]. From the linear fit the limiting slope can be extracted as the inverse of the vertical intercept. Knowing this quantity, the cavity parasitic losses can be found from the slope of the line.

Caird analysis is preferred over Findlay-Clay analysis [66] when characterising SDLs due to the strong dependence of the Findlay-Clay analysis on threshold pump powers. SDL performance and threshold power heavily depends on the pump power at which the cavity was optimized. Caird analysis, based on slope efficiency and output coupler transmittance, is more reliable for this type of laser. Although this method may not be applicable for high output coupling values (for which SDL performance drops dramatically) we restrict our measurements to HR, 1 %, 2 % and 3 % output couplers, well below the output coupling limits of the SDL [67].

From the linear fit in figure 2.16, and using equation (2.1), we can calculate the losses of this cavity to be $\sim 0.4\,\%$. The folding mirror reflection of $> 99.96\,\%$ must be taken into account (twice) and therefore the parasitic losses, only contributed from the losses in the semiconductor structure, are $\sim 0.3\,\%$.

From this result we can calculate the output coupling efficiency (η_{out}) of the laser cavity, which depends on the output coupler as well as the parasitic losses:

$$\eta_{\text{out}} = \frac{OC}{OC + L} \tag{2.2}$$

The laser slope efficiency can be expressed as the multiplication of a number of different factors that quantify the various stages of the photon – electron – photon conversion:

$$\eta_0 = \eta_{\text{abs}} \cdot \eta_{\text{quant}} \cdot \eta_{\text{out}} \cdot \eta_{\text{int}} \tag{2.3}$$

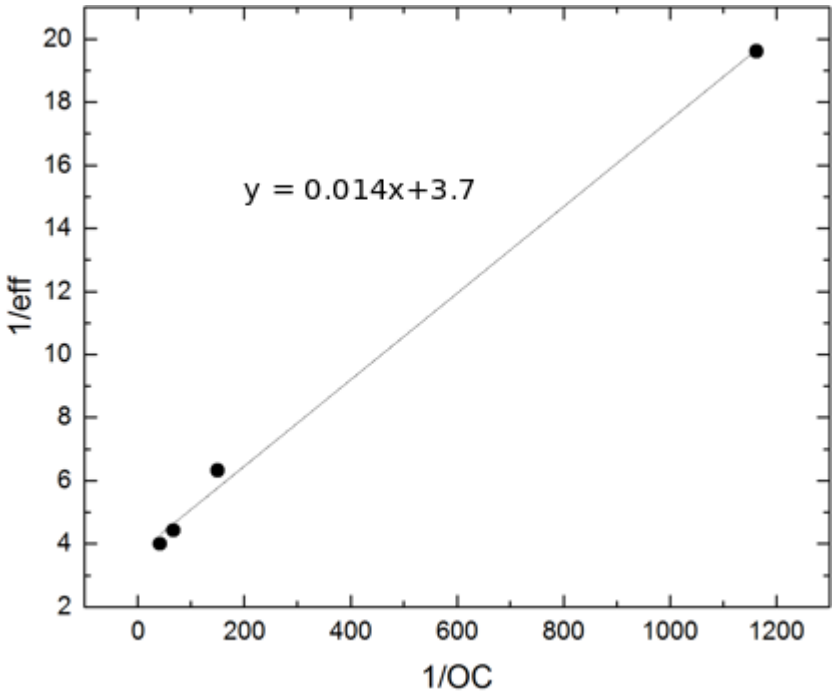

Figure 2.16: Caird analysis of the 3-mirror cavity. The calculated parasitic losses are ∼0.3 %.

The pump photon absorption efficiency (η_{abs}), based on previous results [68], is ~ 0.98. The quantum defect (η_{quant}) corresponds to the ratio between pump and laser wavelengths, ~ 0.79. The internal quantum efficiency (η_{int}) of the semiconductor can now be calculated to be ~ 0.35. It describes the probability of useful lasing recombination, and takes into account the different effects that may occur, such as recombination to the barrier valence band, Auger recombination or surface recombination (electrons escaping the confinement region). The efficiency values are summarized in table 2.1.

Table 2.1: Values of the different efficiency factors.

OC	η_0	η_{abs}	η_{quant}	η_{out}	η_{int}
HR	0.051	0.98	0.788	0.185	0.357
1 %	0.158	0.98	0.788	0.638	0.321
2 %	0.226	0.98	0.788	0.798	0.367
3 %	0.250	0.98	0.788	0.864	0.375

2.5 Conclusion

Semiconductor disk lasers are relatively new devices that bring together advantages from semiconductor and solid state lasers. This chapter has reviewed the principle of operation and design in order to illustrate how the impressive characteristics of this special kind of semiconductor laser arise.

In summary, SDLs combine high power, tunability, narrow linewidth, good beam quality and continuous-wave operation; and are particularly well suited for intracavity nonlinear conversion, the main topic of this work, thanks to the external, high-finesse cavity, strong intracavity fields and low optimum output coupling.

A preliminary characterization of the SDL structure has been carried out in a 3-mirror cavity in order to provide information on the expected optimum mode-matching and output coupling to be used when designing the more complex 4-, 5-, and 6-mirror cavities that will be built during the doubling and tripling experiments. The semiconductor sample has shown good performance with peer-comparable slope efficiencies and low parasitic losses. The fundamental emission at 675 nm (visible red radiation) provides a convenient base to reach near ultraviolet wavelengths in a single frequency conversion stage and deep-UV in a second, tripling stage.

References

[1] M. Kuznetsov, F. Hakimi, R. Sprague, and A. Mooradian. "Design and characteristics of high-power (>0.5W CW) diode-pumped vertical-external-cavity surface-emitting semiconductor lasers with circular TEM_{00} beams". In: *IEEE Journal of Selected Topics in Quantum Electronics* 5.3 (1999), pp. 561–573. DOI: 10.1109/2944.788419.

[2] A. C. Tropper, H. D. Foreman, A. Garnache, K. G. Wilcox, and S. H. Hoogland. "Vertical-external-cavity semiconductor lasers". In: *Journal of Physics D: Applied Physics* 37.9 (May 2004), R75–R85. DOI: 10.1088/0022-3727/37/9/R01.

[3] S. W. Corzine, R. S. Geels, J. W. Scott, R. H. Yan, and L. A. Coldren. "Design of Fabry-Perot surface-emitting lasers with a periodic gain structure". In: *IEEE Journal of Quantum Electronics* 25.6 (June 1989), pp. 1513–1524. DOI: 10.1109/3.29288.

[4] S. Calvez, J. E. Hastie, M. Guina, O. G. Okhotnikov, and M. D. Dawson. "Semiconductor disk lasers for the generation of visible and ultraviolet radiation". In: *Laser & Photonics Review* 3.5 (Sept. 2009), pp. 407–434. DOI: 10.1002/lpor.200810042.

[5] B. E. Jones. "ZnCdMgSe and AlGaInP multi-quantum well films for colour conversion and optically-pumped visible lasers". PhD thesis. University of Strathclyde, 2015, p. 201.

[6] A. Garnache, A. A. Kachanov, F. Stoeckel, and R. Houdré. "Diode-pumped broadband vertical-external-cavity surface-emitting semiconductor laser applied to high-sensitivity intracavity absorption spectroscopy". In: *Journal of the Optical Society of America B* 17.9 (2000), pp. 1589–1598. DOI: 10.1364/JOSAB.17.001589.

[7] A. C. Tropper and S. Hoogland. “Extended cavity surface-emitting semiconductor lasers”. In: *Progress in Quantum Electronics* 30.1 (2006), pp. 1–43. DOI: 10.1016/j.pquantelec.2005.10.002.

[8] M. Schmid, S. Benchabane, F. Torabi-Goudarzi, R. Abram, A. I. Ferguson, and E. Riis. “Optical in-well pumping of a vertical-external-cavity surface-emitting laser”. In: *Applied Physics Letters* 84.24 (June 2004), pp. 4860–4862. DOI: 10.1063/1.1760887.

[9] S. S. Beyertt, M. Zorn, T. Kübler, H. Wenzel, M. Weyers, A. Giesen, G. Tränkle, and U. Brauch. “Optical in-well pumping of a semiconductor disk laser with high optical efficiency”. In: *IEEE Journal of Quantum Electronics* 41.12 (2005), pp. 1439–1449. DOI: 10.1109/JQE.2005.858794.

[10] C. M. N. Mateo, U. Brauch, H. Kahle, R. Bek, T. Schwarzbäck, M. Jetter, M. Abdou Ahmed, P. Michler, and T. Graf. “Efficiency and power scaling of in-well and multi-pass pumped AlGaInP VECSELs”. In: *SPIE 9734*. Ed. by K. G. Wilcox. Mar. 2016, p. 973410. DOI: 10.1117/12.2212162.

[11] T. D. Raymond, W. J. Alford, M. H. Crawford, and A. A. Allerman. “Intracavity frequency doubling of a diode-pumped external-cavity surface-emitting semiconductor laser.” In: *Optics letters* 24.16 (1999), pp. 1127–9. DOI: 10.1364/OL.24.001127.

[12] J. E. Hastie, L. G. Morton, A. J. Kemp, M. D. Dawson, A. B. Krysa, and J. S. Roberts. “Tunable ultraviolet output from an intracavity frequency-doubled red vertical-external-cavity surface-emitting laser”. In: *Applied Physics Letters* 89.6 (Aug. 2006), p. 061114. DOI: 10.1063/1.2236108.

[13] J. A. Piper and H. M. Pask. “Crystalline Raman lasers”. In: *IEEE Journal on Selected Topics in Quantum Electronics* 13.3 (2007), pp. 692–704. DOI: 10.1109/JSTQE.2007.897175.

[14] T. D. Germann, A. Strittmatter, U. W. Pohl, D. Bimberg, J. Rautiainen, M. Guina, and O. G. Okhotnikov. “Quantum-dot semiconductor disk lasers”. In:

Journal of Crystal Growth 310.23 (2008), pp. 5182–5186. DOI: 10.1016/j.jcrysgro.2008.07.004.

[15] N. M. Neil W. Ashcroft. *Solid State Physics*. Cengage Learning, Inc, Jan. 2, 1976. 848 pp.

[16] A. R. Adams. "Band-structure engineering for low-threshold high-efficiency semiconductor lasers". In: *Electronics Letters* 22.5 (1986), p. 249. DOI: 10.1049/el:19860171.

[17] A. R. Adams. "Strained-Layer Quantum-Well Lasers". In: *IEEE Journal of Selected Topics in Quantum Electronics* 17.5 (Sept. 2011), pp. 1364–1373. DOI: 10.1109/JSTQE.2011.2108995.

[18] J. W. Matthews and A. E. Blakeslee. "Defects in epitaxial multilayers. III. Preparation of almost perfect multilayers". In: *Journal of Crystal Growth* 32.2 (1976), pp. 265–273. DOI: 10.1016/0022-0248(76)90041-5.

[19] D. Bour, R. Geels, D. Treat, T. Paoli, F. Ponce, R. Thornton, B. Krusor, R. Bringans, and D. Welch. "Strained $Ga_xIn_{1-x}P/(AlGa)_{0.5}In_{0.5}P$ heterostructures and quantum-well laser diodes". In: *IEEE Journal of Quantum Electronics* 30.2 (1994), pp. 593–607. DOI: 10.1109/3.283808.

[20] E. Yablonovitch and E. Kane. "Reduction of lasing threshold current density by the lowering of valence band effective mass". In: *Journal of Lightwave Technology* 4.5 (1986), pp. 504–506. DOI: 10.1109/JLT.1986.1074751.

[21] N. J. Ekins-Daukes, K. Kawaguchi, and J. Zhang. "Strain-Balanced Criteria for Multiple Quantum Well Structures and Its Signature in X-ray Rocking Curves †". In: *Crystal Growth & Design* 2.4 (July 2002), pp. 287–292. DOI: 10.1021/cg025502y.

[22] H. A. MacLeod. *Thin-Film Optical Filters*. 3rd. CRC Press, 2001, p. 668.

[23] J. E. Hastie. "High Power Surface Emitting Semiconductor Lasers". PhD thesis. University of Strathclyde, 2004, p. 188.

[24] E. F. Schubert. *Light-Emitting Diodes*. Cambridge University Press, June 1, 2006. 434 pp.

[25] L. Fan, M. Fallahi, J. T. Murray, R. Bedford, Y. Kaneda, A. R. Zakharian, J. Hader, J. V. Moloney, W. Stolz, and S. W. Koch. "Tunable high-power high-brightness linearly polarized vertical-external-cavity surface-emitting lasers". In: *Applied Physics Letters* 88.2 (2006), pp. 1–3. DOI: 10.1063/1.2164921.

[26] F. Zhang, B. Heinen, M. Wichmann, C. Möller, B. Kunert, A. Rahimi-Iman, W. Stolz, and M. Koch. "A 23-watt single-frequency vertical-external-cavity surface-emitting laser". In: *Optics Express* 22.11 (2014), p. 12817. DOI: 10.1364/OE.22.012817.

[27] R. Butté, J.-F. F. Carlin, E. Feltin, M. Gonschorek, S. Nicolay, G. Christmann, D. Simeonov, A. Castiglia, J. Dorsaz, H. J. Buehlmann, S. Christopoulos, G. Baldassarri Höger von Högersthal, a. J. D. Grundy, M. Mosca, C. Pinquier, M. A. Py, F. Demangeot, J. Frandon, P. G. Lagoudakis, J. J. Baumberg, and N. Grandjean. "Current status of AlInN layers lattice-matched to GaN for photonics and electronics". In: *Journal of Physics D: Applied Physics* 40.20 (2007), pp. 6328–6344. DOI: 10.1088/0022-3727/40/20/s16.

[28] A. J. Maclean, R. B. Birch, P. W. Roth, A. J. Kemp, and D. Burns. "Limits on efficiency and power scaling in semiconductor disk lasers with diamond heat-spreaders". In: *Journal of the Optical Society of America B* 26.12 (Dec. 2009), p. 2228. DOI: 10.1364/JOSAB.26.002228.

[29] M. Kuznetsov, F. Hakimi, R. Sprague, and A. Mooradian. "High-Power (0.5W CW) Diode-Pumped Vertical-External-Cavity Surface-Emitting Semiconductor Lasers with Circular TEM_{00} Beams". In: *IEEE Photonics Technology Letters* 9.8 (1997), pp. 1063–1065. DOI: 10.1109/68.605500.

[30] Z. L. Liau. "Semiconductor wafer bonding via liquid capillarity". In: *Applied Physics Letters* 77.5 (2000), pp. 651–653. DOI: 10.1063/1.127074.

[31] W. J. Alford, T. D. Raymond, and A. A. Allerman. "High power and good beam quality at 980 nm from a vertical external-cavity surface-emitting laser". In: *Journal of the Optical Society of America B* 19.4 (2002), p. 663. DOI: 10.1364/JOSAB.19.000663.

[32] A. Kemp, G. Valentine, J.-M. Hopkins, J. Hastie, S. Smith, S. Calvez, M. Dawson, and D. Burns. "Thermal management in vertical-external-cavity surface-emitting lasers: finite-element analysis of a heatspreader approach". In: *IEEE Journal of Quantum Electronics* 41.2 (Feb. 2005), pp. 148–155. DOI: 10.1109/JQE.2004.839706.

[33] R. Haring, M. Paschotta, a. Aschwanden, E. Gini, F. Morier-Genoud, and U. Keller. "High-power passively mode-locked semiconductor lasers". In: *IEEE Journal of Quantum Electronics* 38.9 (2002), pp. 1268–1275. DOI: 10.1109/JQE.2002.802111.

[34] T.-L. Wang, Y. Kaneda, J. Hader, J. V. Moloney, B. Kunert, W. Stolz, and S. W. Koch. "Strategies for power scaling VECSELs". In: *Proceedings of SPIE* 8242 (2012), p. 824209. DOI: 10.1117/12.909369.

[35] B. Heinen, C. Moller, K. Jandieri, B. Kunert, M. Koch, and W. Stolz. "The Thermal Resistance of High-Power Semiconductor Disk Lasers". In: *IEEE Journal of Quantum Electronics* 51.5 (May 2015), pp. 1–9. DOI: 10.1109/JQE.2015.2412458.

[36] B. Heinen, T.-L. Wang, M. Sparenberg, A. Weber, B. Kunert, J. Hader, S. Koch, J. Moloney, M. Koch, and W. Stolz. "106 W continuous-wave output power from vertical-external-cavity surface-emitting laser". In: *Electronics Letters* 48.9 (2012), p. 516. DOI: 10.1049/el.2012.0531.

[37] A. J. Kemp, A. J. MacLean, J. E. Hastie, S. A. Smith, J. M. Hopkins, S. Calvez, G. J. Valentine, M. D. Dawson, and D. Burns. "Thermal lensing, thermal management and transverse mode control in microchip VECSELs". In: *Applied Physics B: Lasers and Optics* 83.2 (2006), pp. 189–194. DOI: 10.1007/s00340-006-2151-z.

[38] J. E. Hastie, J.-M. Hopkins, S. Calvez, Chan Wook Jeon, D. Burns, R. Abram, E. Riis, A. I. Ferguson, and M. D. Dawson. "0.5-W single transverse-mode operation of an 850-nm diode-pumped surface-emitting semiconductor laser". In: *IEEE Photonics Technology Letters* 15.7 (July 2003), pp. 894–896. DOI: 10.1109/LPT.2003.813446.

[39] L. Fan, C. Hessenius, M. Fallahi, J. Hader, H. Li, J. V. Moloney, W. Stolz, S. W. Koch, J. T. Murray, and R. Bedford. "Highly strained InGaAsGaAs multiwatt vertical-external-cavity surface-emitting laser emitting around 1170 nm". In: *Applied Physics Letters* 91.13 (2007), pp. 2005–2008. DOI: 10.1063/1.2790838.

[40] J. Paajaste, S. Suomalainen, R. Koskinen, A. Härkönen, M. Guina, and M. Pessa. "High-power and broadly tunable GaSb-based optically pumped VECSELs emitting near 2μm". In: *Journal of Crystal Growth* 311.7 (Mar. 2009), pp. 1917–1919. DOI: 10.1016/j.jcrysgro.2008.10.071.

[41] N. Schulz, J. M. Hopkins, M. Rattunde, D. Burns, and J. Wagner. "High-brightness long-wavelength semiconductor disk lasers". In: *Laser and Photonics Reviews* 2.3 (July 2008), pp. 160–181. DOI: 10.1002/lpor.200710037.

[42] R. Debusmann, N. Dhidah, V. Hoffmann, L. Weixelbaum, U. Brauch, T. Graf, M. Weyers, and M. Kneissl. "InGaN-GaN disk laser for blue-violet emission wavelengths". In: *IEEE Photonics Technology Letters* 22.9 (2010), pp. 652–654. DOI: 10.1109/LPT.2010.2043668.

[43] V. G. Savitski, J. E. Hastie, S. Calvez, and M. D. Dawson. "Cavity-dumping of a semiconductor disk laser for the generation of wavelength-tunable micro-Joule nanosecond pulses". In: *Optics Express* 18 (May 2010), p. 11933. DOI: 10.1364/OE.18.011933.

[44] K. G. Wilcox, Z. Mihoubi, G. J. Daniell, S. Elsmere, A. Quarterman, I. Farrer, D. A. Ritchie, and A. Tropper. "Ultrafast optical Stark mode-locked semiconductor laser." In: *Optics letters* 33.23 (2008), pp. 2797–2799. DOI: 10.1364/OL.33.002797.

[45] D. Waldburger, S. M. Link, M. Mangold, C. G. E. Alfieri, E. Gini, M. Golling, B. W. Tilma, and U. Keller. "High-power 100 fs semiconductor disk lasers". In: *Optica* 3.8 (2016), pp. 844–852. DOI: 10.1364/OPTICA.3.000844.

[46] S. Hoogland, S. Dhanjal, A. Tropper, J. Roberts, R. Haring, R. Paschotta, F. Morier-Genoud, and U. Keller. "Passively mode-locked diode-pumped surface-emitting semiconductor laser". In: *IEEE Photonics Technology Letters* 12.9 (Sept. 2000), pp. 1135–1137. DOI: 10.1109/68.874213.

[47] A. Garnache, S. Hoogland, A. C. Tropper, I. Sagnes, G. Saint-Girons, and J. S. Roberts. "Sub-500-fs soliton-like pulse in a passively mode-locked broadband surface-emitting laser with 100 mW average power". In: *Applied Physics Letters* 80.21 (May 2002), pp. 3892–3894. DOI: 10.1063/1.1482143.

[48] D. Maas, A.-R. Bellancourt, B. Rudin, M. Golling, H. Unold, T. Südmeyer, and U. Keller. "Vertical integration of ultrafast semiconductor lasers". In: *Applied Physics B* 88.4 (Sept. 2007), pp. 493–497. DOI: 10.1007/s00340-007-2760-1.

[49] A.-R. Bellancourt, D. Maas, B. Rudin, M. Golling, T. Südmeyer, and U. Keller. "Modelocked integrated external-cavity surface emitting laser". In: *IET Optoelectronics* 3.2 (Apr. 2009), pp. 61–72.

[50] B. W. Tilma, M. Mangold, C. A. Zaugg, S. M. Link, D. Waldburger, A. Klenner, A. S. Mayer, E. Gini, M. Golling, and U. Keller. "Recent advances in ultrafast semiconductor disk lasers". In: *Light: Science & Applications* 4.7 (July 2015), e310. DOI: 10.1038/lsa.2015.83.

[51] P. Klopp, U. Griebner, M. Zorn, and M. Weyers. "Pulse repetition rate up to 92 GHz or pulse duration shorter than 110 fs from a mode-locked semiconductor disk laser". In: *Applied Physics Letters* 98.7 (2011), pp. 16–19. DOI: 10.1063/1.3554751.

[52] D. Lorenser, D. J. H. C. Maas, H. J. Unold, A. R. Bellancourt, B. Rudin, E. Gini, D. Ebling, and U. Keller. "50-GHz passively mode-locked surface-emitting semiconductor laser with 100-mW average output power". In: *IEEE Journal*

of Quantum Electronics 42.8 (2006), pp. 838–847. DOI: 10.1109/JQE.2006.878183.

[53] M. Mangold, C. A. Zaugg, S. M. Link, M. Golling, B. W. Tilma, and U. Keller. "Pulse repetition rate scaling from 5 to 100 GHz with a high-power semiconductor disk laser". In: *Optics Express* 22.5 (2014), p. 6099. DOI: 10.1364/OE.22.006099.

[54] K. G. Wilcox, A. C. Tropper, H. E. Beere, D. A. Ritchie, B. Kunert, B. Heinen, and W. Stolz. "4.35 kW peak power femtosecond pulse mode-locked VECSEL for supercontinuum generation". In: *Optics express* 21.2 (2013), pp. 1599–1605. DOI: 10.1364/OE.21.001599.

[55] M. Holm, D. Burns, A. Ferguson, and M. Dawson. "Actively stabilized single-frequency vertical-external-cavity AlGaAs laser". In: *IEEE Photonics Technology Letters* 11.12 (1999), pp. 1551–1553. DOI: 10.1109/68.806843.

[56] A. Laurain, C. Mart, J. Hader, J. V. Moloney, B. Kunert, and W. Stolz. "15 W Single Frequency Optically Pumped Semiconductor Laser With Sub-Megahertz Linewidth". In: *IEEE Photonics Technology Letters* 26.2 (Jan. 2014), pp. 131–133. DOI: 10.1109/LPT.2013.2290062.

[57] R. W. P. Drever, J. L. Hall, F. V. Kowalski, J. Hough, G. M. Ford, A. J. Munley, and H. Ward. "Laser phase and frequency stabilization using an optical resonator". In: *Applied Physics B* 31.2 (1983), pp. 97–105. DOI: 10.1007/BF00702605.

[58] E. D. Black. "An introduction to Pound–Drever–Hall laser frequency stabilization". In: *American Journal of Physics* 69.1 (Jan. 2001), pp. 79–87. DOI: 10.1119/1.1286663.

[59] D. Pabœuf and J. E. Hastie. "Tunable narrow linewidth AlGaInP semiconductor disk laser for Sr atom cooling applications". In: *Applied Optics* 55.19 (July 2016), p. 4980. DOI: 10.1364/AO.55.004980.

[60] Coherent. *Short Upper State Lifetime Eliminates "Green Problem," Setting the Industry Standard for Lowest Overall Noise*. Web. Dec. 2017.

[61] Coherent. *Verdi V-Series Family.* https://cohrcdn.azureedge.net/assets/pdf/Verdi-Family-Data-Sheet.pdf. 2011.

[62] Coherent. *Verdi G-Series Family.* https://cohrcdn.azureedge.net/assets/pdf/Verdi-G-Series-Family-Data-Sheet.pdf. 2013.

[63] J. E. Hastie, S. Calvez, M. D. Dawson, T. Leinonen, A. Laakso, J. Lyytikäinen, and M. Pessa. "High power CW red VECSEL with linearly polarized TEM_{00} output beam". In: *Optics Express* 13.1 (Jan. 2005), p. 77. DOI: 10.1364/OPEX.13.000077.

[64] T. Schwarzbäck, M. Eichfelder, W.-M. Schulz, R. Roßbach, M. Jetter, and P. Michler. "Short wavelength red-emitting AlGaInP-VECSEL exceeds 1.2 W continuous-wave output power". In: *Applied Physics B* 102.4 (Mar. 2011), pp. 789–794. DOI: 10.1007/s00340-010-4213-5.

[65] J. A. Caird, S. A. Payne, P. R. Staber, A. J. Ramponi, L. L. Chase, and W. F. Krupke. "Quantum electronic properties of the $Na_3Ga_2Li_3F_{12}$:Cr^{3+} laser". In: *IEEE Journal of Quantum Electronics* 24.6 (June 1988), pp. 1077–1099. DOI: 10.1109/3.231.

[66] D. Findlay and R. Clay. "The measurement of internal losses in 4-level lasers". In: *Physics Letters* 20.3 (Feb. 1966), pp. 277–278. DOI: 10.1016/0031-9163(66)90363-5.

[67] J.-M. Hopkins, A. J. Maclean, D. Burns, E. Riis, N. Schulz, M. Rattunde, C. Manz, K. Köhler, and J. Wagner. "Tunable, Single-frequency, Diode-pumped 2.3μm VECSEL". In: *Optics Express* 15.13 (2007), p. 8212. DOI: 10.1364/OE.15.008212.

[68] P. J. Schlosser. "Vertical External Cavity Surface Emitting Lasers Utilising Quantum Dot Active Regions". PhD thesis. Univeristy of Strathclyde, 2011, p. 269.

CHAPTER 3

Nonlinear Optics

3.1 Introduction

Nonlinear optics plays a crucial role in this work. Our main target is to design and build a semiconductor disk laser emitting at deep ultraviolet wavelengths, for which current semiconductor technology is unable to produce direct emission. The field of nonlinear optics opens the door to frequency conversion processes by which our fundamental, red, laser beam can generate laser emission at higher frequencies (i.e. shorter wavelengths) under appropriate conditions. As we will see throughout this chapter, these conditions require the use of particular nonlinear media, together with observing the conditions set by the laws of conservation (energy and momentum) and optimization of the system for efficient frequency conversion.

Since nonlinear optics is a challenging field and has been the subject of decades of theoretical and experimental work, we shall first review the basic concepts with the intention of building an intuitive vision of the mechanics taking place, complemented with a formal description of the field and of the equations ruling the processes of interest for this study.

3.1.1 Historical introduction

Some nonlinear effects, induced by strong electric or magnetic fields, were known for a long time before the advent of the laser (e.g. the Kerr effect was discovered in 1875 [1, 2]. Electric permittivity and magnetic permeability nonlinearity were also known in advance. Lasers, however, provided access to the strongest photon densities ever achieved, easily an order of magnitude greater than those required to observe nonlinear effects (the amplitude of the external field being of the order of the atomic electric field [3]). The first maser (a device operating on the same principle as lasers but in the microwave range) was produced in 1954 by Townes, Gordon and Zeiger [4, 5]. The first laser, based on a ruby crystal and emitting red light at 694 nm, was built in 1960 by Maiman [6]. Soon after this breakthrough, in 1961, Franken *et al.* used a similar device to generate optical harmonics [7]. The field of nonlinear optics was thus established.

3.1.2 Definition

Nonlinear optics is the field of physics that studies the effects caused by the nonlinear response of a material to the electromagnetic fields travelling through it. For this nonlinear response to be observable, the electromagnetic fields must be intense, such as those found in a laser beam.

Light – matter interactions can be divided into three groups:

- Charge oscillation and photon scattering: electromagnetic fields induce oscillation of charges and every accelerated charge emits electromagnetic radiation. This is the most common type of interaction, explaining reflection and refraction processes and harmonic generation, and therefore it is our main interest.

- Absorption (and emission) of photons by electrons: confined electrons (also nuclei or molecules) have discrete values of energy, or energy levels. Any change in the

energy level of one of these particles requires absorption or emission of energy, commonly in the form of a photon. Laser emission falls within this group, as explained in the previous chapter.

- Pair production and annihilation: under certain circumstances, a photon with enough energy can produce a particle – antiparticle pair. Similarly, a particle – antiparticle collision can produce photon emission. Electron – positron creation and annihilation is a common example of this group. Unfortunately, and despite the inherent appeal of particle physics, this type of interaction is outwith the scope of this work.

The first type of light – matter interaction described is the most commonly observed. The reason for this is that it does not require any particular condition to be fulfilled (such as photons having certain energy for discrete absorption from electrons). The most powerful classical model to study this interaction is the Lorentz model, from the beginning of the 20^{th} century [8]. By considering the atom as a harmonic oscillator, this model successfully describes the linear optical properties of non-metallic solids. This model was later used by Rayleigh to explain nonlinearities in acoustic resonators [9].

When light travels through a system, its oscillating electric field will necessarily induce oscillations on the charges of which such a system is composed. Most commonly, this oscillation can be thought of simply in terms of electrons oscillating within their energy level (or in a more modern approach, a change in the shape of the electronic distribution). The effect this electromagnetic radiation has on the system is converting the neutral components to oscillating dipoles. These dipoles will emit new radiation, as described by Larmor in 1897 [10]. Macroscopically, the refractive index of a material is the most straightforward observation: this photon – dipole interaction gives rise to refraction, photon scattering, etc.

If the intensity of the input (or pump) fields is low (e.g. lightbulb light) the dipoles oscillate harmonically, and they emit electromagnetic radiation with the same frequency

as the oscillation (which is the same as the original light). However, when the pump amplitude becomes large enough (e.g. laser light) the dipole oscillation becomes anharmonic and additional frequencies start to appear. As a result, emission with twice, three times... the frequency of the input light (fundamental frequency) is produced. These terms with frequencies that are multiples of the fundamental are called harmonics, and under some circumstances can become intense enough to overcome the fundamental emission. In fact, since the energy we gain as harmonics is energy being lost from the fundamental, we could theoretically convert our entire fundamental light to its second harmonic (with twice the frequency), keeping the total amount of energy constant (but reducing the number of photons by half).

The process just described is known as (second) harmonic generation, and it is only one of the many effects that nonlinear light – matter interactions can produce. This process does not transfer energy into the system, whose initial and final quantum states are unchanged. This type of process is described as parametric. Since photons interact with electrons, thinking about it in terms of electronic energy levels is very inviting. One should avoid this temptation, since no transfer of energy (neither of linear momentum or angular momentum) takes place. It is nevertheless common to describe the process in terms of virtual states, as depicted in figures 3.1a and 3.1b.

3.1.3 Nonlinear processes

Nonlinear optics can produce a number of different effects, both in the electromagnetic fields involved or in the materials used as nonlinear media. Modifications of the frequency of the light field or of the phase, self-focusing, variations of the refractive index of the materials, signal amplification or multiphoton absorption are only a few examples of the astonishing results observable in the field of nonlinear optics. The work described in this thesis revolves around frequency conversion, in particular up-conversion, or converting to higher frequencies, extending the emitting range of lasers further into the ultraviolet. Down-conversion processes, or converting to lower frequencies, are the

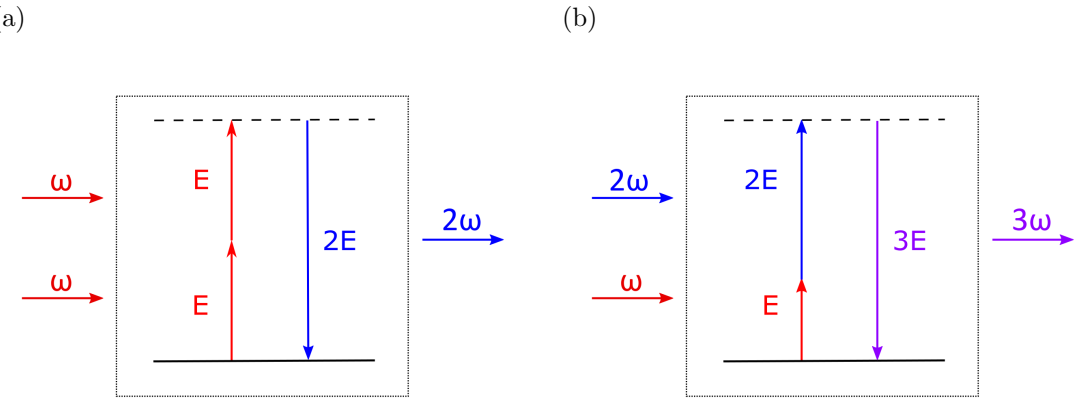

Figure 3.1: (a) Second harmonic generation described in terms of virtual energy levels. Two photons of the same frequency are combined into a new photon with twice the original frequency. (b) Sum-frequency generation. Two photons with energy ω_1 and ω_2 are combined to create a new photon with frequency $\omega_3 = \omega_1 + \omega_2$. In the case depicted, $\omega_2 = 2\omega_1$ and therefore $\omega_3 = 3\omega_1$. Third harmonic generation achieved by SFG is usually more efficient than direct THG (since the latter is a third order process).

other 'half of the equation', extending the range of similar lasers into the infrared. Both techniques can be used to cover gaps in laser emission caused by material limitations (e.g. the semiconductor 'green gap', usually covered by SHG from IR emission). Among the most common frequency conversion processes we can find the following:

SHG

Obtaining a frequency twice that of the fundamental beam used is probably the most common frequency conversion, and also the first one experimentally achieved, by Franken *et al.* in 1961 [7]. In this process two identical photons mix to generate a third photon with twice the energy. It is, in fact, a special case of sum-frequency generation.

SFG

This process mixes two photons of different energies to generate another photon with the combined energy of the two. Unlike in the special case of SHG, two input beams are required, making this process more complicated than the previous one since it means aligning the system with one more beam.

DFG/ OPOs

The reverse of SFG, in this process a higher energy photon splits into two photons of lower energy. This process is mainly used in parametric amplification, where the highest frequency beam, called the pump, transfers energy to a second beam, called the signal, thus amplifying it. A third beam is generated in the process (idler). Optical parametric oscillators make use of this process in a resonant cavity for the signal (or, less usually, for both signal and idler) to generate laser gain.

3.2 Mathematical description

3.2.1 Lorentz oscillator model

Let's consider again the Lorentz oscillator model [3, 8, 11]. The electrons are bound to the atom nucleus obeying Hooke's law. A damping term must also be used to account for collisions and emitted radiation. Finally, a quadratic term is added to the restoring force to account for the nonlinearity of the system. The equation of motion of the electron position x can then be written as:

$$\ddot{x} + \Gamma\dot{x} + \omega_0^2 x + ax^2 = \tfrac{1}{m} F_{\text{external}} \tag{3.1}$$

where the electron (of mass m) is affected by a damping force of the form $\Gamma\dot{x}$ and a restoring force of the form $\omega_0^2 x + ax^2$. The external force in this case will be that caused by an optical field $E(t)$, which will correspond to a monochromatic beam (to follow the previous example about SHG):

$$F = \mathrm{q}E(t) = -\mathrm{e}E_0 \left(e^{-i\omega_1 t} + e^{+i\omega_1 t}\right) \tag{3.2}$$

Note that a wavevector contribution (e.g. e^{ikz}) is not relevant for the present study and would actually vanish in the following argument.

If the external force of equation (3.1) is of the form of equation (3.2), the equation of movement does not have an analytic solution. However, it is solved by considering that the nonlinear term of the restoring force is sufficiently small compared with the linear term. The Rayleigh – Schrödinger perturbation theory is used to obtain the nonlinear corrections to the exact, linear solution.

If we add a parameter λ (with a value between 0 and 1) to the external force so equation (3.1) reduces to that of an anharmonic oscillator with no external forces for $\lambda = 0$ (giving a solution x), increasing λ will add perturbative terms to this solution, which can be expressed as an expansion in powers of λ:

$$x = \lambda x_1 + \lambda^2 x_2 + \lambda^3 x_3 + \ldots \tag{3.3}$$

If we introduce this solution in equation (3.1), the summand terms are obtained as functions of powers of λ. The summands should satisfy the equation for each order of λ independently in order for equation (3.3) to be a solution. We obtain a number of equations of the form:

$$\begin{aligned}
\lambda: &\quad \ddot{x_1} + \Gamma \dot{x_1} + \omega_0^2 x_1 = \tfrac{-\mathrm{e}}{m} E_0 \left(e^{-i\omega_1 t} + e^{+i\omega_1 t} \right) \\
\lambda^2: &\quad \ddot{x_2} + \Gamma \dot{x_2} + \omega_0^2 x_2 + a x_1^2 = 0 \\
\lambda^3: &\quad \ddot{x_3} + \Gamma \dot{x_3} + \omega_0^2 x_3 + a x_1 x_2 = 0 \\
&\dots
\end{aligned} \tag{3.4}$$

Since this work is focused around second order nonlinearities we will not study the terms beyond quadratic. The first equation corresponds to the damped oscillator driven by an external force. The steady state solution in this case is known, and corresponds to:

$$\begin{aligned}
x_1(\omega_1, t) &= A_1 e^{-i\omega_1 t} + B_1 e^{i\omega_1 t} \\
A_1 &= -\frac{\mathrm{e}}{m} \frac{E_0}{C(\omega_1)} \\
B_1 &= -\frac{\mathrm{e}}{m} \frac{E_0}{C(-\omega_1)} \\
C(\omega_1) &= \omega_0^2 - \omega_1^2 - i\Gamma\omega_1
\end{aligned} \tag{3.5}$$

If we now include this solution into the second order equation of equation (3.4) we obtain an analogous equation to the first order solution, with the nonlinear restoring term effectively being a new driving force:

$$\begin{aligned}
a x_1^2 &= a \left[A_1 e^{-i\omega_1 t} + B_1 e^{i\omega_1 t} \right]^2 \\
&= a A_1^2 e^{-i2\omega_1 t} + a B_1^2 e^{i2\omega_1 t} + 2a A_1 B_1
\end{aligned} \tag{3.6}$$

We can observe how terms depending on twice the frequency (second harmonic frequency) appear, together with a non-oscillating term. The solutions for each will be:

$$\begin{aligned} x_2(\omega_2 = 2\omega_1, t) &= A_2 e^{-i2\omega_1 t} + B_2 e^{i2\omega_1 t} \\ x_2(0, t) &= \frac{2A_1 B_1}{\omega_0^2} \end{aligned} \tag{3.7}$$

$$\begin{aligned} x_2(\omega_2 = 2\omega_1, t) &= \frac{-a[\frac{\mathrm{e}}{m}]^2 E_0^2}{C(\omega_1)^2 C(2\omega_1)} e^{-i2\omega_1 t} + \frac{-a[\frac{\mathrm{e}}{m}]^2 E_0^2}{C(-\omega_1)^2 C(-2\omega_1)} e^{i2\omega_1 t} \\ x_2(0) &= \frac{-2a[\frac{\mathrm{e}}{m}]^2 E_0^2}{C(0)C(\omega_1)C(-\omega_1)} \end{aligned} \tag{3.8}$$

The time-independent solution $x_2(0)$ corresponds to the optical rectification. The solution $x_2(\omega_2 = 2\omega_1)$ is describing an oscillation of the dipole with frequency twice the optical field, which will likewise emit electromagnetic radiation with frequency $2\omega_1$: the second harmonic of the fundamental field.

This method can be generalised to an input optical field comprising two different frequencies ω_1 and ω_2, obtaining solutions depending on $\omega_1 + \omega_2$ and $\omega_1 - \omega_2$, as well as $2\omega_1$, $2\omega_2$ and 0. The new terms account for sum and difference-frequency generation.

Stronger fields will produce stronger perturbations, and higher order terms become relevant, giving rise to a large range of different effects, from higher harmonics generation to Raman emission.

3.2.2 Polarization

The electric polarization of a material (or polarization density) quantifies how materials react to external fields. It expresses the induced dipole moment in said materials, and can be written in terms of the dipole moments of its components as:

$$P = -Nex \tag{3.9}$$

where N is the number density of dipoles.

We can substitute our solution of x (equations (3.5) and (3.7)) to obtain the linear and nonlinear contributions $P_{\mathrm{L}}(\omega)$, $P_{\mathrm{NL}}(2\omega)$...

Since P represents the reaction to an external field, it is usual to express it in terms of such a field:

$$P = \epsilon_0 \chi E \tag{3.10}$$

In this last equation we find the constant of proportionality χ, called electric susceptibility, which tells us the strength of the material response to the external field, and the vacuum permittivity ϵ_0. When the external field is strong enough to produce a nonlinear response from the material, we generalise this expression by means of a power series expansion:

$$\vec{P} = \epsilon_0 \chi^{(1)} \vec{E} + \epsilon_0 \chi^{(2)} \vec{E}^2 + \epsilon_0 \chi^{(3)} \vec{E}^3 + ... \tag{3.11}$$

If we focus, for example, on the quadratic term for an input composed of two different beams, we can express it as:

$$\vec{E}(t) = E_1 e^{-i\omega_1 t} + E_2 e^{-i\omega_2 t} + c.c. \tag{3.12}$$

$$\begin{aligned} \vec{P}^{(2)}_{\mathrm{NL}} = \epsilon_0 \chi^{(2)} [E_1^2 e^{-i2\omega_1 t} + E_2^2 e^{-i2\omega_2 t} + 2E_1 E_2 e^{-i(\omega_1+\omega_2)t} + \\ + 2E_1 E_2^* e^{-i(\omega_1-\omega_2)t} + c.c.] + 2\epsilon_0 \chi^{(2)} [E_1 E_1^* + E_2 E_2^*] \end{aligned} \tag{3.13}$$

We can observe again terms with frequency harmonics, as well as the optical rectification term.

Susceptibility

As just mentioned, the electric susceptibility defines how responsive the material dipoles (the material polarization) are to external fields, acting as a constant of proportionality between these two quantities (as seen in equation (3.9)). Since $\boldsymbol{E}$ and $\boldsymbol{P}$ are actually three-dimensional vector fields, $\boldsymbol{\chi}$ will in general be a tensor. Nevertheless, given a propagation direction and a fixed polarization (i.e. for a fixed geometry), the susceptibility can be expressed as a scalar quantity.

An expression for this quantity can be obtained by relating equations (3.9) and (3.10). In particular in the case of linear susceptibility:

$$\chi^{(1)}(\omega_i) = \frac{N\mathrm{e}^2}{\epsilon_0 m C(\omega_i)} \tag{3.14}$$

While in the case of second order susceptibility we find:

$$\chi^{(2)}(\omega_3, \omega_2, \omega_1) = \frac{Na\mathrm{e}^3}{\epsilon_0 m^2 C(\omega_3) C(\omega_2) C(\omega_1)} \tag{3.15}$$

Which can be written in terms of the susceptibilities of the different frequency components:

$$\chi^{(2)}(\omega_3, \omega_2, \omega_1) = \frac{\epsilon_0^2 ma}{N^2\mathrm{e}^3} \chi^{(1)}(\omega_3)\chi^{(1)}(\omega_2)\chi^{(1)}(\omega_1) \tag{3.16}$$

Given reasonable values ($N = 10^{22}\,\mathrm{cm}^{-3}$, $d = 3\,\text{Å}$, $\omega_0 = 10^{16}\,\mathrm{rad/s}$, $a \sim \omega_0^2/d$) we obtain that the linear susceptibility is of the order of unity. The second order nonlinear susceptibility presents a value around $10^{-12}\,\mathrm{m/V}$. The second order contribution will be

comparable to the linear response when the external fields are of the order of magnitude of the characteristic atomic electric field ($E_{at} = 5.14 \times 10^{11}$ V/m).

Centrosymmetric vs Non-centrosymmetric

The restoring force proposed in the equation of motion of the anharmonic oscillator (equations (3.1) and (3.2)) was defined as $F \propto x + x^2$ which corresponds to the potential $U(x) \propto x^2 + x^3$. While a non-centrosymmetric material can be accurately described with this kind of potential, centrosymmetric materials cannot. Due to the symmetry of such materials, inversion symmetry is required ($U(x) = U(-x)$) and the potential will be of the form $U(x) \propto x^2 + x^4$. In these materials the second-order nonlinear processes vanish, and the first observable nonlinear effects are directly third-order.

3.2.3 Second order vs third order processes

The strength of the nonlinearity induced in a material is quantified by the optical susceptibility. As explained in section 3.2.2, the order of magnitude of the nonlinear susceptibility $\chi^{(i)}$ values can be approximated to:

$$\frac{\chi^{(1)}}{E_{at}}, \frac{\chi^{(1)}}{E_{at}^2} ... \tag{3.17}$$

Higher order nonlinearities are therefore more difficult to see than low order ones. Second harmonic generation is a good example of an easily seen nonlinear effect: it can be observed from a single pass with a CW laser, and SDLs with intracavity SHG are relatively simple to build. Since the process efficiency increases with the intensity of the fundamental fields, higher nonlinear effects are difficult to produce in CW operation; pulsed lasers are the common solution [12, 13].

As noted in section 3.2.2, centrosymmetric materials do not exhibit second order nonlinear processes due to the symmetry of their atomic structure. This conveniently separates second order and third order processes, avoiding competition when the third order process is desired.

3.2.4 Energy conservation

It is a fundamental law of physics that energy can neither be created nor destroyed. As stated by the first law of thermodynamics every closed system must satisfy energy conservation, which means energy is always transformed from one form to another.

$$\Delta E = 0 \tag{3.18}$$

We can think of our "input beam – crystal – output beam" system as being a closed system. Moreover, sum-frequency generation (and by extension second harmonic generation) is a parametric process, which means it does not change the quantum state of the crystal. Let's assume the crystal does not absorb our wavelengths (as in the case of LBO or BBO at 675 nm – 337 nm) and that no other processes are present. This is a sensible assumption, since it is what we observe in the laboratory. The energy is then never stored in the crystal. The energy simply transforms from input photons, at frequencies w_1 and w_2, to output photons, at frequency w_3. Second order, frequency up-conversion is therefore a three photon process. In the particular case of second harmonic generation, two input photons must be annihilated so an output photon with twice their energy is created. Mathematically this is expressed:

$$\Delta E = \hbar\omega_3 - (\hbar\omega_1 + \hbar\omega_2) \tag{3.19}$$

Since this expression equals 0 by means of energy conservation, we see that $\omega_3 = \omega_1 + \omega_2$.

3.2.5 Momentum conservation

Another conservation law, this time related to Newton's first law of motion, is that the momentum of a system remains constant in the absence of external forces.

$$\Delta \boldsymbol{p} = 0 \tag{3.20}$$

Applied to our closed system of converting photons, we express this conservation law as:

$$\Delta \boldsymbol{k} = \boldsymbol{k_3} - (\boldsymbol{k_1} + \boldsymbol{k_2}) = 0 \tag{3.21}$$

Where we have defined the wavevector modulus as:

$$k = \frac{2\pi n}{\lambda} \tag{3.22}$$

It is important to notice the implications of the presence of the refractive index n in the last equation: dispersion plays a key role in frequency conversion. To illustrate this, let's focus again on the simple SHG process, in which $\lambda_2 = \lambda_1$ and $\lambda_3 = \frac{1}{2}\lambda_1$ (by definition). From here we obtain, simplifying equation (3.21):

$$\frac{n_3}{\lambda_3} = 2\frac{n_1}{\lambda_1} \quad \Rightarrow \quad n_3 = n_1 \tag{3.23}$$

Setting both refractive indices equal implies both beams will travel with the same speed inside the nonlinear material. This has profound implications regarding the phase of each beam. For this reason, equation (3.21) is most commonly known as the phase matching condition.

Phase matching

When the fundamental beam propagates through a nonlinear medium generating second harmonic, the second harmonic photons are produced from the beginning to the end of the crystal. We can imagine the crystal composed of very thin slices, all of which generate second harmonic. The output beam we observe at the exit of the crystal is the result of the interference of all these small contributions. Because the fundamental beam is of course in phase with itself, the second harmonic fields generated will keep the fundamental phase. However, due to dispersion, when the several second harmonic fields propagate along the crystal the phase will, in general, not be maintained (figure 3.2a). Indeed, the phase difference between two beams propagating through a medium with different refractive indices is not constant. This could effectively mean destructive interference at the end of the crystal and second harmonic would not be observed.

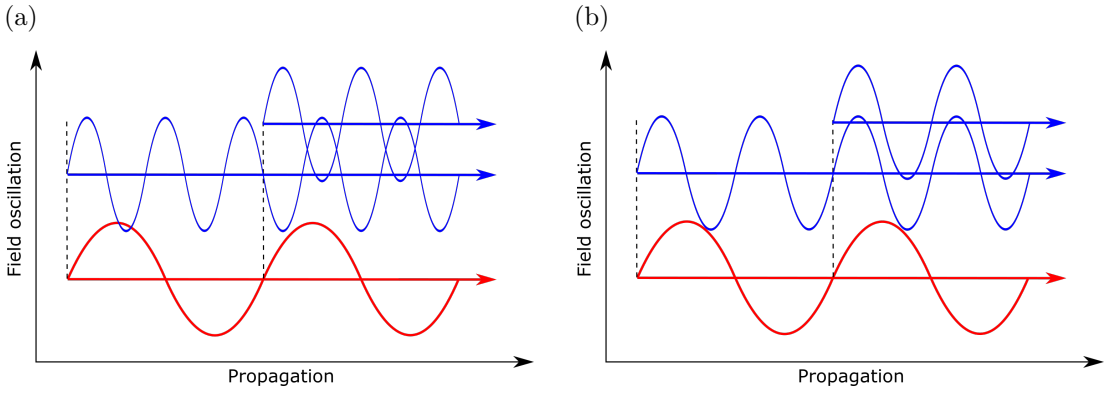

Figure 3.2: Representation of fundamental and SHG fields in phase-mismatching (a) and phase matching (b) configurations. Phase matching is required for constructive interference of the multiple SHG components.

If both beams travel with the same refractive index, however, the phase of all second harmonic contributions will be preserved over the whole crystal length and all the SHG contributions will interfere constructively, adding up to the total SHG output power (figure 3.2b).

A total phase mismatch does not occur instantly, but rather it happens over an extended length. If the nonlinear crystal is shorter than the coherence length there is no need for phase matching considerations, as said crystal length would be within the coherent build-up length of the interaction.

$$l_c = \frac{2}{\Delta k} \tag{3.24}$$

However this distance is relatively short ($l_c <$ mm, typically $l_c \sim$ 10s of µm): longer crystal lengths are required to produce sufficient output power. In general, due to dispersion, the refractive index is wavelength dependent and phase matching will not naturally occur. To be able to set the conditions for momentum conservation we make use of a property of certain materials: birefringence.

Phase matching conditions in crystals are different for every wavelength involved and the materials used. Only certain materials will offer phase matching for a set of given wavelengths, and those materials do not necessarily offer the highest nonlinear coefficient. Ultraviolet wavelengths are especially challenging in terms of crystal availability, for phase matching, performance and transmission limitations. For this reason, there is an enormous amount of research worldwide dedicated to the design and development of better nonlinear materials.

3.2.6 Birefringence

Birefringence means that the refractive index depends on the direction of polarization of the light. This is not a nonlinear effect, but a well-known part of linear optics and a characteristic of the structure of the material. Birefringence is not present in isotropic materials, such as those with cubic structure. The simplest case corresponds to uniaxial materials, which present a single anisotropy axis. Biaxial materials present three characteristic refractive indices, corresponding to the three principal axes of such materials. In our experiments all crystals used are, or can be considered, uniaxial (LBO is a biaxial crystal, which in this case is cut so the direction of propagation matches one of the crystal axes, making it uniaxial in effect).

For a uniaxial crystal two principal axes can be defined: the ordinary and extraordinary axis. When the light is linearly polarized in those directions, it will exhibit different refractive indices n_o and n_e. More interestingly, if the polarization happens to be at an angle between these two axes the refractive index takes an intermediate value defined as:

$$\frac{1}{n_e(\theta)^2} = \frac{\cos^2(\theta)}{n_o^2} + \frac{\sin^2(\theta)}{n_e^2} \tag{3.25}$$

Where θ is the angle of propagation with respect to the extraordinary axis.

We therefore find here a powerful mechanism to avoid phase mismatch over any crystal length. Going back to the example of second harmonic generation, if the fundamental beam travels with ordinary polarization, it is generally possible to find an angle at which the second harmonic beam can travel with extraordinary polarization exhibiting the same refractive index. This idea is depicted in figures 3.3 and 3.4.

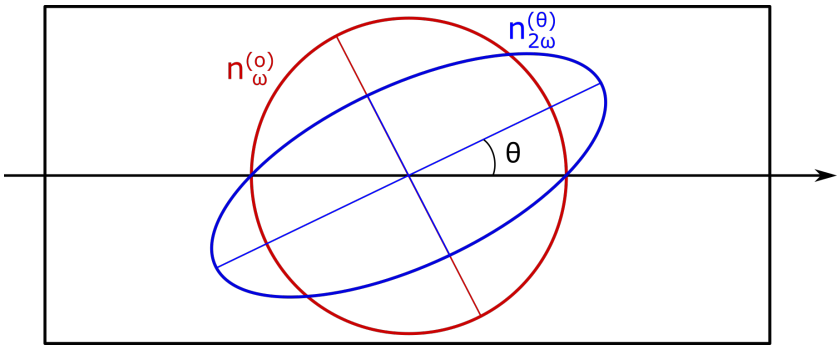

Figure 3.3: Refractive indices for fundamental (ordinary) and second harmonic (extraordinary) in phase-matched SHG. The arrow marks the wavevector direction. Second harmonic polarization is vertical while fundamental polarization is perpendicular to the screen.

This phase matching technique is called critical phase matching, alluding to the sensitivity to crystal misalignment. Moreover, when light travels with an angle from the optic axis in birefringent materials it suffers an effect called walk-off, negatively affecting beam quality, focusing limit, frequency conversion, etc. as explained in the following section.

Depending on the particular characteristics of each material, it is possible to find two different configurations for the polarization of the beams:

- Type-I phase matching, when the input beams have the same polarization (typically ordinary polarization). The generated beam would have perpendicular polarization.

- Type-II phase matching, when the input beams have perpendicular polarizations (one ordinary, one extraordinary). The polarization of the generated beam would depend on the material.

An alternative technique is non-critical phase matching, which uses the temperature dependence of the refractive index to match the refractive index of the ordinary and extraordinary axis. This technique avoids the walk-off effect since propagation occurs on axis. The drawback is that the temperature required may be significantly higher than

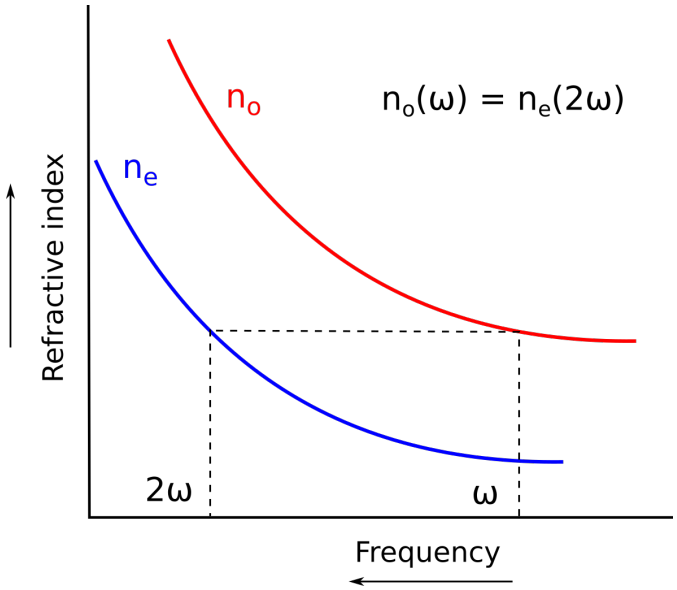

Figure 3.4: Critical phase matching. Extraordinary refractive index of second harmonic and ordinary refractive index of fundamental take the same value under particular circumstances.

room temperature so that crystal ovens are often needed. The temperature difference from room temperature is proportional to the separation from axis required in critical phase matching, thus having little to no effect in some cases. For example, SHG in LBO at 675 nm requires a phase matching angle of $\phi = 47°$. An increase of 200 K in the crystal temperature barely changes ϕ by one degree.

3.2.7 Walk-off

When the wavevector k propagates with extraordinary polarization at an angle θ from the optic axis, the Poynting vector will not be parallel to k. On the contrary, the energy flux will drift from the k direction with an angle ρ that can be expressed as:

$$\rho = -\frac{1}{n_e(\theta)} \frac{\partial n_e(\theta)}{\partial \theta} \tag{3.26}$$

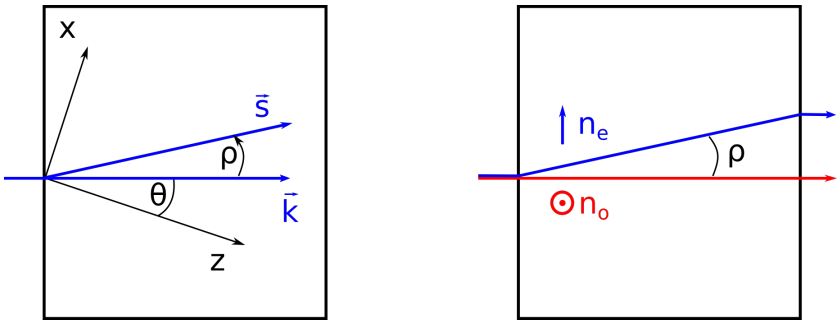

Figure 3.5: Wavevector and Poynting vector featuring walk-off effect inside a birefringent material, with crystal axis defined by x and z (y axis would be perpendicular to the drawing) (left). Walk-off affecting the extraordinary polarization component of the beam (right).

As a result, at the exit of the material, light with extraordinary polarization will be separated from light with ordinary polarization, as can be seen in figure 3.5. We can immediately see that this would cause separation between fundamental and frequency converted beams.

Beam separation, however, is not the only effect walk-off has, especially when considering frequency conversion. Beam focusing is also affected, being more limited in the walk-off direction. This causes asymmetry between sagittal and tangential components and different divergence angles (assuming they were equal at the beginning), diminishing the beam quality. Moreover, walk-off is closely linked to frequency conversion, with the total output power strongly depending on the walk-off angle. We shall see the precise effect walk-off has on our system in the following chapters.

3.3 Frequency conversion

During this chapter we have reviewed nonlinear optics and the broad range of different processes that arise from it. We have reviewed its origin and the effects that can affect nonlinear beams. We shall now look more in detail at the two processes that we use in our experiment to generate third harmonic emission. As described in Chapter 4, we will produce second harmonic generation from a fundamental beam at 674 nm, obtaining

Table 3.1: Comparison of different intracavity frequency tripling setups with the main characteristics of the nonlinear crystals used.

Author	λ_0 (nm)	SHG crystal	d_{eff} (pm/V)	ρ (mrad)	SFG crystal	d_{eff} (pm/V)	ρ (mrad)
Wu [15]	1064	LBO (ooe)	0.83	6.88	BBO (ooe)	2.02	72.31
Roissé [16]	1064	KTP (eoe)	3.58	3.16 / 4.13	LBO (ooe)	0.72	18.18
Sun [17]	1319	LBO (eeo)	0.81	5.33 / 5.33	LBO non-critical	0.69	–
Shu [14]	1064	LBO (ooe)	0.83	6.88	BBO (eoe)	1.29	71.49 / 77.86
This work	674	LBO (ooe)	0.61	18.93	BBO (ooe)	1.55	82.60

a laser beam at 337 nm. These two beams can then be mixed via sum-frequency generation, to produce third harmonic emission at 224 nm. Both processes occur inside the SDL external cavity, thus providing a large amount of fundamental power, very much needed in any nonlinear process as explained in section 3.1.2. This technique has been successfully employed previously, both using SDLs [14] or other gain material [15–17]. These previous demonstrations have been carried out at longer wavelengths, and the relevant data are summarized in table 3.1. This table also shows how working with shorter wavelengths is more challenging.

As compared with conversion from a fundamental wavelength of 1064 nm, when starting from 674 nm the nonlinear coefficient of the SHG process decreases by 25 %, while the walk-off angle is three times larger. In other crystals often used, such as KTP, a fundamental visible wavelength is out of the range of phase matching. The larger walk-off angle produces a larger separation between fundamental and second harmonic beams (negligible in previous examples). While LBO for SFG offers a low nonlinear

coefficient as compared with BBO, walk-off in the latter is always large, decreasing the maximum achievable power as described in Chapter 5.

3.3.1 Second harmonic generation

We already mentioned second harmonic generation at the beginning of this chapter. This process converts light of a given fundamental frequency into its second harmonic (doubling that fundamental frequency). It is the most common nonlinear optical process of all, in particular it is used for conversion from the omnipresent laser emission at 1064 nm to the visible green emission at 532 nm. The superior performance of 1064 lasers together with simple SHG has provided a magnificent workaround for the semiconductor green gap for many applications (notably common green laser pointers). This section will look at the process in more detail.

Phase matching condition

Phase matching is a sine qua non condition, and the first calculation that needs to be done if this process is to be implemented. In the case of type-I SHG the phase matching condition is quickly transformed into a neat equality.

$$\Delta k = k_2 - 2k_1 = 0 \quad \Rightarrow \quad \frac{n_{\omega_2} 2\omega_1}{c} = 2\frac{n_{\omega_1}\omega_1}{c} \quad \Rightarrow \quad n_{\omega_2} = n_{\omega_1} \tag{3.27}$$

We can then cut a birefringent crystal so that the fundamental and second harmonic beams, travelling through it with different polarizations, will show equal values of their respective refractive indices.

Output power

Starting with the publication of the first observation of second harmonic generation by Franken *et al.* in 1961 [7], a number of papers were dedicated to study the interaction between light waves in nonlinear dielectrics, from particular cases to the general solution [18–24]. Thanks to those efforts, we can now describe the output power of SHG with the equation:

$$P_3 = \frac{16\pi^2 d_{\text{eff}}^2}{\epsilon_0 c \lambda_1^3 n_1 n_3} e^{-\alpha L} P_1^2 L h(\sigma, \beta, \kappa, \xi, \mu) \tag{3.28}$$

Here, the universal constants ϵ_0 and c take the expected values (in S.I. units), n_1 and n_3 are the refractive indices of the material for the involved wavelengths, λ_1 is the fundamental wavelength and d_{eff} is the effective nonlinear coefficient of the material. α takes into consideration the fundamental and second harmonic losses. The exponential equals 1 if the light is not absorbed by the material. The h function accounts for the walk-off effect, phase matching, focusing... produced in the nonlinear conversion, and takes a value between 0 and 1. This function will be studied in detail in Chapter 5 for our particular system, and is described in the following section. The derivation of this equation will not be explained in this thesis, since it can be found in its original form here [23]. A modern derivation can be also found elsewhere ([25]).

It is important to note that for loose focusing (i.e. $L << b$) the value of h tends to L/b. The confocal parameter is defined as twice the Rayleigh length ($b = 2z_0$). In this case the output power of the conversion would be proportional to L^2. This is not the case for tight focusing, in particular for large values of the walk-off angle.

Optimum focusing / crystal length

It could be expected that the optimum focusing, in the absence of walk-off, occurs when the crystal length is approximately twice the Rayleigh length (equal to the confocal parameter $b = 2z_0$). Actually, it was proved by Boyd and Kleinman [23] that the optimum condition happens for a phase-mismatch of $\Delta k = 3.2/L$, which they calculated to be $L = 2.8b$; although this value decreases to $L = \pi b/2$ for perfect phase matching, as calculated by Bjorkholm [21]. Nevertheless, if the walk-off angle is large, the optimum phase matching tends towards 0 and its curve becomes flatter, making it less critical to achieve the perfect condition.

3.3.2 Sum-frequency generation

Sum frequency generation is in fact the general case of SHG: two photons of different energies interact with the material to produce photons of a third energy (while in SHG the input photons have all the same energy). In both cases, each conversion that takes place involves three photons.

Phase matching

The phase matching condition in sum-frequency conversion differs from the special case of type-I SHG. Since three different wavelengths must be phase-matched, there is no configuration offering the same refractive index for each of the beams. In the case of SFG the solution would be:

$$\begin{aligned} \Delta k &= k_3 - k_1 - k_2 = 0 \\ \Rightarrow \quad & \frac{n_{\omega_3} 3\omega_1}{c} = \frac{n_{\omega_2} 2\omega_1}{c} + \frac{n_{\omega_1}\omega_1}{c} \\ \Rightarrow \quad & n_{\omega_3} = \frac{2n_{\omega_2} + n_{\omega_1}}{3} \end{aligned} \tag{3.29}$$

While in some particular cases the desired wavelengths (or the crystal) will force us to use a particular type of phase matching, in general several configurations will be available, and the preferred one must be chosen to favour the nonlinear coefficient or the desired configuration of the polarization of the different beams.

Output power

The output power from this process is calculated in the same manner as the SHG output power, obtaining a very similar equation. Again, the reader can refer to the paper of Boyd and Kleinman from 1968 [23] to see the original derivation.

$$P_3 = \frac{32\pi^2 d_{\text{eff}}^2}{\epsilon_0 c \lambda_1 \lambda_2 \lambda_3 n_3^2} e^{-\alpha L} P_1 P_2 L h(\sigma, \beta, \kappa, \xi, \mu) \tag{3.30}$$

As in equation (3.28), the universal constants are in S.I. units, n_i are the refractive indices for the corresponding wavelengths λ_i and the exponential term takes into account the absorption of the material at every wavelength. We find again the h function (already mentioned in the SHG process) accounting for walk-off, focusing and phase matching effects. This function is described in the next section, and the parameters will be defined in Chapter 5.

Boyd and Kleinman h function

Nonlinear frequency conversion effects take place all along the nonlinear crystal. Providing the necessary conditions are fulfilled, frequency mixing will occur from beginning to end of the given crystal, thus generating output fields at each point along the propagation axis. We have already described how phase matching is needed so the output fields interfere constructively with each other, but despite the importance of accurate phase matching, the fields' interference is much more complex. The input beams are usually focused inside the crystal, since the conversion efficiency is proportional to the photon density, and the output fields will also follow the focusing geometry (for the particular wavelength). Moreover, walk-off is generally present, in the case of type-I SFG affecting the output beam, effectively displacing the output fields from the optical axis. The h function comes from calculating the coherent interference by integrating the generated fields over the crystal length.

Boyd and Kleinman's study, however, is limited to the mixing of Gaussian beams with the same confocal parameter. Of course that is the ideal case, and when dealing with separated input lasers one should aim to build the system so both beams have the same confocal parameter, maximizing the beam overlap. In some systems, such as the one described in this work, one input depends on the other (e.g. second harmonic, generated by the fundamental, is directly used as input), which makes it unviable to focus them both with the same confocal parameter. An extension of the theory of parametric interaction of focusing Gaussian beams is therefore needed. Fortunately Guha and Falk addressed this issue in 1980 [26], generalizing Boyd and Kleinman's h function to input beams with different confocal parameters. The value of h they calculated reduces to that of Boyd and Kleinman when both beams have the same confocal parameter.

An extended description of this equation and parameters involved will be given in Chapter 5, however we present it here for completeness. Of particular importance are

the focusing parameters ξ_1 and ξ_2, and the walk-off parameter B. This equation has to be solved numerically for each set of input parameters.

$$h = \frac{1}{4\xi_4} I \tag{3.31a}$$

$$I = \int_0^1 \int_0^1 \mathrm{d}z_1 \, \mathrm{d}z_2 \times \frac{\exp\left[i\Delta k L \left(z_1 - z_2\right)\right] \exp\left[-\left({}^{4B^2}/_{\beta}\right)\left(z_1 - z_2\right)^2 f\right]}{\left(z_1 - A_1\right)\left(z_2 - A_1^*\right) + C_1} \tag{3.31b}$$

While a number of plots are given in the original paper, we have implemented the numerical calculation of the h function to be able to produce detailed estimations for our experimental conditions, allowing for a more accurate study of the process as can be seen in Chapter 5.

3.3.3 Optimum efficiency

Any given laser has an optimum value of output power as a result of optimum output coupling. For this optimum output coupling the gain medium is able to handle the output (useful) losses, giving the maximum output power possible (for a given pump power). Considering nonlinear conversion, there should then be an optimum conversion efficiency based on the optimum output coupling of the laser. This optimum conversion efficiency may not be achievable in every setup, in particular in CW lasers, but it is still interesting to calculate and keep in mind for further optimization. Considering small conversion efficiencies and no depletion of the fundamental beam for either process, we can relate them with the optimum output coupling as:

$$\mathrm{OC} \approx \eta_{12} + \eta_{13} \tag{3.32}$$

Where OC is the optimum output coupling and η_{ij} the conversion efficiencies for fundamental to second and to third harmonic. For the fundamental intracavity laser, all frequency conversion steps (both to second and to third harmonic) are seen as losses. Third harmonic output is in our case the desired output, the useful loss. We can express the conversion efficiency from fundamental to second and to third harmonic in terms of photon energy (E_i). If n_i is the number of photons at wavelength λ_i the conversion efficiency can be calculated as:

$$\eta_{12} = \frac{n_2 E_2}{n_1 E_1} = \frac{2n_2}{n_1} \tag{3.33}$$

$$\eta_{13} = \frac{n_3 E_3}{n_1 E_1} = \frac{3n_3}{n_1} \tag{3.34}$$

Since we are not interested in having second harmonic output, ideally we would like to convert all second harmonic photons into third harmonic photons: $n_3 = n_2$. Therefore we can express equation (3.34) as:

$$\eta_{13} = \frac{3}{2}\eta_{12} \tag{3.35}$$

Substituting in equation (3.32), we find the following ratios:

$$\eta_{12} \approx \frac{2}{5}\mathrm{OC} \tag{3.36}$$

$$\eta_{13} \approx \frac{3}{5}\mathrm{OC} \tag{3.37}$$

Given that our laser presents an optimum output coupling close to 3 %, the optimum conversion efficiencies for SHG and SFG can be calculated to be approximately 1.2 %

and 1.8 % respectively. These values are far from the conversion efficiencies achievable with an intracavity cascaded tripling system such as the one presented in this work, especially when working in continuous-wave operation, as we will see in the next chapter.

3.4 Conclusion

Atomic oscillation of crystals and fundamental conservation laws can be exploited, by means of birefringence, to achieve the classical impossibility of photon frequency conversion. In this chapter we have reviewed the theory behind frequency conversion, with particular focus on second harmonic generation (SHG) and sum-frequency generation (SFG), the nonlinear processes used in this work.

The basic dependence of these nonlinear processes with input power, crystal nonlinear coefficient or crystal length is readily appreciated from this introduction. However, the amount of variables involved in frequency conversion is vast (walk-off angle, beam size, focusing... to name a few). Their effect can be quantified in Boyd and Kleinman's h function and a closer look will be presented in Chapter 5, in relation to the experimental results shown in the following chapter.

References

[1] J. Kerr. "A new relation between electricity and light: Dielectrified media birefringent". In: *Philosophical Magazine Series 4* 50.332 (1875), pp. 337–348. DOI: 10.1080/14786447508641302.

[2] J. Kerr. "A new relation between electricity and light: Dielectrified media birefringent (second paper)". In: *Philosophical Magazine Series 4* 50.333 (1875), pp. 446–458. DOI: 10.1080/14786447508641319.

[3] R. Boyd. *Nonlinear optics*. 3rd. Academic Press, 2008, p. 620. DOI: 10.1016/B978-0-12-369470-6.

[4] J. P. Gordon, H. J. Zeiger, and C. H. Townes. "Molecular microwave oscillator and new hyperfine structure in the microwave spectrum of NH_3". In: *Physical Review* 95.1 (1954), pp. 282–284. DOI: 10.1103/PhysRev.95.282.

[5] J. P. Gordon, H. J. Zeiger, and C. H. Townes. "The maser-new type of microwave amplifier, frequency standard, and spectrometer". In: *Physical Review* 99.4 (1955), pp. 1264–1274. DOI: 10.1103/PhysRev.99.1264.

[6] T. H. Maiman. "Optical and microwave-optical experiments in ruby". In: *Physical Review Letters* 4.11 (1960), pp. 564–566. DOI: 10.1103/PhysRevLett.4.564.

[7] P. A. Franken, A. E. Hill, C. W. Peters, and G. Weinreich. "Generation of Optical Harmonics". In: *Physical Review Letters* 7.4 (Aug. 1961), pp. 118–119. DOI: 10.1103/PhysRevLett.7.118.

[8] A. F. J. Levy. "The Lorentz oscillator model". In: *Essential Classical Mechanics for Device Physics*. San Rafael: Morgan & Claypool Publishers, 2016. Chap. 5, pp. 5.1–5.21. DOI: 10.1088/978-1-6817-4413-1ch5.

[9] J. W. S. B. Rayleigh. *The theory of sound I*. 2nd. London: Macmillan and CO, 1894, p. 544.

[10] J. Larmor. "On the theory of the magnetic influence on spectra; and on the radiation from moving ions". In: *Philosophical Magazine Series 5* 44.271 (1897), pp. 503–512. DOI: 10.1080/14786449708621095.

[11] Y. R. Shen. *The principles of nonlinear optics*. 1984th ed. New York: J. Wiley, 1984, p. 563.

[12] Y. K. Yap, M. Inagaki, S. Nakajima, Y. Mori, and T. Sasaki. "High-power fourth- and fifth-harmonic generation of a Nd:YAG laser by means of a $CsLiB_6O_{10}$". In: *Optics Letters* 21.17 (Sept. 1996), p. 1348. DOI: 10.1364/OL.21.001348.

[13] P. Koch, J. Bartschke, and J. A. L'huillier. "Single-mode deep-UV light source at 1917 nm by seventh-harmonic generation of a high-power, Q-switched, injection-locked 1342 nm Nd:YVO_4 laser". In: *Applied Optics* 55.8 (Mar. 2016), p. 1871. DOI: 10.1364/AO.55.001871.

[14] Q.-z. Shu, A. L. Caprara, J. D. Berger, D. W. Anthon, H. Jerman, and L. Spinelli. "Intracavity-tripled optically-pumped semiconductor laser at 355 nm". In: *Lasers and Applications in Science and Engineering*. Ed. by W. A. Clarkson, N. Hodgson, and R. K. Shori. Vol. 7193. San Jose: SPIE, Feb. 2009, p. 719319. DOI: 10.1117/12.816073.

[15] R. Wu. "High-efficiency and compact blue source: intracavity frequency tripling by using LBO and BBO without the influence of birefringence". In: *Applied Optics* 32.6 (Feb. 1993), p. 971. DOI: 10.1364/AO.32.000971.

[16] E. Roissé, V. Couderc, A. Barthélémy, and F. Louradour. "Intracavity frequency-tripling of actively mode-locked diode-pumped Nd:YAG laser". In: *Applied Physics B: Lasers and Optics* 69.2 (Aug. 1999), pp. 89–91. DOI: 10.1007/s003400050776.

[17] Z. Sun, R. Li, Y. Bi, X. Yang, Y. Bo, W. Hou, X. Lin, H. Zhang, D. Cui, and Z. Xu. "Generation of 4.3-W coherent blue light by frequency-tripling of a side-pumped Nd:YAG laser in LBO crystals". In: *Optics Express* 12.26 (2004), p. 6428. DOI: 10.1364/OPEX.12.006428.

[18] J. A. Armstrong, N. Bloembergen, J. Ducuing, and P. S. Pershan. "Interactions between Light Waves in a Nonlinear Dielectric". In: *Physical Review* 127.6 (Sept. 1962), pp. 1918–1939. DOI: 10.1103/PhysRev.127.1918.

[19] D. A. Kleinman. "Theory of Second Harmonic Generation of Light". In: *Physical Review* 128.4 (Nov. 1962), pp. 1761–1775. DOI: 10.1103/PhysRev.128.1761.

[20] G. D. Boyd, A. Ashkin, J. M. Dziedzic, and D. A. Kleinman. "Second-Harmonic Generation of Light with Double Refraction". In: *Physical Review* 137.4A (Feb. 1965), A1305–A1320. DOI: 10.1103/PhysRev.137.A1305.

[21] J. Bjorkholm. "Optical Second-Harmonic Generation Using a Focused Gaussian Laser Beam". In: *Physical Review* 142 (1966), pp. 126–136. DOI: 10.1103/PhysRev.142.126.

[22] D. A. Kleinman, A. Ashkin, and G. D. Boyd. "Second-Harmonic Generation of Light by Focused Laser Beams". In: *Physical Review* 145.1 (May 1966), pp. 338–379. DOI: 10.1103/PhysRev.145.338.

[23] G. D. Boyd and D. A. Kleinman. "Parametric Interaction of Focused Gaussian Light Beams". In: *Journal of Applied Physics* 39.8 (1968), p. 3597. DOI: 10.1063/1.1656831.

[24] R. Smith. "Theory of intracavity optical second-harmonic generation". In: *IEEE Journal of Quantum Electronics* 6.4 (Apr. 1970), pp. 215–223. DOI: 10.1109/JQE.1970.1076440.

[25] W. P. Risk, T. R. Gosnell, and A. V. Nurmikko. *Compact Blue-Green Lasers*. April. Cambridge: Cambridge University Press, 2003. DOI: 10.1017/CBO9780511606502.

[26] S. Guha and J. Falk. "The effects of focusing in the three-frequency parametric upconverter". In: *Journal of Applied Physics* 51.1 (Jan. 1980), pp. 50–60. DOI: 10.1063/1.327353.

CHAPTER 4

THG results

4.1 Introduction

The quest to reach laser wavelengths outside the common emission bands of materials began almost immediately after the first demonstration of the laser, using both nonlinear crystals and gas media to achieve frequency conversion [1–5]. Second harmonic generation in these early days provided an efficient means to obtain visible radiation, and doubling the 1064 nm output from a Nd:YAG crystal to achieve green emission is still probably the most common frequency conversion process carried out nowadays. Shorter wavelengths required further conversion, either from the second harmonic output of a previous process or making use of higher (i.e. single-step third, fourth...) harmonic generation. However the efficiency of the direct methods decreases rapidly since they are higher order processes, as explained in Chapter 3.

Third harmonic generation (THG) by means of two consecutive nonlinear frequency conversion steps – instead of making use of the direct, single-step, third-order process just mentioned – was soon reported as an efficient method to achieve ultraviolet wavelengths [6, 7]: the third harmonic of neodymium lasers emitting at 1064 nm, 355 nm,

fell within the near ultraviolet region, and conversion efficiency up to 30 % was reported. A more theoretical approach was devised by Craxton [8, 9], with demonstrated higher efficiency [10] of up to 80 %. These first implementations of THG were made outside of the laser cavities, although sometimes making use of external resonators, with pulsed fundamental lasers. Pulsed lasers are capable of high frequency conversion efficiencies thanks to the high intensity pulses, well over MW/cm^2, and so any kind of resonator is not necessarily needed. Continuous-wave lasers, however, do need resonators to increase the photon density inside the nonlinear crystal at any given time. External resonators work well in this regard, and provide flexibility to align the input beams as required, making it possible to greatly optimize the system.

The use of the SHG + SFG implementation for intracavity tripling was first shown by Wu in 1993 [11]. The advantage of this method is the greatly reduced complexity of the system since, apart from building external resonators, these need to be stabilized (sketched in figure 4.1). Moreover, precise configuration is needed if the external resonator is to confine the laser power. If we consider the single cavity system, the intracavity power of the fundamental laser is usually very high (our system can reach over 100 W of intracavity power using only 5 W of pump power so long as intracavity losses are kept to a minimum). Since both second harmonic generation and sum-frequency generation can take place inside the same fundamental cavity, the simplification of the experimental setup is considerable. Intermediate solutions have also being proposed, as described by the theoretical study developed by Koch and Moore [12]. Despite the high intracavity fields possible in continuous-wave operation, most of the work has been developed with pulsed lasers [13–15], with the enormous intensities achieved simplifying the process. Intracavity tripling in a continuous wave SDL was first demonstrated by Shu *et al.* [16] with remarkable results: the authors achieved 450 mW of third harmonic output power ($\lambda = 355\,\text{nm}$) with 18 W of pump power.

In this chapter, a frequency tripling experiment will be described, using a red SDL ($\lambda = 675\,\text{nm}$) as the fundamental laser, and thus reaching deep ultraviolet emission

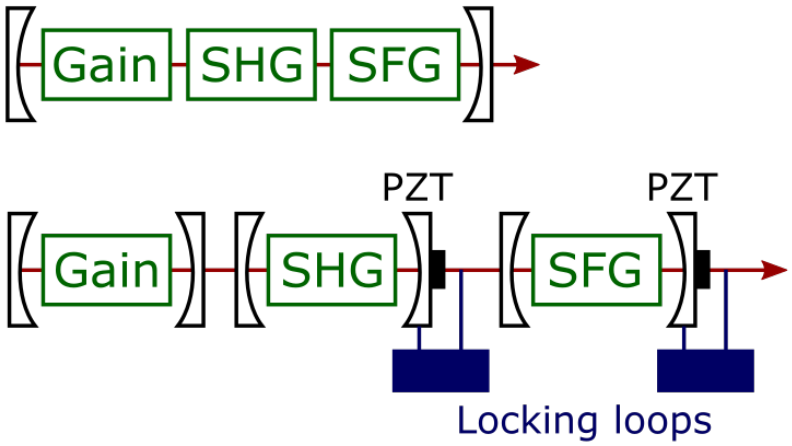

Figure 4.1: Intracavity tripling vs external resonators schema. Tripling inside the fundamental cavity greatly simplifies the optical resonator system and makes it compact. External resonators require precise cavity length control in order to minimize transmission losses. Stabilization loops (locking loops) are complex systems requiring e.g. reference cavity, amplifiers or further electronics. Required optical elements apart from gain element and nonlinear crystals are omitted since they are usually needed in both set-ups.

as laser output, at a wavelength of 224.5 nm. This is, to the authors' knowledge, the shortest wavelength emitted from an SDL to date, and the first implementation of intracavity tripling in a visible SDL.

While all the aforementioned previous work provides an excellent basis from which to build upon, we faced several difficulties caused by working with shorter wavelengths, such as beam separation or reduced conversion efficiency, due to higher walk-off parameters or even absorption. The cavity design is of paramount importance, and far from trivial due to the large number of factors to take into account. The nonlinear crystals have to be carefully chosen, although the choices are very limited. Mirror and intracavity element alignment can be a long process until the cavity is fully optimized. Finally, the relatively low power third harmonic beam must be efficiently coupled out of the cavity and detected.

There are a number of acronyms and abbreviations used within this chapter that will be clarified here:

- 'Pump beam', or 'pump power' refers to the pump laser used as the power source for the whole experiment. It is a commercially available frequency-doubled Nd:YVO_4 laser (Coherent Verdi) emitting at 532 nm with a maximum pump power of 5.5 W. This laser is focused onto the SDL gain medium to produce population inversion. Since an uncoated diamond heatspreader is being used on top of the SDL sample for improved cooling, the pump power reaching the sample, which we refer to as 'input power', is 82 % of the pump.

- 'Fundamental beam' refers to the SDL oscillating wavelength of around 674 nm. We may also refer to it, mostly when talking about beam power, as the intracavity power. It is the only beam resonating in the cavity, and since all the mirrors are highly reflective at this wavelength, its output power is small, on the order of a few milliwatts.

- 'SHG' stands for second harmonic generation. However, we may use this acronym to refer to the resulting beam of this process. This is a common practice in the field.

- 'THG' refers to third harmonic generation, and it really refers to a particular nonlinear process where three fundamental photons mix to produce another photon with three times the fundamental photon energy. However, this process is usually highly inefficient due to the small nonlinearity of the crystals available. THG may also be used to refer to the more efficient SHG plus SFG process, resulting in third harmonic generation as well, which is the meaning we will use here. As with SHG, we may use THG to refer to the third harmonic beam resulting from the process.

- 'SFG' stands for sum-frequency generation, and in our particular case it consists of mixing the fundamental photons with the second harmonic (SHG) photons to produce third harmonic (THG) photons.

4.2 Cavity design

As previously said, the design of an SDL cavity for third harmonic generation is not a trivial problem, since there are many factors that play a role in the particular requirements that the cavity needs to fulfil.

The main requirements are the three beam waists needed for the gain region and both nonlinear process regions:

- The SDL gain structure requires a beam size of ∼45 µm radius. This size provides a good photon density while avoiding thermal roll-over for pump power up to 5.5 W, as described in Chapter 2.

- SHG requires a beam waist of ∼20 µm radius. This size would be the optimum considering the size of our crystal and the fundamental wavelength, as defined by equation (5.10).

- SFG also requires a tight focus. While the optimum beam waist is ∼18 µm, this assumes the beam size of the second harmonic can also be precisely controlled. This, however, is not the case, since the second harmonic will be produced by the fundamental beam in the first nonlinear crystal and will then propagate through the cavity to reach the second nonlinear crystal. Its geometry is therefore defined by the existing cavity, and the waist at the SFG crystal will be larger than the optimum size. Since the second harmonic waist will be larger than desired, the fundamental waist has to be larger as well to improve the overlap. The calculations described in Chapter 5 suggest a beam size over 40 µm radius to be optimal, considering the divergence of the SHG beam.

While three beam waists may be achievable in a 4 mirror cavity, using 5 mirrors (or even 6) gives much more flexibility to the design, allowing for more customizable beam sizes and mirror distances.

The set-up has to accommodate the limitations that arise from working with standard optical equipment, in particular mounting arrangements, for a proof of concept experiment. A future system using custom engineered compact components will benefit from extended flexibility for the cavity design. For the current work there are some space constraints (as can be observed in figures 4.2 and 4.3 that need to be taken into account when designing the cavity, such as:

- The water-cooled SDL mount is relatively bulky and no other element can coincide in that space. The second arm of the cavity (M_2 to M_3) needs to be at least $\sim$100 mm longer than the first arm (SDL to M_2).

- The dual waveplate, being in a rotational mount, needs some clearance around the beam, making it difficult to fit in the region defined by the mirrors M_2 – M_3. The fourth arm (M_4 to M_5) of the cavity should therefore be longer than the third arm.

- While the folding angles of the mirrors are always kept as small as possible, the SHG crystal, with beams passing on either side (it is placed in the third arm) sets a relatively large minimum angle, narrowing the stability region of the cavity.

As described below, both frequency conversion processes use type-I phase matching, requiring the polarization of the second harmonic to be rotated between them. This is achieved with a dual waveplate: its effect on the second harmonic beam will be that of a half waveplate, rotating its polarization by 90°. The fundamental beam, also travelling through this waveplate, is not affected since the waveplate is designed as a full waveplate at this wavelength. This intracavity element is antireflection coated for

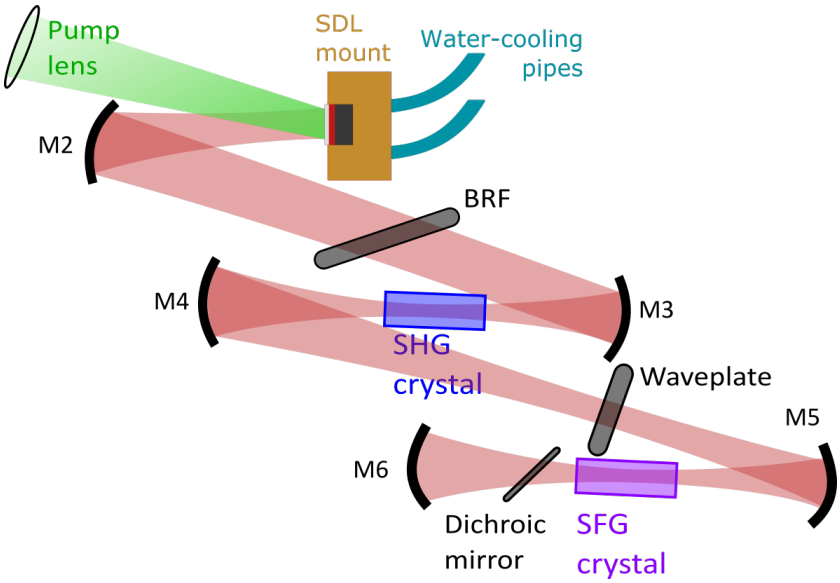

Figure 4.2: Schematic of a 6-mirror cavity with the required optics for intracavity tripling. Mounts holding the optics would occupy extra space.

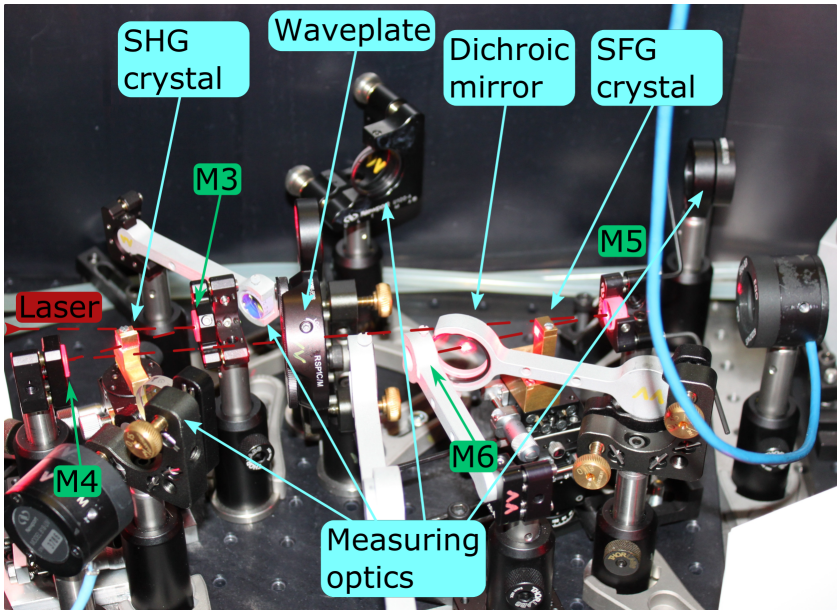

Figure 4.3: Picture of the 6-mirror setup during intracavity tripling. SDL, M2 and BRF are at the left of the picture and not appearing in view.

both the fundamental and the second harmonic wavelengths. The schematic of this behaviour is depicted in figure 4.4.

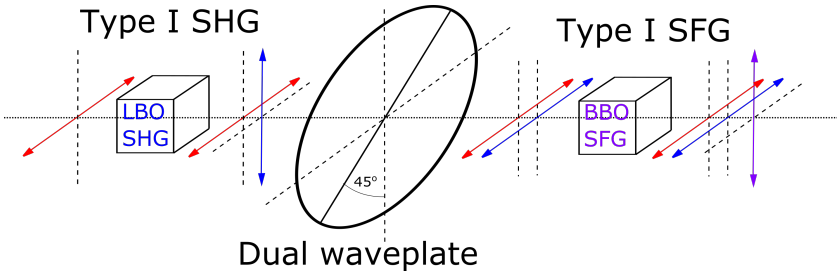

Figure 4.4: Schematic of the function of the dual waveplate.

The third harmonic beam is extracted from the cavity by means of an intracavity dichroic mirror. This eliminates absorption effects that would occur under transmission through one of the cavity mirrors and it has the added advantage of simplifying the coatings needed: placed at Brewster's angle, the loss for the fundamental beam is low even with no AR coatings.

4.3 Nonlinear crystals

The choice of the nonlinear crystals is critical for efficient frequency conversion processes. Unfortunately, at ultraviolet wavelengths, the available crystals are few. The most common ones are beta-barium borate (BaB_2O_4, BBO), lithium triborate (LiB_3O_5, LBO), and caesium lithium borate ($CsLiB_6O_{10}$, CLBO). The nonlinear properties of these three materials are far superior to any other available alternatives in this wavelength range.

4.3.1 SHG

Intracavity second harmonic generation, particularly in an SDL cavity (low loss tolerance), is usually achieved with type-I phase matching. Type-II phase matching (eoe configuration, due to the crystals being negative uniaxial) would add walk-off effects to the fundamental beam, without providing any particular advantage in this case.

Table 4.1: Nonlinear properties of the most suitable materials for SHG at 675 nm – 337 nm.

Crystal	d_{eff} (pm/V)	ρ (mrad)
BBO	1.95	76.81
LBO	0.61	19.01
CLBO	0.58	38.07

Second harmonic generation, from a fundamental wavelength of 675 nm to 337 nm, can be achieved in any of the aforementioned crystals. However, CLBO offers the lowest nonlinear coefficient and a significant walk-off angle and will therefore not be considered for this process (see table 4.1).

BBO offers a high nonlinear coefficient, allowing for stronger conversion, and it is usually the first choice when aiming for high output power at the second harmonic. The drawback of using this crystal is its walk-off angle, of over 76 mrad. This high walk-off forces a compromise between tight focusing and beam quality. At the same time it separates the fundamental and second harmonic beams (SHG beam would exit the crystal around 300 µm apart from the fundamental beam for a 7 mm BBO), which is not ideal for SFG downstream.

For this reason we believe that LBO is the most appropriate crystal for SHG in our particular experiment. The low walk-off angle keeps the beams closer together, while its nonlinear coefficient, being almost four times smaller than that of the BBO, is still one of the highest at these wavelengths.

We have chosen a 7 mm long crystal: long enough to produce tens of milliwatts of output power while not separating the beams more than a hundred of micrometres.

4.3.2 SFG

The crystal choice for sum-frequency generation, mixing 674 nm and 337 nm to produce 224.5 nm, is very limited: BBO stands out from any other material, despite its large walk-off, due to its high nonlinear coefficient. LBO and CLBO do not have phase-matching at such short wavelengths, and other possible materials, such as CBBF or RBBF, present nonlinear coefficients at least five times smaller, yet with large walk-off angles.

It is still possible to choose the phase-matching desired (data summarised in table 4.2):

- Type-I phase-matching presents the largest nonlinear coefficient and a large walk-off affecting only the third harmonic beam. It is necessary to rotate the polarization of the second harmonic beam, so it matches the polarization of the fundamental (in type-I SHG it is produced with polarization perpendicular to that of the fundamental).

- Type-II phase-matching offers a nonlinear coefficient that is over 25 times smaller than that of type-I phase-matching ($d_{\mathrm{eoe}} = 0.039 d_{\mathrm{ooe}}$). This alone filters out type-II phase-matching as an option for SFG, despite the walk-off angle suffered by the third harmonic beam in this case being considerably smaller than in the previous case (although it adds walk-off effect to the fundamental beam). The polarization of the input beams would not need to be modified prior to this nonlinear process, reducing one intracavity element. However, all the advantages that this configuration presents are not capable of compensating for the lower nonlinear coefficient, since the dependence of output power is quadratic with the nonlinear coefficient ($P_{\mathrm{out}} \propto d^2$). Moreover, as we will see in Chapter 5, the walk-off affecting the fundamental would cause a reduction of 5 times the maximum value, while the losses in the intracavity power produced by the waveplate are negligible in comparison.

Table 4.2: Comparison of type-I and type-II SFG tripling from 675 nm in BBO.

Crystal	d_{eff} (pm/V)	ρ (mrad)
BBO: type-I PM	1.55	82.60
BBO: type-II PM	0.06	22.33 (ω) – 28.83 (3ω)

It is important to realise that BBO presents some absorption at 224.5 nm, the absorption coefficient being ($\alpha = 0.12\,\text{cm}^{-1}$). This produces absorption of 6 % over the length of our crystal (5 mm). The crystal length of 5 mm was chosen as a compromise between beam absorption, conversion efficiency and beam interaction length.

4.4 Optical elements characterization

Every optical element placed intracavity will cause losses to the fundamental intracavity power, and great attention should be given to antireflection coatings on each surface. Our system includes a birefringent filter, two nonlinear crystals, a waveplate and a dichroic mirror; all inside the cavity resonator.

Some elements, as in the case of the birefringent filter and the dichroic mirror, are placed at Brewster's angle, which minimizes the reflection losses for horizontal polarization. The SDL sample has been positioned for optimum performance for horizontal polarization (the SDL gain is nominally unpolarized; however, small effects due to slight birefringence in the clamped semiconductor/diamond composite can result in an optimal rotation angle). The Brewster elements therefore actively force the laser polarization to be horizontal by causing intolerable losses to any other polarization. The rest of the optical elements rely on the quality of the antireflection coatings to minimize the losses caused to the laser.

We have carried out several power transfer measurements and a Caird analysis [17], described already in Chapter 2, to evaluate the losses added by both auxiliary elements

Table 4.3: Mirror measured output coupling values and its inverse.

Nominal OC	Measured OC	1/OC
1 %	0.667 %	141.443
2 %	1.498 %	65.020
3 %	2.398 %	41.017

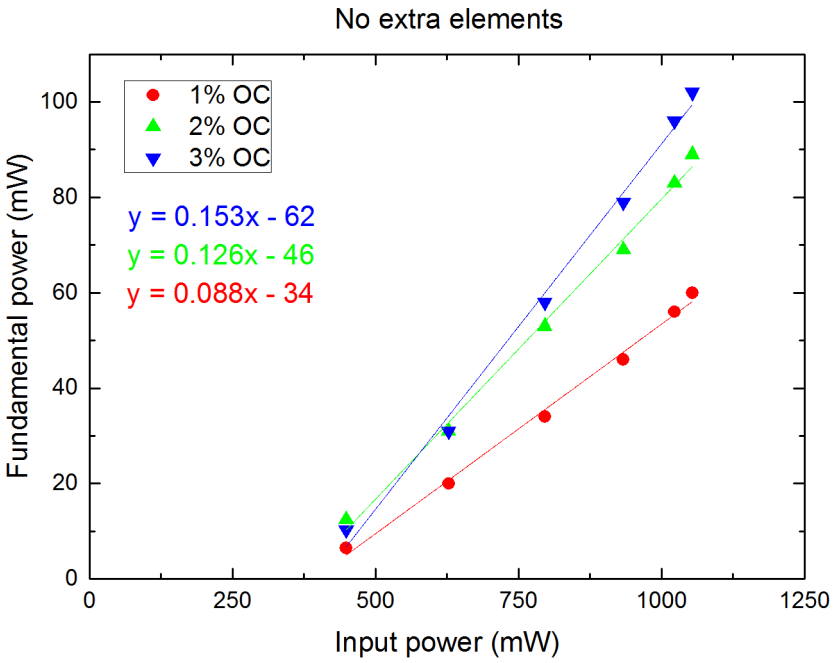

Figure 4.5: Power transfer for an empty 3 mirror cavity. This is the base cavity for the following measurements.

(dichroic mirror and dual waveplate), together with an analysis of the empty cavity (no extra elements) for comparison. Figures 4.5 to 4.7 show the effect of adding the dichroic mirror and the dual waveplate to a 3 mirror cavity, using the output couplers enumerated in table 4.3. The final OC value (or its inverse) takes into account a 0.04 % T folding mirror.

We can use these data to carry out the Caird analysis (figure 4.8), using the absorbed power slope efficiency and the output coupling of the cavity to find out the intrinsic slope efficiency and the round-trip cavity loss. The resulting data, summarized in table 4.4, show similar cavity losses in the empty cavity and when introducing the dichroic mirror.

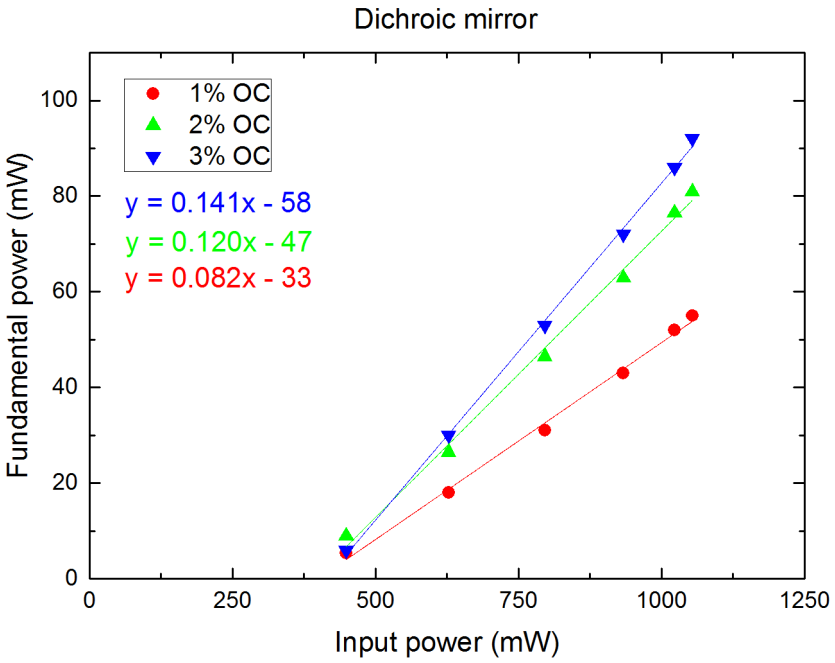

Figure 4.6: Power transfer for the 3 mirror cavity with the dichroic mirror placed inside.

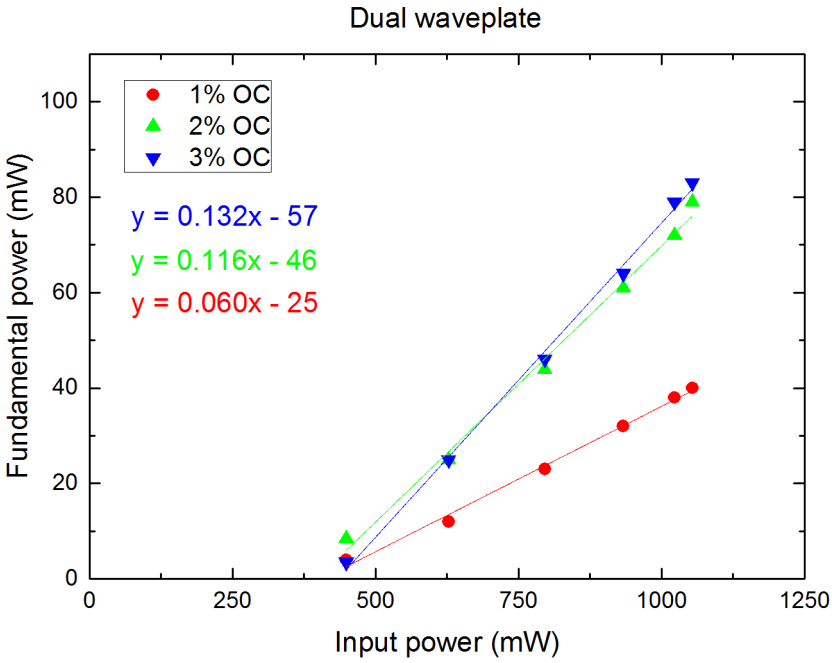

Figure 4.7: Power transfer for the 3 mirror cavity with the dual waveplate placed inside.

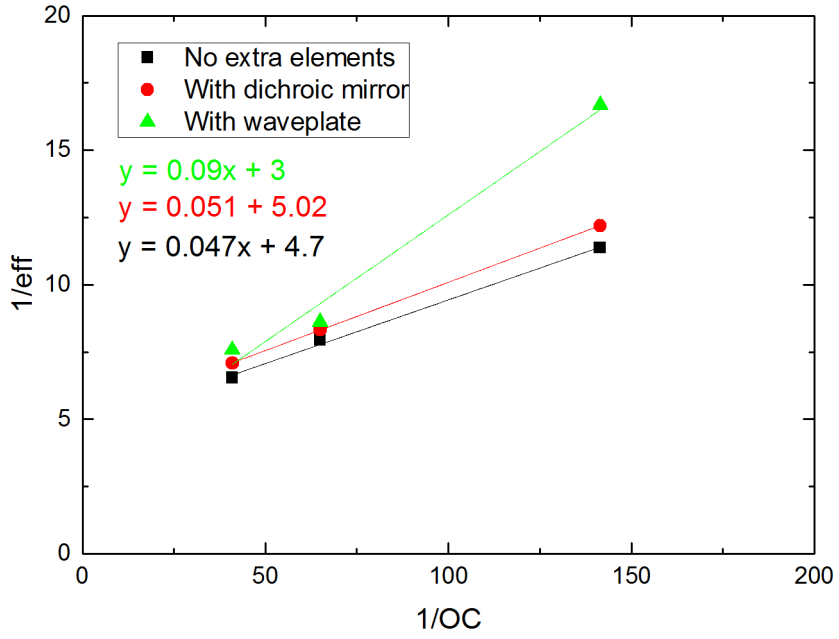

Figure 4.8: Caird plot: inverse of the slope efficiency (eff) as a function of the inverse of the output coupling (OC).

Table 4.4: Summary of data from figure 4.8 and calculation of the parasitic losses.

Setup	η_0	Loss
No extra elements	0.213	0.01
+ DM	0.199	0.01
+ DW	0.330	0.03

The dual waveplate, however, triples the losses. This will of course have an impact on the maximum intracavity power that we will be able to achieve, thus reducing the conversion efficiency of the nonlinear processes.

4.5 Experimental setup

The laser cavity will have some fixed features not dependent on its particular geometry, mostly described at the beginning of this chapter. We enumerate them here as a reminder and refer the reader to figure 4.9:

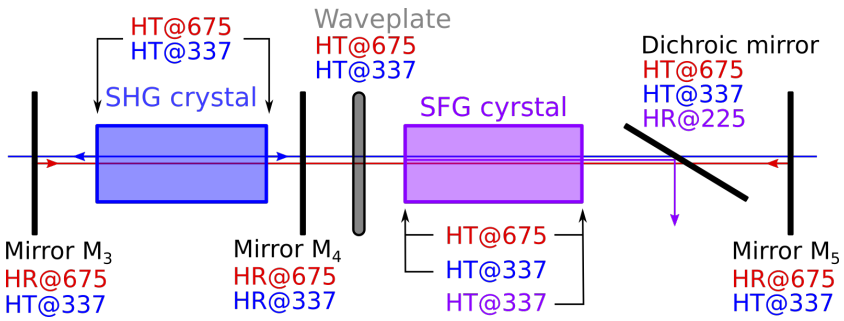

Figure 4.9: Intracavity tripling scheme: black lines correspond to mirrors. The mirror reflectivity and transmittance minimum requirements are explicitly described. The fundamental beam resonates inside the cavity, which produces SHG in both directions. Resonating the SHG beam is not trivial, and will be discussed in section 4.5.6. This drawing omits laser gain, in our system happening in the same cavity. For simplicity a 5-mirror cavity is considered here, refer to figure 4.14 for a full cavity drawing.

SHG is achieved inside a 7-mm long LBO crystal, producing a beam at 337 nm propagating forward, nearly collinear with the fundamental beam. The faces of this crystal are anti-reflection coated for fundamental and second harmonic. While all cavity mirrors are high reflective for the fundamental beam, mirrors between SHG crystal and SFG crystal need to reflect both fundamental and second harmonic beams, and therefore are also high reflective for SHG wavelength ($R > 99\,\%$).

Due to the resonance of the fundamental beam, SHG beam is produced in both forward and backwards directions. In the current set-up, the backwards propagating SHG is coupled out from the cavity via M_3, coated for high transmission at this wavelength.

As mentioned above, SHG occurs with type-I phase matching and, since SFG also utilises type-I phase matching, a dual waveplate is placed after the SHG crystal to rotate the polarization of the second harmonic beam parallel with that of the fundamental (90° rotation). It also acts as a full waveplate for the fundamental beam, leaving it unaffected. This element is highly transmissive for the fundamental and SHG beams.

SFG is achieved inside a 5-mm long BBO crystal, producing a beam at 224.5 nm propagating forward. The limitations of current coating technology mean that it is not feasible to coat the crystal for simultaneous antireflection at all three short wavelengths.

For this reason, the input face of the crystal is AR coated for the input beams, fundamental and second harmonic, but not for the third harmonic beam (it will not travel through this face, in principle). The output face of the crystal is AR coated for the fundamental and the third harmonic.

The third harmonic beam is extracted from the cavity using a dichroic mirror, positioned at Brewster's angle, antireflection coated for the second harmonic and highly reflective for the third harmonic ($R > 99.9\,\%$). Its placement at Brewster's angle ensures high transmission for the fundamental beam, removing the need for AR coating at this wavelength.

4.5.1 6-mirror cavity setup

The particular conditions required by this experiment to work, as described at the beginning of this chapter – together with the limitations in the available cavity designing software (WinLase), which makes finding a good cavity a 'trial and error' search – provided the motivation to look for a simple-to-find cavity design with 6 mirrors, so the beam geometry would alternate between focused and collimated in the different cavity arms. In parallel, a script was developed that would automatize the design of laser cavities in order to overcome the limitations of the previous cavity designing software.

The 6-mirror cavity, sketched in figure 4.10, provides two segments with a nearly collimated beam, in which we will position the BRF and the waveplate. SHG occurs between M_3 and M_4, with M_4 and M_5 being highly reflective for UVA. SFG occurs between M_5 and M_6. The last mirror is highly transmissive for UVA, since the second harmonic should not go back through the cavity to avoid unwanted conversion: since both fundamental and SHG beams would be traveling backwards through the SFG crystal, frequency conversion would take place producing a non-useful THG beam (considering that another dichroic mirror would be needed for extraction of this other beam), thus increasing losses for the fundamental and SHG. The beam size at the

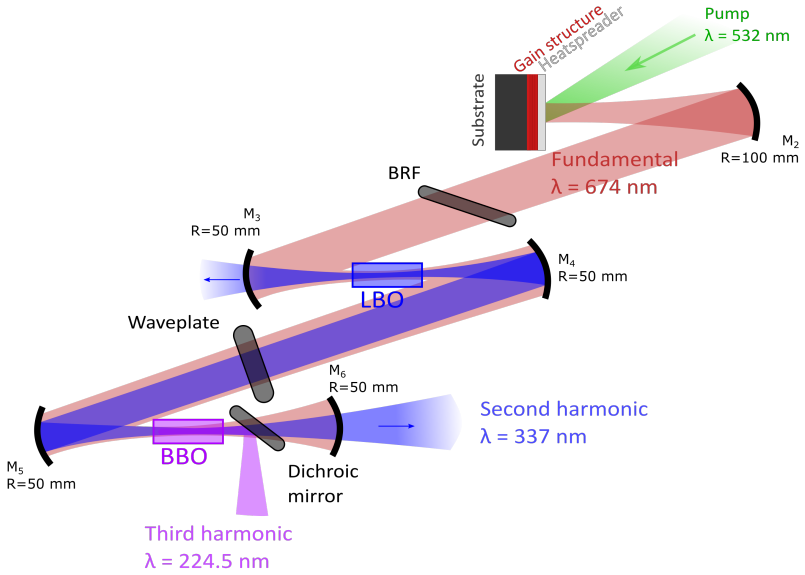

Figure 4.10: Schematic diagram of the 6M SDL frequency-tripling cavity. All abbreviations are defined in the main text.

gain structure is ∼40 µm radius, while in the nonlinear crystals is ∼15 µm and ∼40 µm respectively.

A solarization-resistant optical fiber, suitable for deep-UV operation, has been used together with an Avantes CCD spectrometer to measure the spectrum of the extracted beam.

4.5.2 6-mirror cavity results

Figure 4.11 shows the first measurement of the emission spectrum of the laser radiating in the deep UV, with the third harmonic centred at 224.5 nm. This is the shortest wavelength emitted from an SDL to date via the first implementation of intracavity frequency tripling in a visible SDL. It is also possible to observe the second harmonic peak at 337 nm, together with some noise produced by the fundamental beam (due to saturation of the CCD camera). This spectrum was measured using an Avantes CCD spectrometer with resolution of 0.4 nm.

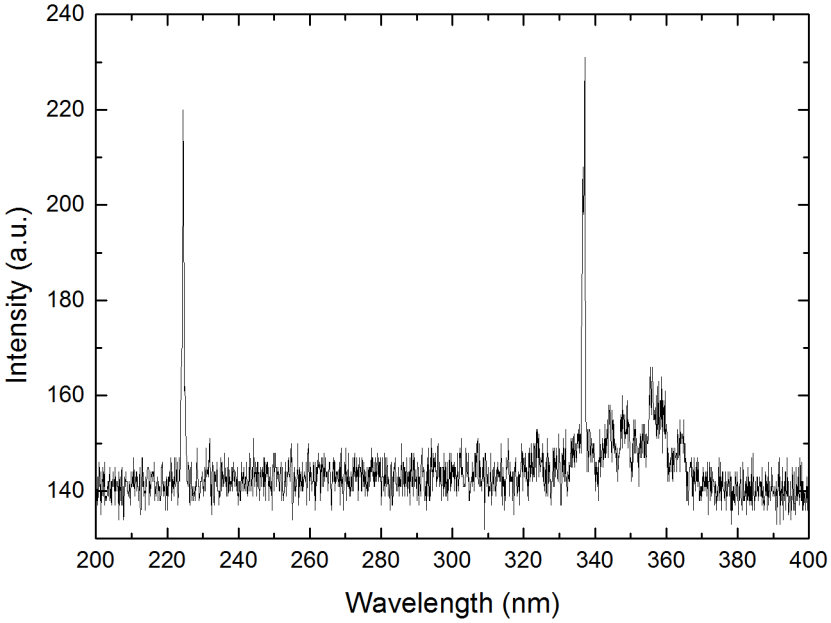

Figure 4.11: First spectrum showing generation of the third harmonic from a visible SDL.

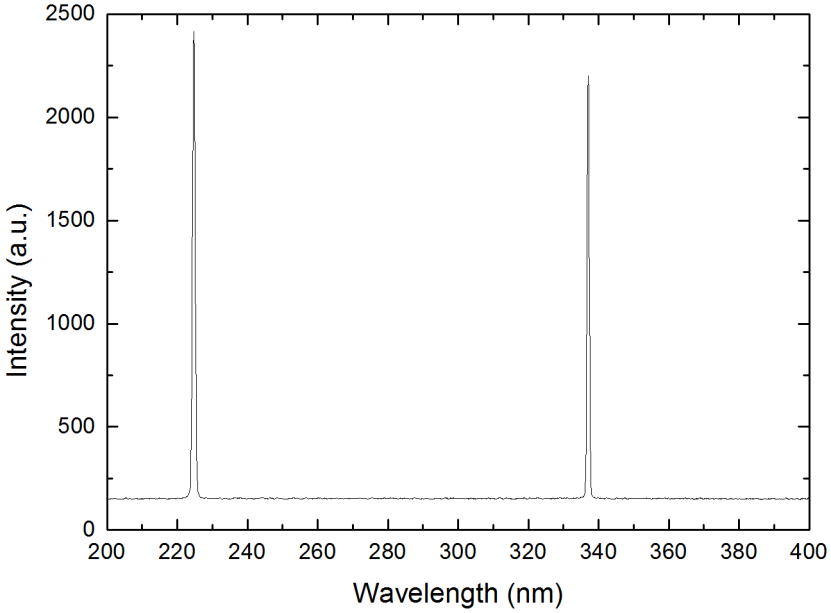

Figure 4.12: Spectrum showing generation of the third harmonic from a visible SDL. The noise has been reduced by careful isolation of the THG beam.

It is difficult to measure the third harmonic power due to the low efficiency of the process. Even extracting it with a dichroic mirror, the fundamental beam reflected

here (a very small percentage of the intracavity power) is still much larger than the THG power. Using a pinhole, together with a set of dichroic mirrors filtering out the fundamental and careful optimization of the system, we were able to greatly reduce the fundamental light overlapping the third harmonic and increase the signal to noise ratio, allowing for a cleaner spectrum (figure 4.12). The linewidth of the third harmonic peak is ∼1 nm.

The wavelength can be tuned between 224.0 nm and 225.8 nm, as shown in figure 4.13, by rotating the BRF and adjusting the phase matching angle of both crystals to the new optimum position. The realignment of the crystals to match the BRF wavelength is complicated and usually causing the output power to be greatly reduced when moving away from the maximum. The dual waveplate also contributes to the diminishing of the power since it is designed to work at a fundamental wavelength of 674 nm, which yields a third harmonic wavelength of 224.5 nm. We can see that the tuning range is centred on this particular wavelength. As will be shown in section 4.5.4, in the 5-mirror cavity the tuning range is still centred on 224.5 nm, but is slightly broader.

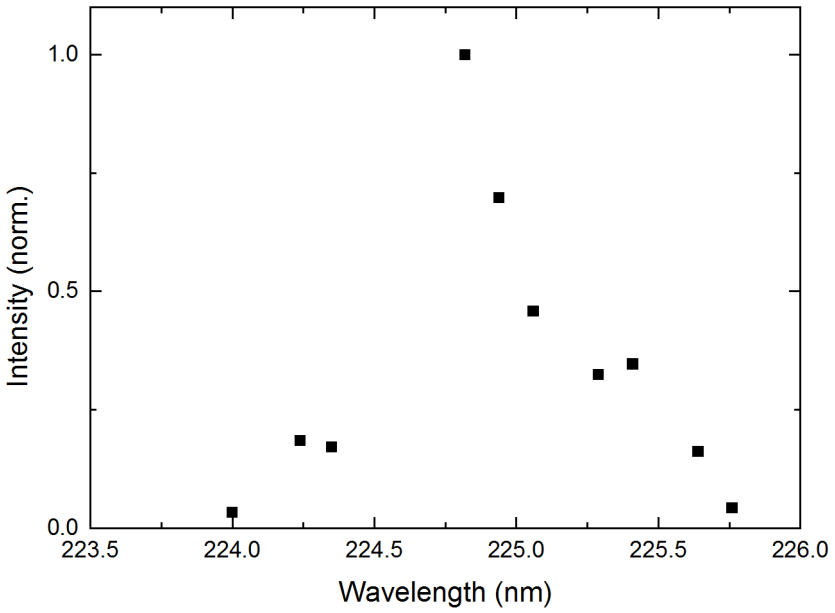

Figure 4.13: Normalised UVC output power of the laser as the wavelength is tuned by rotation of the birefringent filter. The tuning range is 350 cm^{-1}. Power quickly drops away from the central wavelength.

4.5.3 5-mirror cavity setup

At this point, our script for automatizing the cavity search was ready and we were able to find stable solutions for a 5-mirror configuration with close-to-desired beam sizes. Further development has led to a ready to use program called SimCav, described in Appendix A.

The new laser setup consists of a 5-mirror cavity designed with 3 beam waists: at the SDL (43 µm radius), LBO crystal (∼15 µm radius) and at the BBO crystal (∼40 µm radius) respectively. Tight waists have been chosen to ensure high power densities and thus favour higher conversion efficiencies. All mirrors have high reflectivity at the fundamental wavelength ($R > 99.9\,\%$). Mirror M_4 is again HR coated for the second harmonic. M_5 is this time HT for this wavelength, as is M_3.

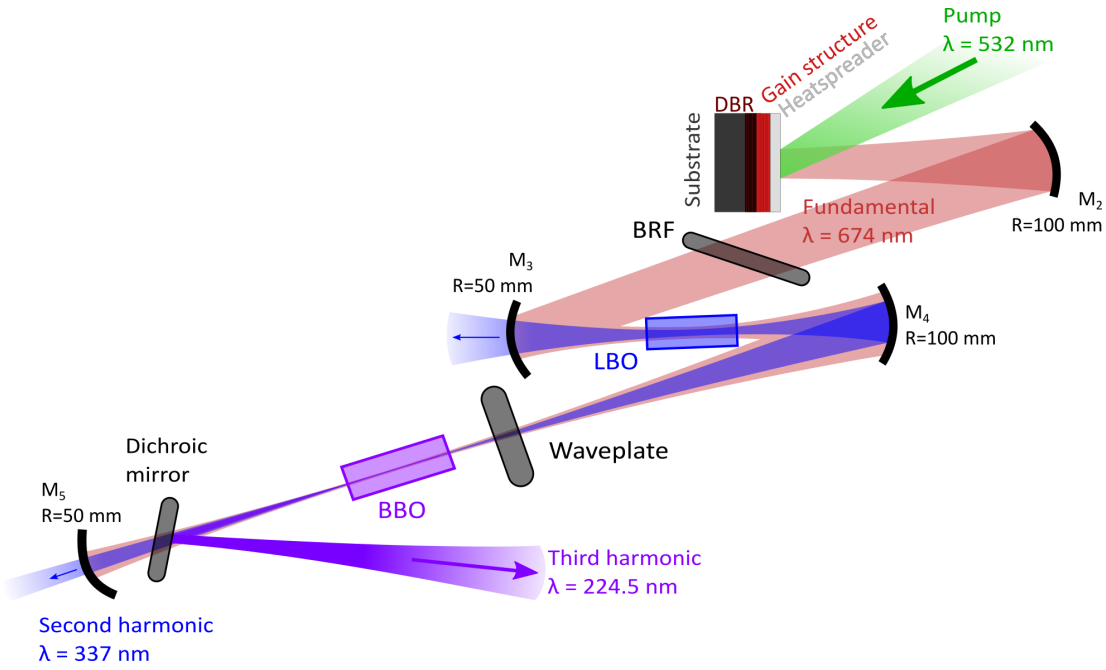

Figure 4.14: Schematic diagram of the 5M SDL frequency-tripling cavity (SFG setup). All abbreviations are defined in the main text.

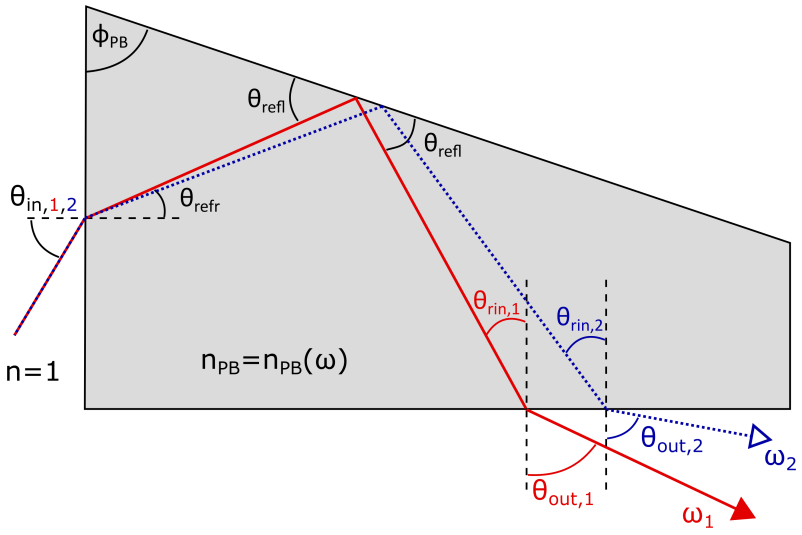

Figure 4.15: Pellin Broca prism effect in two coaxial beams incident at Brewster's angle. At the exit of the prism both beams are spatially separated and travelling with a different angle.

Pellin Broca prism

We overcame the previous issue of overlapping fundamental and UV output beams using a Pellin Broca prism to separate the beams reflected by the dichroic mirror. The difference in the angle of deviation is enough to achieve centimetre-separation between the beams. Separating the beams also allows for observation of the THG beam, by means of using a fluorescent card, thus easing the alignment of optical elements. As can be seen in figure 4.15, a beam travelling through the prism will undergo refraction and reflection until it exits with a 90° angle from the initial direction. Different wavelengths will present different refraction angles, thus modifying the final direction.

The drawbacks of this method are two-fold:

- The material of the prism is fused silica, which presents some (little) absorption at 225 nm.

- It is designed to work at Brewster's angle (so the output direction is perpendicular to the input direction).

Regarding the material, fused silica absorbs in the UVC band, so the prism has a transmittance of 98.8 % for 10 mm at 224 nm (excluding Fresnel loss), with an absorption coefficient of $\alpha_0 = 0.011\,65\,\mathrm{cm}^{-1}$. The distance the light travels inside the prism has been estimated as 38.6 mm, and so the transmittance of the prism for our beam will be approximately 95.6 %.

However this takes us to the second drawback: the prism is designed to be positioned at Brewster's angle for horizontal polarization, while the polarization of our THG beam is vertical. The Brewster's angle is 56.66°. Since the prism facets are not antireflection coated, according to Fresnel equations this causes 15.8 % reflection loss for the input THG beam. Considering the angle evolution as depicted in figure 4.15, the angle of incidence when exiting the prism is 34.14°, and this causes an extra 17.5 % reflection loss.

The final transmission will therefore be $T_{\mathrm{prism}} = (1 - R_{Si})T_P(1 - R_{So}) = 0.66$. We are also using a lens of the same material to keep the laser focused, which has a calculated transmission of $T_{\mathrm{lens}} = 0.91$. The total transmittance of the imaging system is then $T_{\mathrm{system}} = T_{\mathrm{lens}} \cdot T_{\mathrm{prism}} = 0.60$, or 60 % of the produced THG.

4.5.4 5-mirror cavity results

This cavity has proven to be more reliable than the previous one given the larger stability range that permits better mirror positioning and alignment, also improving the beam quality (TEM_{00} is desired for optimal conversion efficiency in the nonlinear processes). This helps to achieve higher intracavity power, thus improving all the nonlinear processes and obtaining higher output powers.

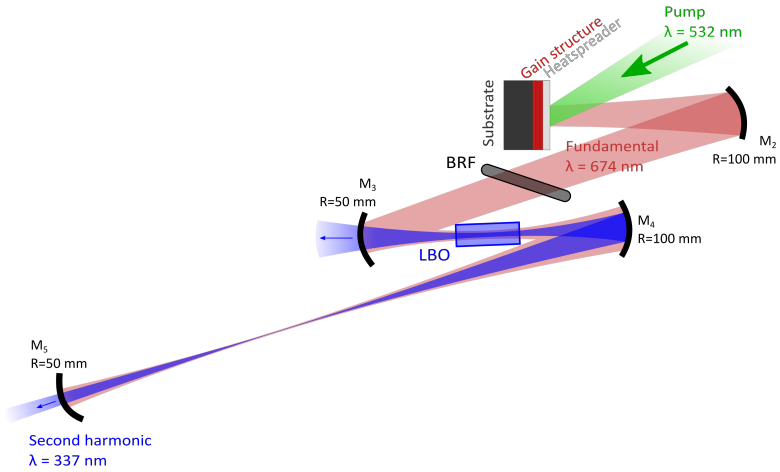

Figure 4.16: Schematic diagram of the 5M cavity set for SHG operation (SHG setup).

SHG setup

The SHG performance must be fully optimized before moving to the next step. Good conversion efficiency for this process ensures higher input power available for conversion in the SFG process. While the cavity will be modified with the inclusion of the second nonlinear crystal (also, to a lesser extent, by the dual waveplate and dichroic mirror) this modification affects mostly the positioning of M_5 and beam size in the last arm of the cavity, leaving the SHG segment unaffected (figure 4.16).

Thanks to the optimized design of the cavity and precise alignment of the cavity elements, we have managed to obtain a total SHG output power over 120 mW and 0.2 % conversion efficiency from intracavity power. This result has been obtained with LBO, whose nonlinear coefficient is 4 times smaller than that of BBO at these wavelengths, for which the maximum conversion efficiency previously reported is under 0.6 % for a similar configuration [18]. As can be observed in figure 4.17a, the intracavity power reaches over 60 W. While not as high as that achieved in the 3-mirror cavity with fundamental-only operation, it is still a high fundamental power that allows for a high SHG output power. Since the performance of the SDL with nonlinear output coupling

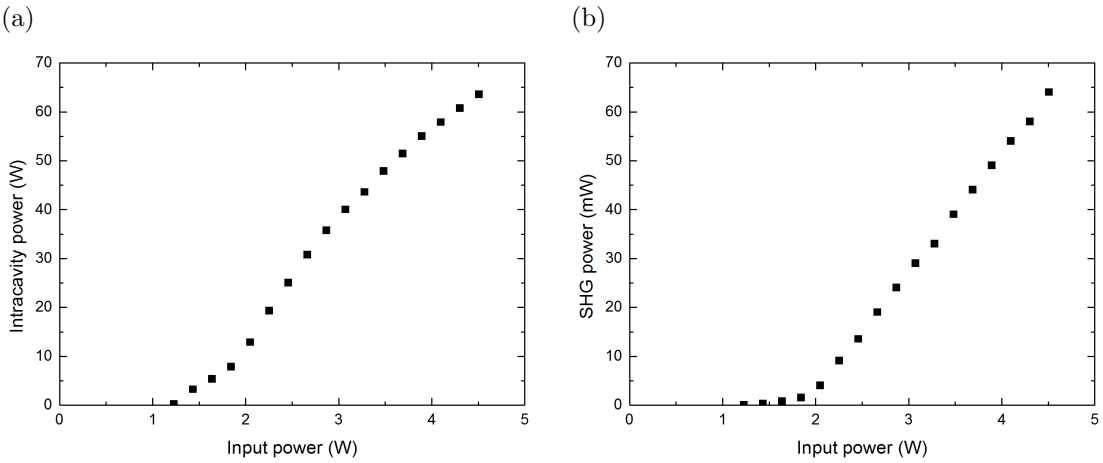

Figure 4.17: Intracavity power (a) and SHG power (b) as a function of the input power. The SHG power measured is in a single beam, representing half the total SHG produced.

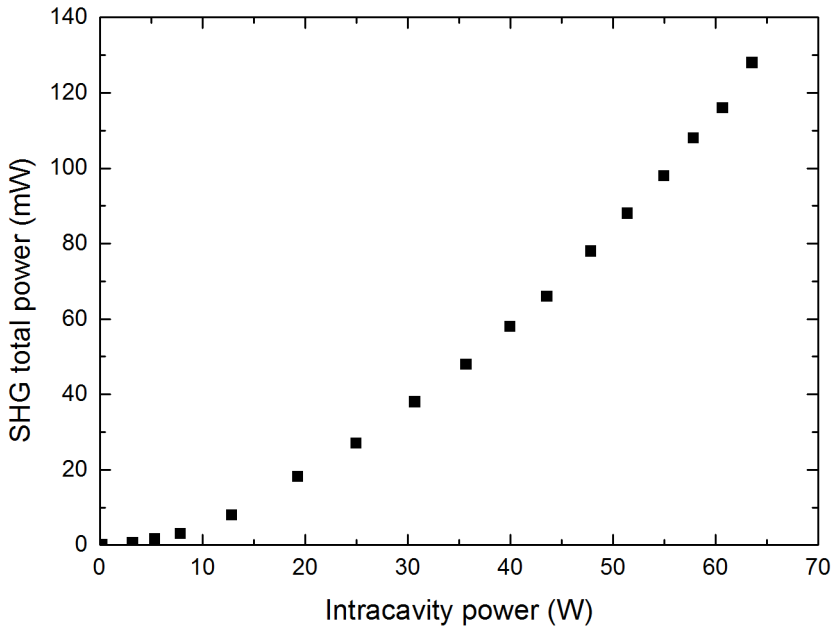

Figure 4.18: SHG power versus fundamental intracavity power, showing the expected quadratic behaviour.

does not follow a linear increase with pump power, the SHG power with respect to this same pump power does not follow a quadratic evolution. Plotting the SHG output power as a function of the intracavity power shows the expected quadratic behaviour, in accordance with the theory (figure 4.18).

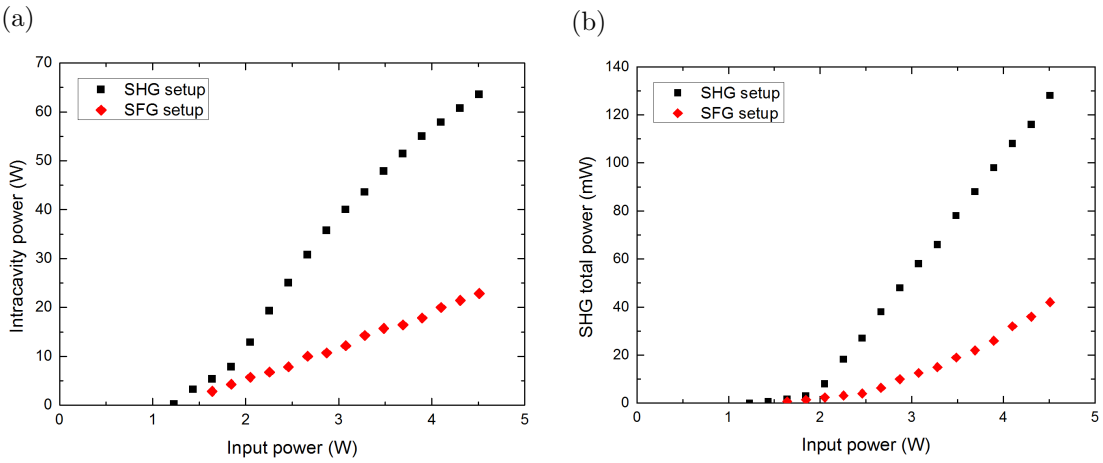

Figure 4.19: Intracavity power (a) and SHG power (b) as a function of the input power. The SHG power is single beam, meaning half the total SHG power. The two different curves correspond to the SHG setup (analysed in the previous section, shown for comparison) and SFG setup of the cavity, as described in the text.

SFG setup

Once the dual waveplate, the SFG crystal and the dichroic mirror are inserted, we can see in figure 4.19a how the intracavity power has now decreased by 60 %. Note that in this particular case the SFG crystal is purposely aligned for no phase matching so no frequency mixing process takes place, thus avoiding any possible depletion. The new SHG output power has also decreased to 60 % figure 4.19b of the previous value, which is not as much as expected given the quadratic dependence of the SHG with the fundamental intracavity power.

As we can see from figure 4.20, the conversion efficiency from intracavity power to SHG power is slightly increased, perhaps indicating better alignment of the crystal in terms of phase matching and/or positioning at the waist. Note that the inclusion of the new intracavity elements modified the geometry of the cavity, thus changing the beam sizes.

Unfortunately, and as clearly shown in figures 4.19a and 4.19b and figure 4.20, the dramatic drop of the intracavity power greatly reduces the overall (pump to SHG)

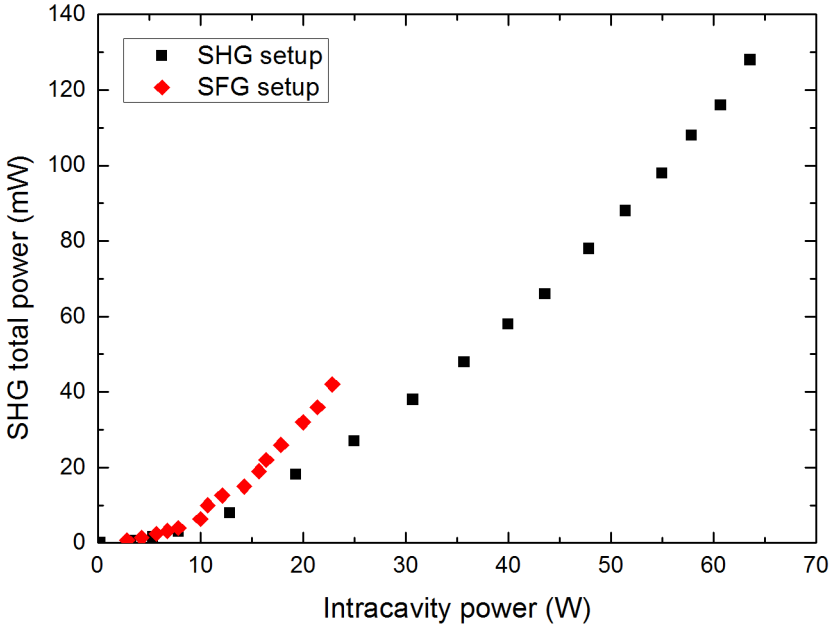

Figure 4.20: SHG total power as a function of the intracavity power for the SHG and SFG setups. Although the intracavity power is reduced in the SFG setup, the SHG conversion efficiency has been further improved.

efficiency of the SHG process, which has changed from almost 3 % to close to 1 %, as shown in figure 4.21. The reduced intracavity and SHG power available will have a negative impact in the conversion efficiency of the following SFG process, whose output power is directly proportional to the power of the input beams.

In conclusion, even if there is not much we can do to deal with the losses caused by all the intracavity elements required, it is important that we carefully design and align the cavity to maximize its potential. This will help to maintain an optimal conversion efficiency and therefore increase the fundamental and SHG power available for sum-frequency mixing.

We now move on to the next step, and align the SFG crystal at the correct phase matching angle so the sum-frequency generation process takes place.

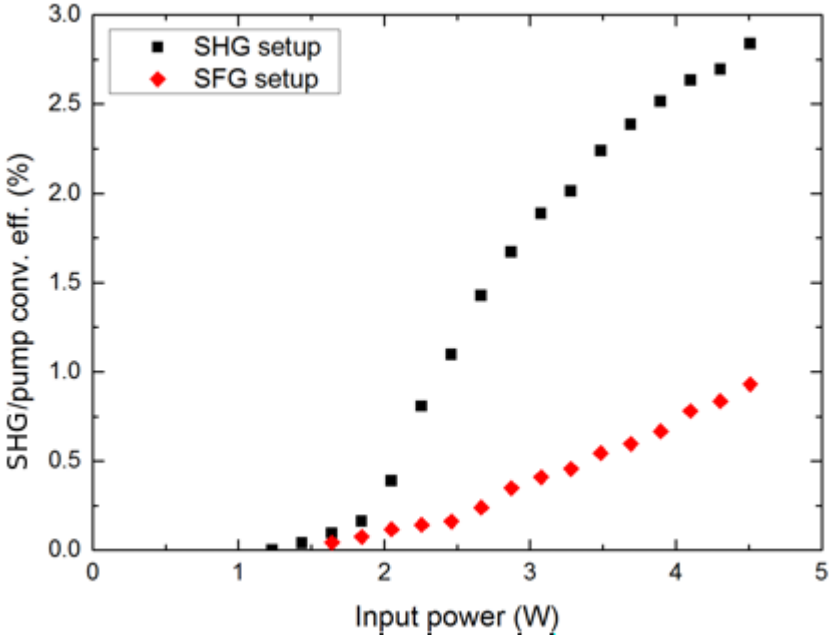

Figure 4.21: Input power to SHG power conversion efficiency. The decrease of this efficiency is caused by the decrease of the intracavity power.

Results

The new spectrum of the laser output shows that this time the third harmonic is the only beam coupled into the fibre (figure 4.22), thanks to the separation introduced by the Pellin Broca prism. The linewidth of the third harmonic beam is again ∼1 nm. Also, this separation of the THG beam from the fundamental or unwanted SHG reflections makes it easier to recognize when SFG is actually taking place, by means of using a fluorescent card that allows direct eye detection over a threshold. The new cavity provided enough THG output power for this threshold to be easily reached. This allowed for better alignment of optical elements. The output beam was carefully isolated from other light sources, such as the fundamental beam reflections or the pump scattered light (very bright in comparison).

The THG power was now high enough to be measured with an optical power meter, and we were able to produce a power transfer curve. In figure 4.23 we have plotted the THG output power vs the input power. As can be seen in equation (5.12) the THG

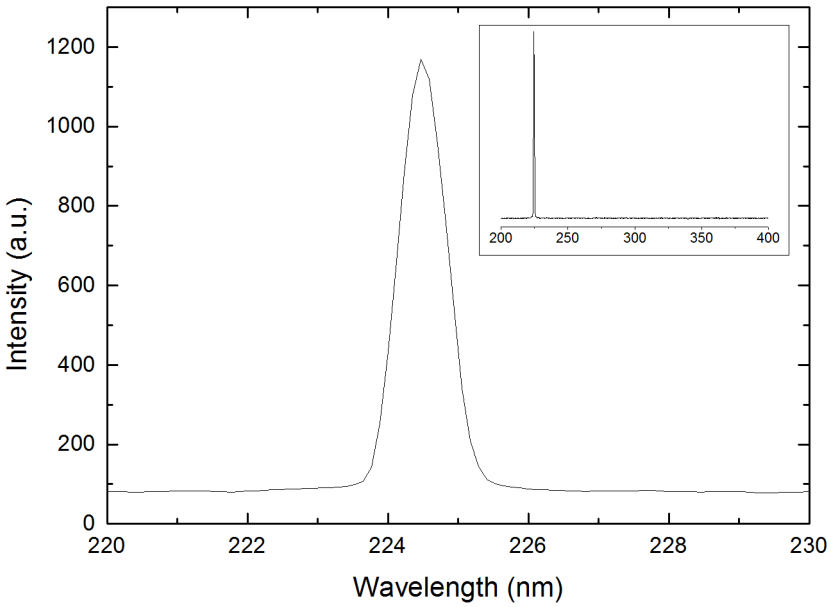

Figure 4.22: THG output spectrum, with linewidth of ∼1 nm. SHG signal is no longer present due to the use of the Pellin Broca prism (see inset). The resolution of the spectrometer is 0.4 nm.

power is proportional to the power of the fundamental and the power of the second harmonic. Since the SHG power is proportional to the square of the fundamental power, the THG should be proportional to the cube of the fundamental intracavity power. This intracavity power is usually proportional to the input power, so the dependence of the THG power with the input power should be cubic as well. This is no longer true when the intracavity power deviates from linear behaviour, as, for example, that caused by thermal roll over.

78 µW of THG output power were produced with 4.5 W of input power, as shown in figure 4.23. The intracavity power for maximum input is estimated to be under 30 W. The SHG power is estimated to be between 20 and 30 mW per beam, although only the forward propagating beam is contributing to the SFG process in the current configuration. The laser threshold (for the fundamental wavelength) is at 1.1 W of input power. However the THG is not detectable below 1.6 W of input power. The SHG to THG efficiency is calculated to be 0.5 %. This conversion efficiency is limited mainly

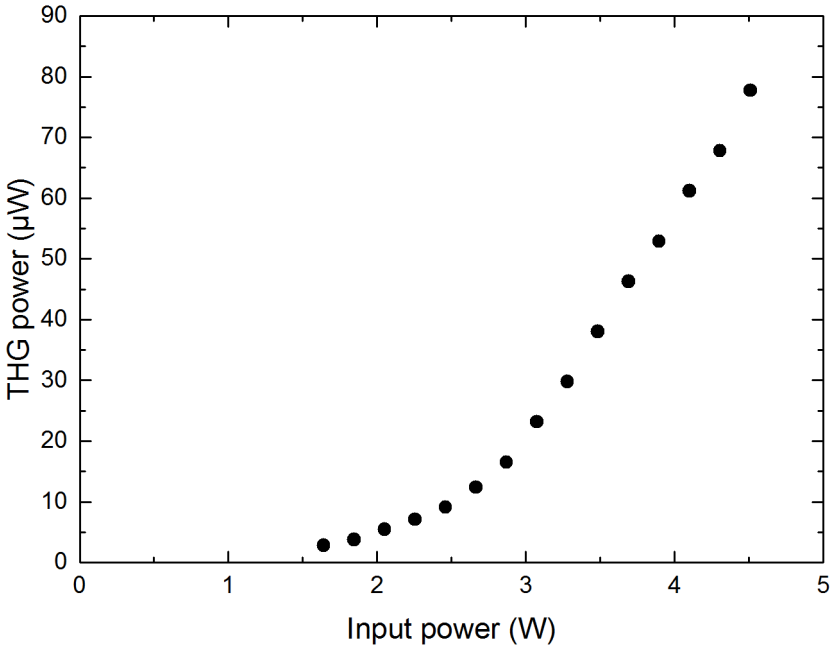

Figure 4.23: THG output power as a function of the input power. Almost 80 µW of power is obtained at 224.5 nm.

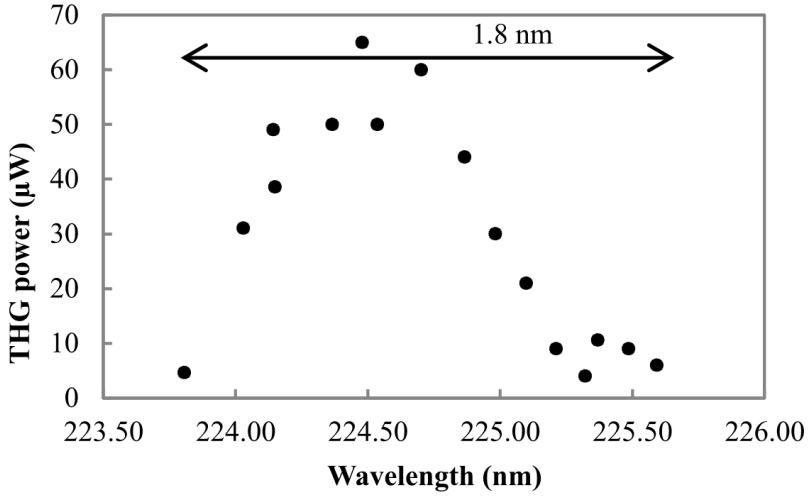

Figure 4.24: Normalised UVC output power of the laser as the wavelength is tuned by rotation of the birefringent filter. The tuning range is 350 cm^{-1}. Contrary to the 6-mirror cavity tuning curve, the power is much more stable around the central peak.

by the divergence of the beams and by the walk-off induced by the nonlinear materials, and will be studied in detail in Chapter 5.

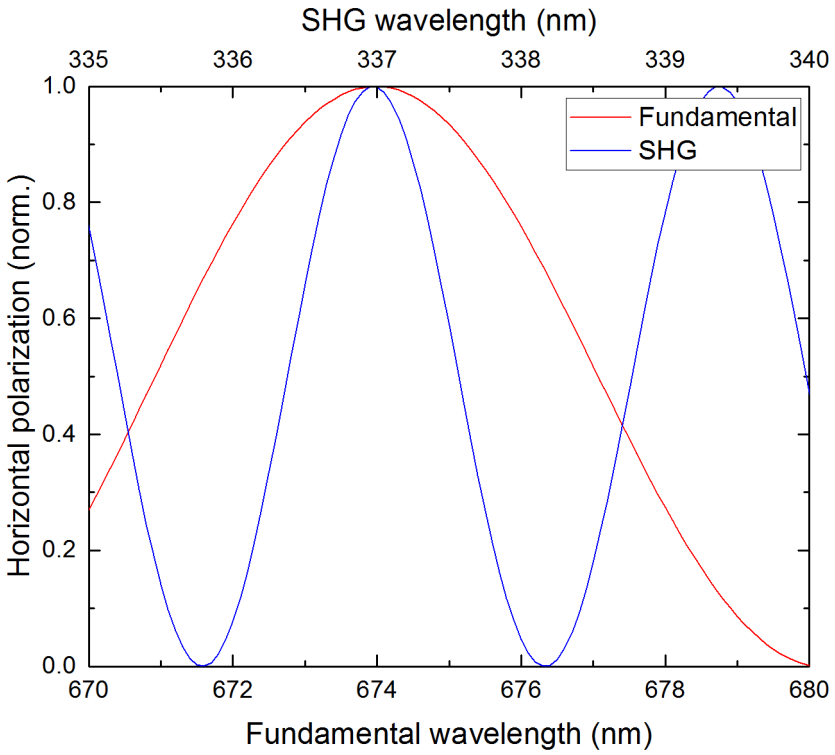

Figure 4.25: Change in polarization of fundamental (red) and SHG (blue) beams when the dual waveplate is rotated out of the central position.

As in the 6-mirror cavity, we can tune the output wavelength of this laser by rotating the BRF and reorienting both nonlinear crystals for good phase matching alignment. The tuning range in this case is 223.8 nm to 225.6 nm (figure 4.24), corresponding to a fundamental wavelength range of 5.4 nm. This particular SDL is capable of a tuning range of 10 nm without nonlinear conversion. Nevertheless, 1.8 nm tuning in the UVC corresponds to a tuning range of 350 cm^{-1}, comparable with typical tuning ranges of SDLs at other wavelengths [18–22].

The dual waveplate is designed to work at 674 nm / 337 nm, and its performance is reduced when the wavelength is tuned away from these values (as can be seen in figure 4.25). While it works within a region around the central wavelength, the polarization mismatch caused seems to be limiting the tuning of the laser. A tunable dual waveplate, e.g. featuring variable thickness, should allow for an extended tuning range, potentially over 3 nm (around 600 cm^{-1}).

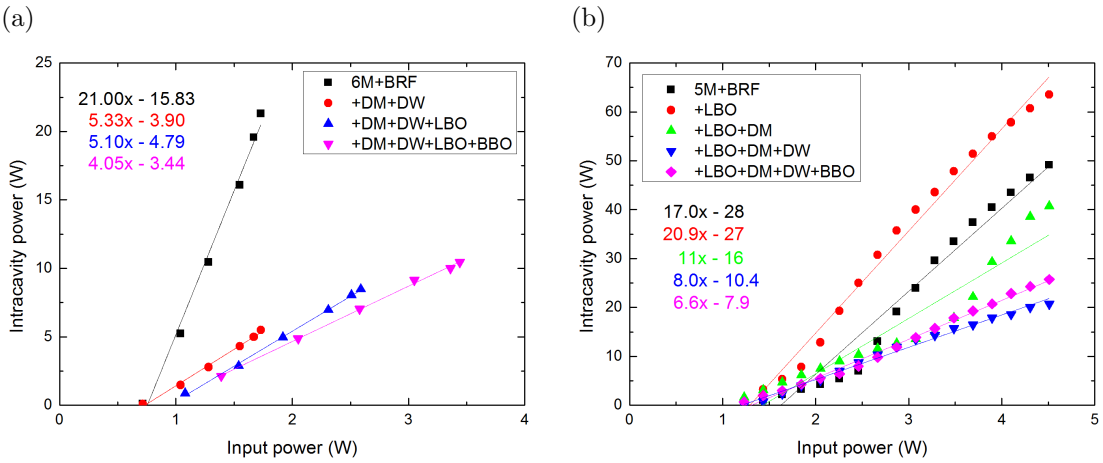

Figure 4.26: Power transfers on the 6M cavity (a) and 5M cavity (b) showing the effect the addition of intracavity elements has on the intracavity power. Blue and pink curves depict the same intracavity elements in both graphs.

4.5.5 Comparison of 5- and 6-mirror cavity set-ups

Figures 4.26a and 4.26b show the intracavity powers achieved in the 6 mirror cavity and the 5 mirror cavity with the inclusion of the intracavity elements. In both cases, this addition produces a dramatic loss of intracavity power. We should note that the pump power used for the 6 mirror cavity was not yet as high as it could be, since this was the first time using such amount of power on the sample. The optimization of the cavity is therefore different from optimization at high power, obtaining lower threshold powers. From the evolution of the slopes of the linear curves we can appreciate the effect of the added losses to the cavities. As seen from the most relevant blue and pink data, the slopes are similar, suggesting that the conversion efficiency should be similar in both cases (for equal pump power). If this was the case we should have been able to measure THG power over 20 µW in the 6 mirror cavity. We suspect that this difference may be caused by the way the beams overlap within the crystal, discussed in detail in Chapter 5.

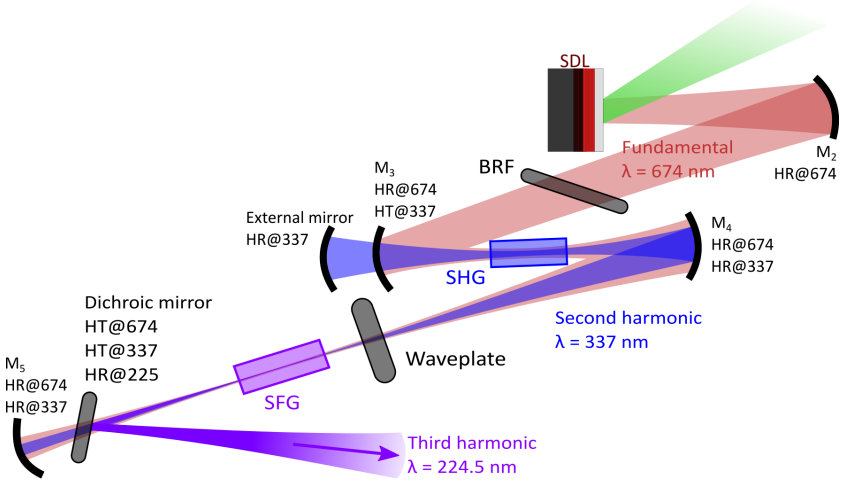

Figure 4.27: 5-mirror cavity with an added external mirror after M_3, reflecting back into the cavity the previously lost SHG backwards beam.

4.5.6 Further improvements

All the aforementioned experiments make use of the forward-propagating SHG beam to produce frequency conversion but, since the SHG process is produced in a resonant cavity, a second, backwards-propagating SHG beam is also generated. In the previous experiments, said backwards-propagating beam is not used, effectively meaning a loss of 50 % of the available SHG power. New mounts for the optical elements will allow the use of an external mirror (positioned behind M_3, as shown in figure 4.27) to reflect this previously wasted SHG beam back into the cavity, with mirror steering for optimum adjust. With this simple setup we can easily block the external mirror to revert to the original system, and unblock it to retroreflect the secondary SHG beam. The effect of this new configuration, reflecting back the second SHG beam, can be seen in figure 4.28.

Unfortunately, the 5mm-long BBO crystal had undergone degradation before the implementation of this experiment. We note that the intracavity power is nearly half that of the previous results. The conversion efficiency has also dropped, since this laser previously achieved roughly eight times more output power for such a level of intracavity power. Nevertheless, we can observe how the THG power achievable with

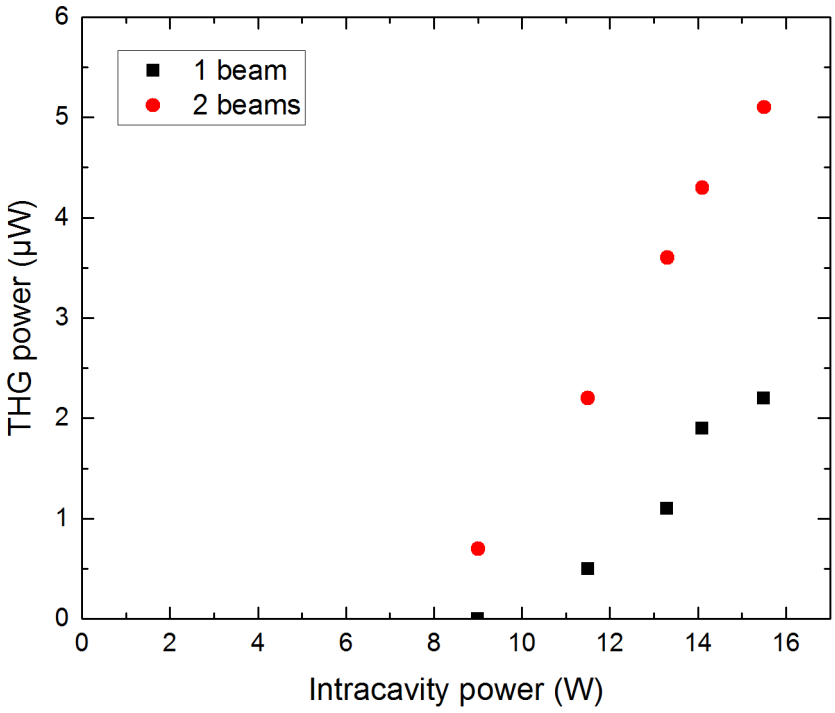

Figure 4.28: THG output power as a function of the intracavity power comparing the system with (red circles) and without (black squares) an external SHG reflecting mirror. Use of both SHG beams doubles the achievable THG power.

the retroreflection setup (with the external mirror sending back the other SHG beam that was previously lost) is twice the power obtained with the single beam setup. Due to the degradation in the BBO crystal we cannot compare this result with that reported in section 4.5.4, but the available data is promising.

Previous systems [16] have reversed the order of the crystals in the cavity, producing SHG near the last mirror of the cavity and directly reflecting it (together with the fundamental). While this is the ideal method (see figure 4.29), it is difficult to implement when large values of the walk-off angle are present. The second SHG beam suffers deviation from the optical axis twice, as it passes back and forth through the SHG crystal, and the reflecting mirror, being part of the cavity resonant for the fundamental, cannot independently compensate for this. Having the SHG reflecting mirror separated

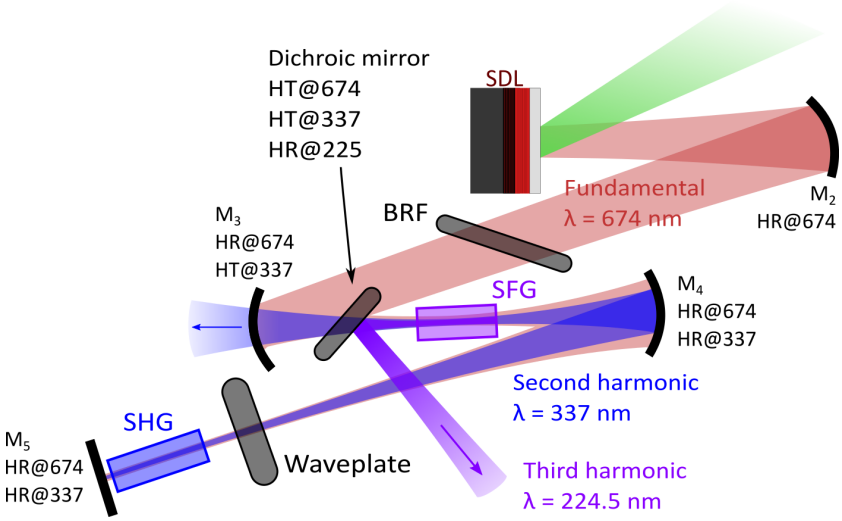

Figure 4.29: Tripling cavity in reversed order. The location of the SHG crystal at the end of the cavity allows for easy reflection of the forward propagating SHG beam, so the total SHG is directed into the SFG crystal. Since M_5 is part of the cavity, correction on the SHG beam alone is not possible, thus presenting an issue if large walk-off values are present on the second harmonic stage.

from the cavity allows for beam steering, compensating the walk-off drift and optimizing the path for improved mixing.

4.6 Conclusion

This result is, to the authors' knowledge, the shortest wavelength ever achieved with an SDL, and the first implementation of intracavity tripling from a visible SDL. The system offers continuous wave laser operation in the deep UV region of the electromagnetic spectrum, with an output power of 78 µW at 224.5 nm and tunable over a range of 350 cm^{-1}. The setup is compact, as compared with other systems offering CW, UVC laser emission (e.g. [23, 24]), thanks to the short fundamental wavelength and the intracavity scheme used for frequency conversion.

AlGaInP-based (red) SDLs are a relatively immature laser technology, with efficiency improvements still regularly reported (see e.g. 2.5 W output power reported by Mateo *et*

al. [25]), meaning a significant increase of the fundamental power is potentially available with an associated increase in frequency conversion efficiency. Given the cubic dependence of the third harmonic output power on the fundamental intracavity power, deep UV on the order of several milli-Watts is feasible. In addition, semiconductor bandgap engineering has shown that AlGaInP-based SDLs can offer fundamental emission over a 50 nm range around 665 nm, thus offering access to the 213 – 230 nm range with similar set-ups.

Chapter 5 describes an investigation of the power limitations of the current set-up, presenting a study of the evolution of the beams inside the cavity and their overlap within the SFG crystal, and using the available nonlinear frequency conversion theory to calculate the expected performance of this system.

References

[1] R. H. Kingston. "Parametric Amplification and Oscillation at Optical Frequencies". In: *Proceedings of the IRE* 50.4 (1962), p. 472. DOI: 10.1109/JRPROC.1962.288044.

[2] S. A. Akhmanov, A. . Kovrigin, A. S. Piskarskas, V. V. Fadeev, and R. V. Khokhlov. "Observation of parametric amplification in the optical range". In: *JETP Letters* 2 (1965), pp. 191–193.

[3] A. G. Akhmanov, S. A. Akmanov, B. V. Zhdanov, A. I. Kovrigin, N. K. Podsotskaya, and R. V. Khokhlov. "Generation of coherent radiation at $\lambda = 2120$ Å by cascade frequency conversion". In: *Journal of Experimental and Theoretical Physics Letters* 10 (1969), p. 254.

[4] S. E. Harris and R. B. Miles. "Proposed third-harmonic generation in phase-matched metal vapors". In: *Applied Physics Letters* 19.10 (1971), pp. 385–387. DOI: 10.1063/1.1653740.

[5] J. F. Young, G. C. Bjorklund, A. H. Kung, R. B. Miles, and S. E. Harris. "Third-Harmonic Generation in Phase-Matched Rb Vapor". In: *Physical Review Letters* 27.23 (Dec. 1971), pp. 1551–1553. DOI: 10.1103/PhysRevLett.27.1551.

[6] K. V. A. Norinskii L. V. "Effective Generation of Powerful Coherent Ultraviolet Radiation". In: *JETP Letters* 13.4 (1971), p. 133.

[7] D. T. Attwood, E. L. Pierce, and L. W. Coleman. "Conversion efficiency and pulse shortening of a frequency-tripled, sub-nanosecond, 1.064 μm pulse". In: *Optics Communications* 15.1 (1975), pp. 10–12. DOI: 10.1016/0030-4018(75)90170-4.

[8] R. S. Craxton. "Theory of high efficiency third harmonic generation of high power Nd-glass laser radiation". In: *Optics Communications* 34.3 (Sept. 1980), pp. 474–478. DOI: 10.1016/0030-4018(80)90420-4.

[9] R. S. Craxton. "High efficiency freqeuncy tripling schemes for high-power Nd:Glass lasers". In: *IEEE Journal of Quantum Electronics* 9 (1981), pp. 1771–1782. DOI: 10.1109/jqe.1981.1071318.

[10] W. Seka, S. D. Jacobs, J. E. Rizzo, R. Boni, and R. S. Craxton. "Demonstration of high efficiency third harmonic conversion of high power Nd-glass laser radiation". In: *Optics Communications* 34.3 (Sept. 1980), pp. 469–473. DOI: 10.1016/0030-4018(80)90419-8.

[11] R. Wu. "High-efficiency and compact blue source: intracavity frequency tripling by using LBO and BBO without the influence of birefringence". In: *Applied Optics* 32.6 (Feb. 1993), p. 971. DOI: 10.1364/AO.32.000971.

[12] K. Koch and G. T. Moore. "Singly resonant cavity-enhanced frequency tripling". In: *Journal of the Optical Society of America B* 16.3 (Mar. 1999), p. 448. DOI: 10.1364/JOSAB.16.000448.

[13] E. Roissé, V. Couderc, A. Barthélémy, and F. Louradour. "Intracavity frequency-tripling of actively mode-locked diode-pumped Nd:YAG laser". In: *Applied Physics B: Lasers and Optics* 69.2 (Aug. 1999), pp. 89–91. DOI: 10.1007/s003400050776.

[14] G. McConnell, A. I. Ferguson, and N. Langford. "Cavity-augmented frequency tripling of a continuous wave mode-locked laser". In: *Journal of Physics D: Applied Physics* 34.16 (Aug. 2001), pp. 2408–2413. DOI: 10.1088/0022-3727/34/16/304.

[15] Z. Sun, R. Li, Y. Bi, X. Yang, Y. Bo, W. Hou, X. Lin, H. Zhang, D. Cui, and Z. Xu. "Generation of 4.3-W coherent blue light by frequency-tripling of a side-pumped Nd:YAG laser in LBO crystals". In: *Optics Express* 12.26 (2004), p. 6428. DOI: 10.1364/OPEX.12.006428.

[16] Q.-z. Shu, A. L. Caprara, J. D. Berger, D. W. Anthon, H. Jerman, and L. Spinelli. "Intracavity-tripled optically-pumped semiconductor laser at 355 nm". In: *Lasers and Applications in Science and Engineering*. Ed. by W. A. Clarkson,

N. Hodgson, and R. K. Shori. Vol. 7193. San Jose: SPIE, Feb. 2009, p. 719319. DOI: 10.1117/12.816073.

[17] J. A. Caird, S. A. Payne, P. R. Staber, A. J. Ramponi, L. L. Chase, and W. F. Krupke. "Quantum electronic properties of the $Na_3Ga_2Li_3F_{12}$:Cr^{3+} laser". In: *IEEE Journal of Quantum Electronics* 24.6 (June 1988), pp. 1077–1099. DOI: 10.1109/3.231.

[18] H. Kahle, R. Bek, M. Heldmaier, T. Schwarzbäck, M. Jetter, and P. Michler. "High optical output power in the UVA range of a frequency-doubled, strain-compensated AlGaInP-VECSEL". In: *Applied Physics Express* 7.9 (Sept. 2014), p. 092705. DOI: 10.7567/APEX.7.092705.

[19] J. E. Hastie, J.-M. Hopkins, S. Calvez, Chan Wook Jeon, D. Burns, R. Abram, E. Riis, A. I. Ferguson, and M. D. Dawson. "0.5-W single transverse-mode operation of an 850-nm diode-pumped surface-emitting semiconductor laser". In: *IEEE Photonics Technology Letters* 15.7 (July 2003), pp. 894–896. DOI: 10.1109/LPT.2003.813446.

[20] R. Abram, K. Gardner, E. Riis, and A. I. Ferguson. "Narrow linewidth operation of a tunable optically pumped semiconductor laser." In: *Optics express* 12.22 (2004), pp. 5434–9. DOI: 10.1364/OPEX.12.005434.

[21] L. Fan, C. Hessenius, M. Fallahi, J. Hader, H. Li, J. V. Moloney, W. Stolz, S. W. Koch, J. T. Murray, and R. Bedford. "Highly strained InGaAsGaAs multiwatt vertical-external-cavity surface-emitting laser emitting around 1170 nm". In: *Applied Physics Letters* 91.13 (2007), pp. 2005–2008. DOI: 10.1063/1.2790838.

[22] J. Paajaste, S. Suomalainen, R. Koskinen, A. Härkönen, M. Guina, and M. Pessa. "High-power and broadly tunable GaSb-based optically pumped VECSELs emitting near 2μm". In: *Journal of Crystal Growth* 311.7 (Mar. 2009), pp. 1917–1919. DOI: 10.1016/j.jcrysgro.2008.10.071.

[23] S. Sayama and M. Ohtsu. "Tunable UV CW generation by frequency tripling of a Ti:sapphire laser". In: *Optics Communications* 137.4-6 (May 1997), pp. 295–298. DOI: 10.1016/S0030-4018(96)00799-7.

[24] X. Zhang, Z. Wang, G. Wang, Y. Zhu, Z. Xu, and C. Chen. "Widely tunable and high-average-power fourth-harmonic generation of a Ti:sapphire laser with a KBBOF prism-coupled device". In: *Optics Letters* 34.9 (May 2009), p. 1342. DOI: 10.1364/OL.34.001342.

[25] C. M. N. Mateo, U. Brauch, H. Kahle, R. Bek, T. Schwarzbäck, M. Jetter, M. Abdou Ahmed, P. Michler, and T. Graf. "Efficiency and power scaling of in-well and multi-pass pumped AlGaInP VECSELs". In: *SPIE 9734*. Ed. by K. G. Wilcox. Mar. 2016, p. 973410. DOI: 10.1117/12.2212162.

CHAPTER 5

Interpretation / modelling

5.1 Introduction

This chapter aims to study certain theoretical aspects of the THG experiment discussed in the previous chapter, acting as a complement and helping us to increase our understanding of the limitations of the conversion processes taking place. The chapter is divided in two main sections: beam propagation and power estimation; with a last section suggesting alternatives to optimize the system based on what we have learned.

5.2 Beam propagation

Calculating the beam geometry inside a laser resonator is essentially straightforward when dealing with a single, fundamental beam inside a laser cavity: any resonator software may be used to calculate the beam profile at every point within the cavity. Accurate estimation of the beam profile within complex cavities with narrow stability regions is, however, more difficult since a small variation in the distance between mirrors

(e.g. 1 mm) can lead to a large variation in the beam waist of the laser beam (e.g. tens of micrometres). This is of paramount importance when carrying out frequency conversion experiments, since the conversion efficiency is inversely proportional to the square of the beam waist, highlighting the importance of careful optimization of the process.

Intracavity tripling via SHG plus SFG adds complexity when trying to ascertain the beam sizes, since the second harmonic beam, output of the SHG process and input of the SFG process, cannot be calculated with the aforesaid method. Its initial geometry will be determined by the geometry of the fundamental beam inside the SHG crystal and the conversion process, while its evolution obeys beam propagation rules through the cavity mirrors (aligned for optimum fundamental operation). This section will cover the generation and propagation (in terms of geometry) of the second harmonic beam, study the beam geometry in our experimental cavities and try to describe the resulting alignment challenges for intracavity tripling.

5.2.1 Initial state of the second harmonic beam

An intuitive way of visualizing the SHG process is the fundamental, Gaussian beam generating second harmonic Gaussians at every point of its beam path inside the crystal. These second harmonic waves will interfere with each other, constructively in the optimum case, to produce the final second harmonic beam we observe outside the nonlinear crystal. If the second harmonic polarization is extraordinary all the components will suffer walk-off, deviating from the optical axis depending on the length of the crystal they have to travel through. The interference results in a distorted Gaussian beam at the exit of the nonlinear crystal. This process was extensively studied by Kleinman *et al.* [1], obtaining an expression for the external harmonic field that we reproduce in the modern form proposed here [2]:

$$E_2(x',y',z') = \frac{-ik_2}{2n^2} d_{\text{eff}} \frac{E_0^2}{2} e^{-\frac{\alpha_2}{2}L} \frac{2n}{n+1} \times \\ \times \int_0^L \frac{e^{-\alpha z} e^{i\Delta k z}}{1+i\zeta} \left[\frac{1}{1+i\zeta'} e^{-\frac{2\left[(x'-\rho(L-z))^2 + (y')^2\right]}{w_0^2(1+i\zeta')}} \right] \mathrm{d}z \tag{5.1}$$

$$\begin{array}{lll} \alpha = \alpha_1 - \frac{1}{2}\alpha_2 & y' = y & \zeta = 2\dfrac{\left(z - \frac{L}{2}\right)}{b} \\ x' = x + \rho(L-z) & z' = z & \zeta' = 2\dfrac{\left(z' - \frac{L}{2}\right)}{b} \end{array} \tag{5.2}$$

In this equation, the α_i coefficients correspond to the absorption suffered by each beam inside the nonlinear crystal, ρ is the walk-off angle, n the refractive index (equal for both wavelength for phase-matched SHG), d_{eff} is the nonlinear coefficient and L, the length of said crystal. The coordinates x, y define the position with respect to the optical axis and z is the coordinate along the optical axis, with $z = 0$ at the beginning of the crystal. Δk corresponds to the phase mismatch, while k_i are the wavevectors. Finally, E_0 is the amplitude of the fundamental field, w_0 the beam waist radius and b the confocal parameter.

Applied to our experimental setup, where the fundamental beam has a beam waist of 14 µm radius at the centre of the SHG crystal, we can calculate the resulting beam profile at the exit of said crystal. The fundamental profile is calculated by Gaussian propagation, while the profile of the second harmonic is calculated with equation (5.1). Both beam profiles at the exit of the SHG crystal are plotted in figure 5.1.

The profile of the second harmonic is a distorted Gaussian: the distortion occurs on the side affected by walk-off; the right side of the second harmonic profile is Gaussian. The Gaussian fit is utilised as the theory used in the following section is developed for Gaussian beams.

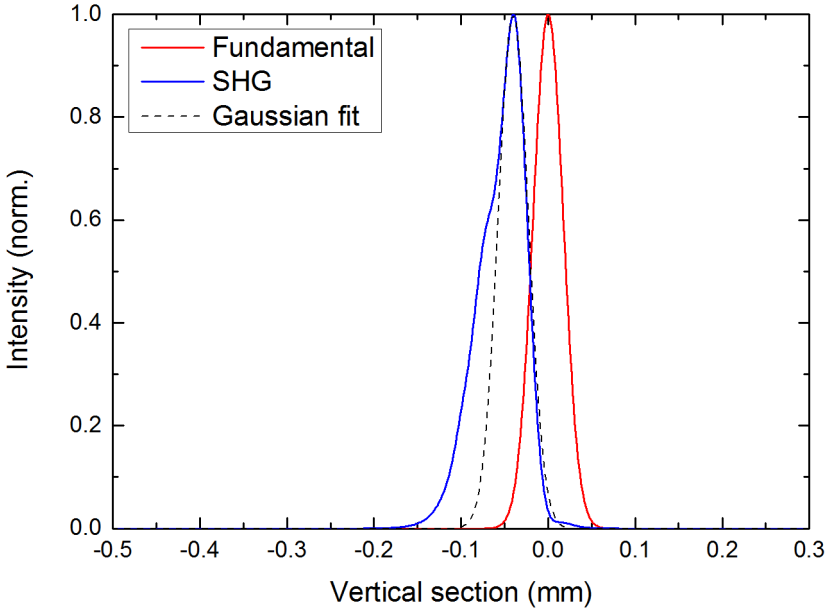

Figure 5.1: Beam profiles at the exit of the SHG crystal. A Gaussian profile has been fitted to the SHG beam, in order to define the beam size. The beam profiles correspond to the vertical section, which is the direction of effect of the walk-off. The zero corresponds to the optical axis of the cavity, on which the fundamental beam is centred.

5.2.2 Ray transfer matrix analysis

Ray transfer matrix analysis, also known as ABCD formalism, is a simple yet powerful technique to propagate light rays (off axis) or Gaussian beams (on axis) through an optical system. A detailed analysis can be found in the literature [3]. The Gaussian beams are defined at any given point z by a complex beam parameter $q(z)$, expressed as:

$$\frac{1}{q(z)} = \frac{1}{R(z)} - \frac{i\lambda_0}{\pi n w^2(z)} \tag{5.3}$$

R corresponds to the radius of curvature of the beam wavefront at the given distance z, λ_0 is the vacuum wavelength, n the refractive index of the medium and w the beam waist (radius). It can be also defined in terms of the Rayleigh length and cavity distances:

$$q(z) = (z - z_0) + iz_R \tag{5.4}$$

Where z_0 is the position of the beam waist and z_R the Rayleigh length.

The matrices of the optical elements are two dimensional (having four components, hence the ABCD name), and the most common are shown in table 5.1. Matrices of several optical elements can be multiplied to obtain the matrix of the total system. In fact, resonator stabilities are usually calculated with this method. The evolution of a given beam characterized by its complex beam parameter (q_1) can be studied by applying the system matrix to it:

$$q_2 = \frac{Aq_1 + B}{Cq_1 + D} \tag{5.5}$$

Table 5.1: Most common ABCD matrices [3].

Propagation in a medium of constant refractive index	Refraction at a flat interface	Reflection from a flat mirror
$\begin{bmatrix} 1 & d \\ 0 & 1 \end{bmatrix}$	$\begin{bmatrix} 1 & 0 \\ 0 & \frac{n_1}{n_2} \end{bmatrix}$	$\begin{bmatrix} 1 & 0 \\ 0 & 1 \end{bmatrix}$
Thin lens	**Refraction at a curved interface**	**Reflection from a curved mirror**
$\begin{bmatrix} 1 & 0 \\ \frac{-1}{f} & 1 \end{bmatrix}$	$\begin{bmatrix} 1 & 0 \\ \frac{n_1 - n_2}{R n_2} & \frac{n_1}{n_2} \end{bmatrix}$	$\begin{bmatrix} 1 & 0 \\ \frac{-2}{R} & 1 \end{bmatrix}$

While this method deals exclusively with on-axis beams, it can be generalized to work with off-axis beams, as in our case, by means of order 3 matrices [4]. The drawback of this approach is, of course, an increased complexity of the method. It is for this reason that we instead make use of a different and indeed useful analytical tool for optical processes: Fourier analysis.

5.2.3 Fourier optics

Fourier analysis has been successfully applied to many different physical problems with excellent results, and the field of optics is no exception. This method, based on the fundamental concept of representing a general function as the integral of simpler trigonometric functions, offers an excellent approach to beam propagation (among other problems), in particular in the case of off-axis beams. The propagation of a (Gaussian) beam within an optical system becomes significantly simpler in our case, comprising nothing more than free space and mirrors (an interface between two media has to be considered as well for evaluating the propagation inside the SFG crystal). Fourier analysis is described in detail elsewhere (see e.g. [5]), thus this section is limited to articulating the objects of interest to this work.

An optical wave can be expressed in the Fourier domain by means of its Fourier transform. Changing the domain can simplify certain operations. In particular, the Fourier transform of a beam displaced in space equals the Fourier transform of the original beam multiplied by the propagator function $H(z, \sigma, \lambda)$:

$$H(z, \sigma, \lambda) = \exp\left(\mathrm{i}\frac{2\pi}{\lambda} z\sqrt{1 - \lambda^2\sigma^2}\right) \tag{5.6}$$

In this equation z is the propagation distance and σ the spatial frequency in the Fourier domain. The wavelength is defined as $\lambda = \lambda_0/n$.

The focussing effect of the curved mirror is taken into account by applying a spherical phase:

$$T(x, \lambda) = \exp\left(\frac{\mathrm{i}\pi x^2}{\lambda\frac{R}{2}}\right) \tag{5.7}$$

Here, the focusing distance has been substituted by half of the mirror radius, as described by the paraxial approximation ($f = R/2$).

5.2.4 General propagation

Both methods mentioned give similar results when applied to our system. The Fourier approach was used because its treatment of off-axis beams is more straightforward than that of the matrix method. The Gaussian beams plotted in figure 5.1 are now the input for the Fourier algorithm, and will be propagated through both 6-mirror and 5-mirror cavities to obtain their geometry inside the BBO crystal, where the SFG process takes place.

The propagation process itself is similar in both 6-mirror and 5-mirror cavities:

1. We take the output beams from the SHG crystal and propagate them using equation (5.6) through distance d_3 until we reach mirror M_4.

2. Equation (5.7) is then used to compute the reflection on mirror M_4.

3. As in the first step, the beams are propagated through distance d_4.

4. In the 6-mirror cavity, propagation through one more mirror and distance has to be considered before arriving at the SFG crystal, while in the 5-mirror cavity the SFG crystal is after distance d_4, as can be seen in figures 4.10 and 4.14. In both cases the BBO crystal for SFG is positioned at the waist of the fundamental beam. The SHG beam focuses at a different distance from the mirror due to the different angle of divergence. This would not be the case if both beams had the same confocal parameter, but the walk-off suffered by the SHG beam modifies it, as the output beam will be composed by a superposition of Gaussian components.

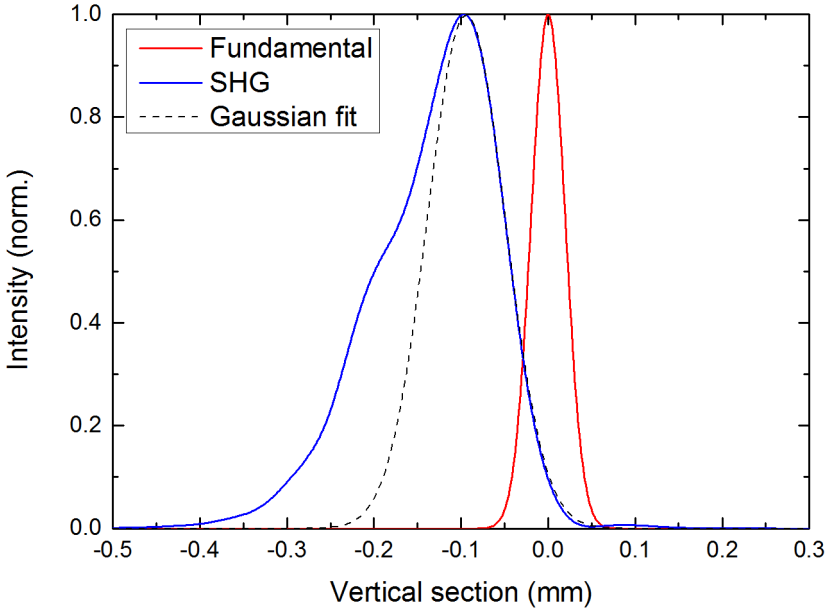

Figure 5.2: Beam profiles at the centre of SFG crystal in the 5-mirror cavity. SHG beam has separated from the cavity axis during the propagation from the SHG crystal.

5. We now calculate the geometry of both beams for every point inside the SFG crystal, so we can observe the evolution of the beam sizes, position and overlap within said crystal.

As seen in figure 5.1, the maximum intensity of the SHG beam starts located 40 µm away from the optical axis of the cavity, where the fundamental beam is centred. The effect of walk-off on the beam shape is visible on the left side of this profile, which is wider and exhibits additional features. At the exit of the crystal the fundamental beam size is 35 µm radius, while the beam size of a Gaussian fit of the SHG is 50 µm radius.

Propagation through the 5-mirror cavity

Propagating the beams over our 5-mirror cavity yields a detailed vision of the beam geometry inside the SFG crystal. We have depicted in figure 5.2 the fundamental and

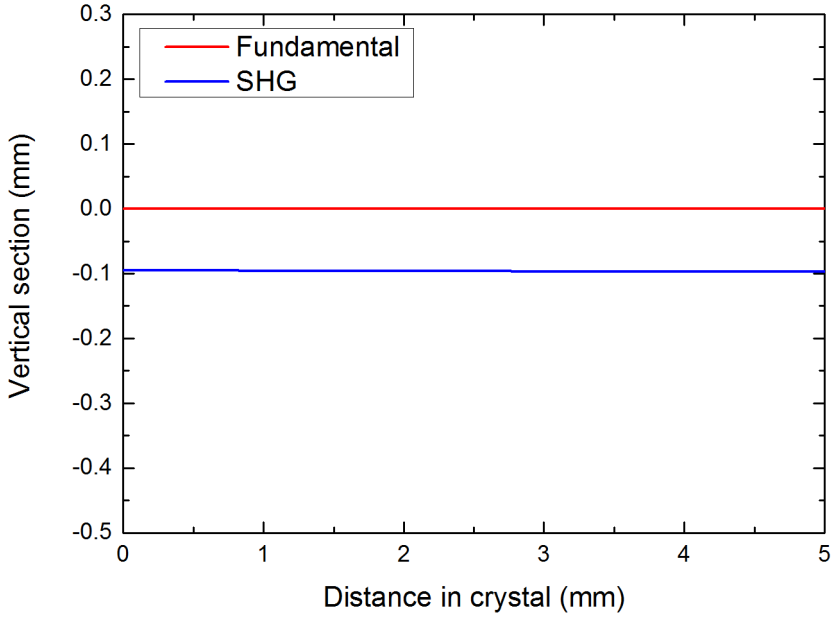

Figure 5.3: Fundamental and SHG beam paths inside SFG crystal in 5-mirror cavity configuration.

SHG beams (together with a Gaussian fit of the SHG beam) at the centre of the SFG crystal.

The propagation of the fundamental beam shows a beam waist of 40 µm radius, in agreement with the value obtained when designing the cavity, as described in the previous chapter. The Gaussian fit of the SHG beam has a beam waist of 91 µm radius. While the focusing size of this second beam should ideally be tighter, the limitations in the cavity design make it difficult to improve it. In exchange, both beams are, if not collinear, at least close to parallel (with the SHG optical path presenting an angle of only 0.4 mrad), as can be seen in figure 5.3, where the optical path (defined by the position of the peak of each beam) has been plotted.

This parallelism is crucial since we have chosen our crystal to be cut for SFG with parallel beams. It is worth mentioning that, although there are a number of publications dealing with noncollinear phase matching, they refer to crossing beams, rather than noncollinear, parallel beams. We have not been able to find any study on noncollinear parallel beams,

probably because type-I phase matching for SHG at longer wavelengths, typically 1064 nm to 532 nm or longer, offers a much smaller walk-off angle (especially in LBO: $\rho <$ 10 mrad) between the fundamental and the second harmonic beam. With such small walk-off angles the separation between these beams, which are the input for the SFG process, is negligible.

Propagation through the 6-mirror cavity

The first thing we notice when examining the beam profiles inside the BBO crystal in the 6-mirror cavity configuration (figure 5.4) is that both peaks are separated a shorter distance than in the 5-mirror cavity: 45 µm. The beam size of the fundamental beam is again 40 µm, while the SHG beam presents a much tighter focus as compared with the previous cavity configuration (36 µm). The extra optical arm and mirror in this cavity (as compared with the 5-mirror cavity) allow for more control over the geometry of the beams. It is then possible to make the SHG beam to cross the fundamental beam closer to the point where they focus.

The drawback of this approach is that the angle between these beams is large (6 mrad in our case) as can be seen in figure 5.5. Having a large angle between the beams is far from ideal, given that our SFG crystal is cut for type-I phase matching with parallel beams. This noncollinearity can be taken into account [6], obtaining a phase-mismatching $\Delta k \cdot L \sim 9$ and thus dramatically reducing the SFG process efficiency (for the previous case of 0.4 mrad in the 5 mirror cavity $\Delta k \cdot L < 1$, with a much smaller effect on the conversion efficiency). How the SFG process is affected by phase matching can be found in figure 5.12.

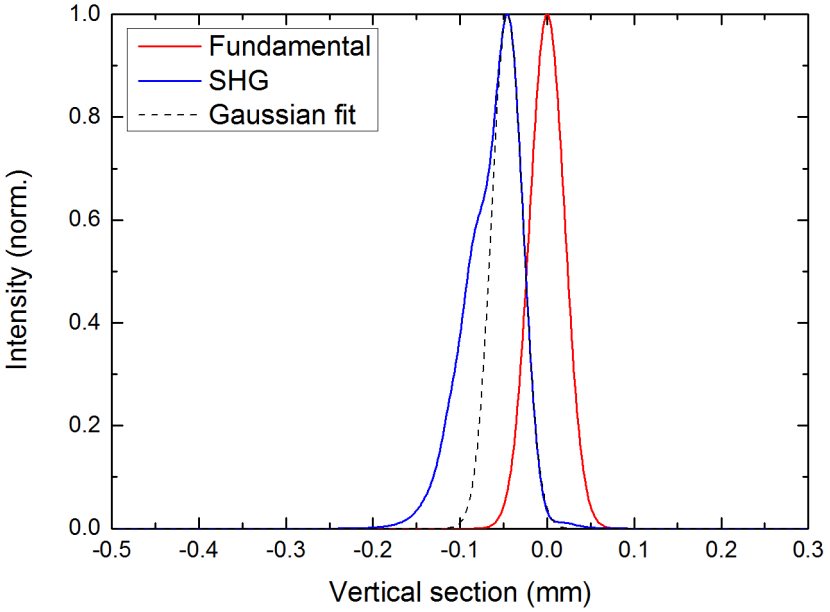

Figure 5.4: Beam profiles at the centre of SFG crystal in the 6-mirror cavity. The beams are much closer in this configuration as compared with the 5-mirror cavity.

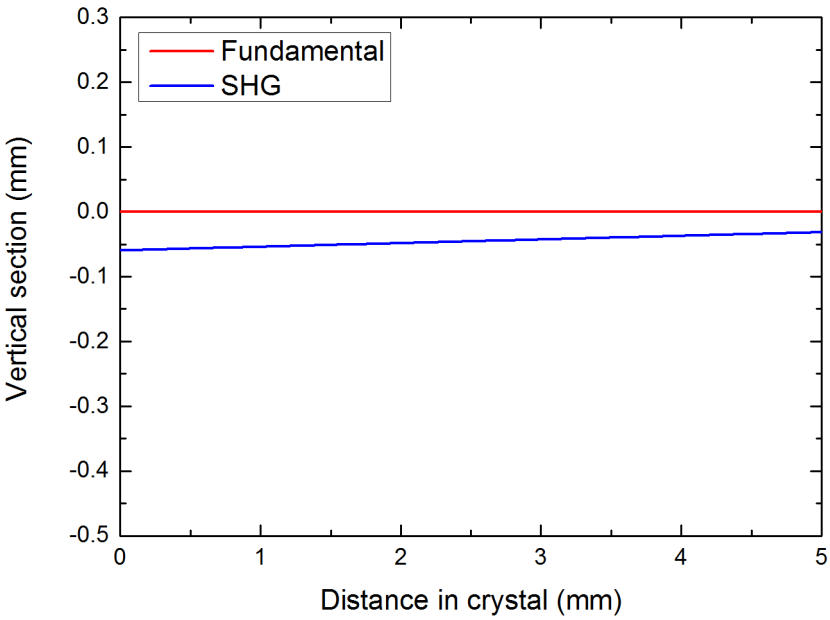

Figure 5.5: Fundamental and SHG beam paths inside SFG crystal in 6-mirror cavity configuration.

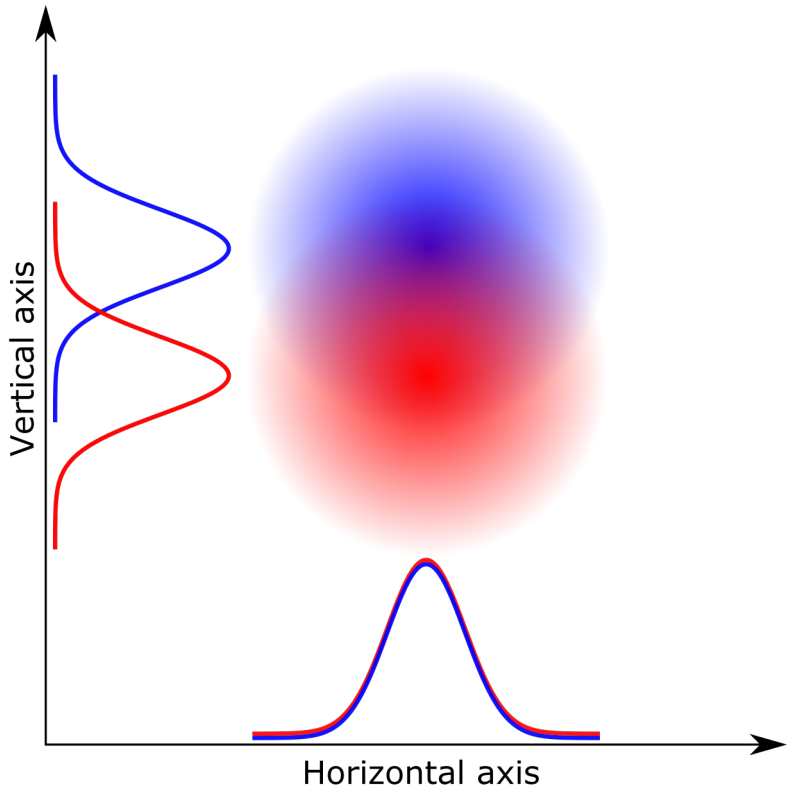

Figure 5.6: Overlapping beams decomposed in horizontal and vertical components. This drawing shows that the overlap mismatch happens in the vertical axis, while the beams superpose well in the horizontal axis.

5.2.5 Beam overlap

Seeing that the beams are not collinear, but present a lateral separation in the SFG crystal, we attempt to quantify the overlap between the fields to get an idea of the effect this lateral displacement may have on the conversion efficiency of the process. The overlap is calculated considering the fields, rather than the intensities, using the equation:

$$\eta = \frac{\left| \int_A E_1^* E_2 \, \mathrm{d}A \right|^2}{\int_A |E_1|^2 \, \mathrm{d}A \int_A |E_2|^2 \, \mathrm{d}A} \tag{5.8}$$

Although this equation considers a two-dimensional overlap, we can separately consider the horizontal and vertical components of our beams as depicted in figure 5.6, effectively simplifying the calculations by removing the need of calculating the X-axis overlap, since it is already taken into account by the theory (see next paragraph).

Theory of harmonic generation, which we will introduce in section 5.3.1, later on this chapter, considers collinear beams, but allows for different beam size. This means that if we use only equation (5.8) to calculate the absolute overlap, we would be taking the different beam size twice into account. We will therefore calculate also the overlap of the same beams as if they were collinear, and use this value as a normalization to obtain the effective overlap of the input beams.

$$\eta_{\text{eff}} = \frac{\eta}{\eta_{\text{centred}}} \tag{5.9}$$

Overlap in 5-mirror cavity

The fundamental and SHG overlapping fields are plotted in figure 5.7, as a cross section of the vertical axis (the walk-off direction in our experiment).

The overlap between these fields can be calculated at each point in the SFG crystal (figure 5.8). The overlap is affected by the spatial positioning of the beam as well as the focusing, and therefore it changes throughout the crystal length. In the 5-mirror cavity configuration, the overlap is rather constant, around 15 % over the whole crystal.

While the Gaussian fit is accurate on the overlapping side of the beam, the extra area on the other side produces a small deviation in the overlapping values considering the real SHG field or the Gaussian fit. Figure 5.7 shows that the values obtained using either field do not differ more than a few units. The Gaussian fit of the SHG field comprises almost 70 % of the SHG power.

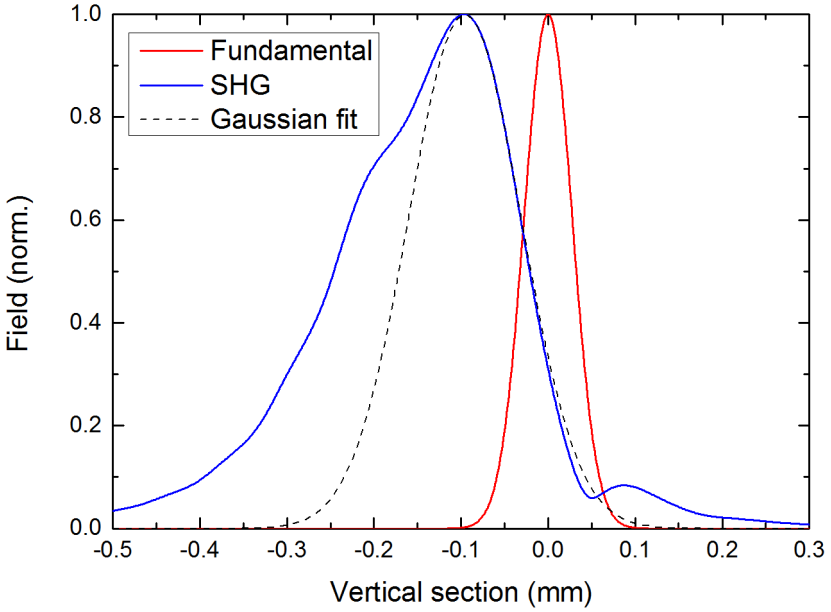

Figure 5.7: Electric fields of fundamental and second harmonic beams in 5-mirror cavity configuration.

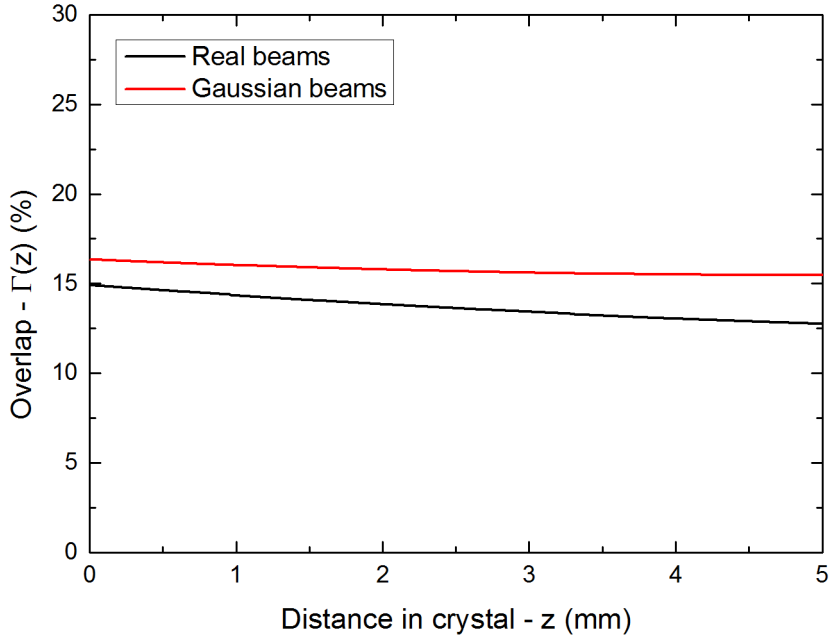

Figure 5.8: Calculated overlap inside SFG crystal in 5-mirror cavity configuration.

Overlap in 6-mirror cavity

The 6-mirror cavity configuration, as described above, offers a tighter SHG focus and closer beams, since they cross near the focus. For this reason the overlap is higher than in the 5-mirror configuration, although this result does not take into account the fact that the beams are not parallel anymore, but traveling with an angle of 6 mrad (figures 5.9 and 5.10).

The maximum overlap seems to happen after the crystal, where both beams cross. One could think that placing the crystal at that point would increase the conversion efficiency of the process, however since the beam size will be larger at that point, offering a low photon density, the generated output power would be extremely low even with perfect overlap. Experimentally, the crystal is positioned at the point that maximizes the process, at (or near) the focusing point of the fundamental beam: the large intensity of this beam is hardly comparable with any other variable of the system, and any configuration that diminishes its effect necessarily decreases the conversion efficiency.

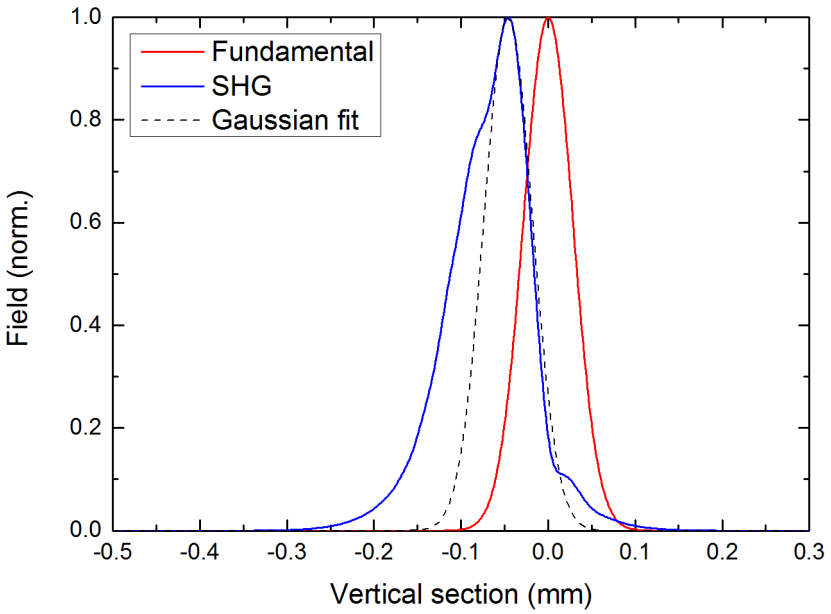

Figure 5.9: Electric fields of fundamental and second harmonic beams in 6-mirror cavity configuration.

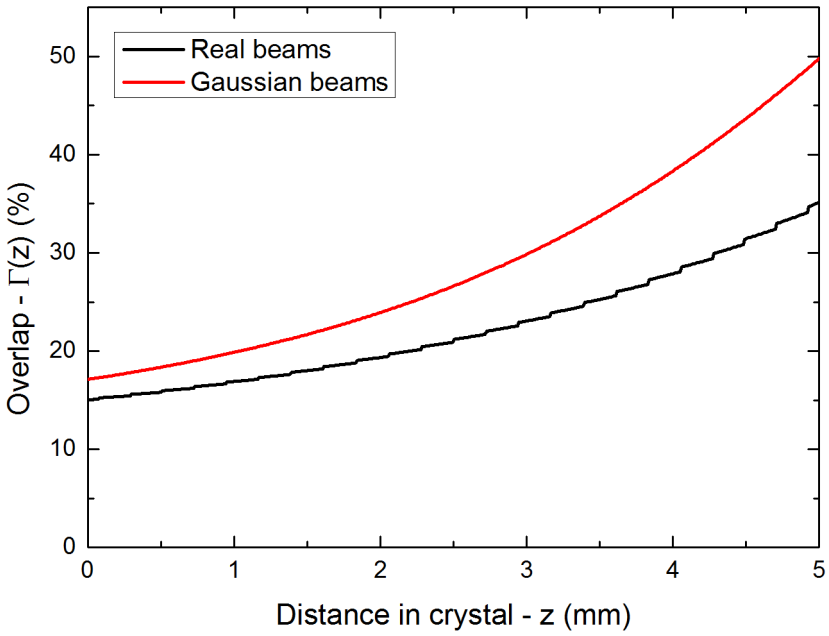

Figure 5.10: Calculated overlap inside SFG crystal in 6-mirror cavity configuration.

5.2.6 Overlap compensation by crystal orientation

The calculation of the overlap for the 5-mirror cavity offers a low value that does not match very well with the calculated output power of the SFG process (see next part of the chapter). The output power estimations are, of course, nothing more than that: their main purpose is to give us an idea of the order of magnitude of the expected output, rather than a precise value. Nevertheless we considered the possibility that the crystal orientation (in the case of non-normal incidence) could modify the beam path to provide some improved overlap (figure 5.11). We must remember that being a tunable laser, the fundamental (and thus SHG) wavelength can change, and the crystal orientation needs to be such that fulfils the phase matching condition for the three beams involved. Therefore, crystal orientation always depends on the exact wavelength of the beams. On the other hand, and as shown in figure 5.12, zero phase-mismatch is not always the optimum solution, or there may be some flexibility around the optimum value (loose focus does not require as precise phase matching values as tight focus). In

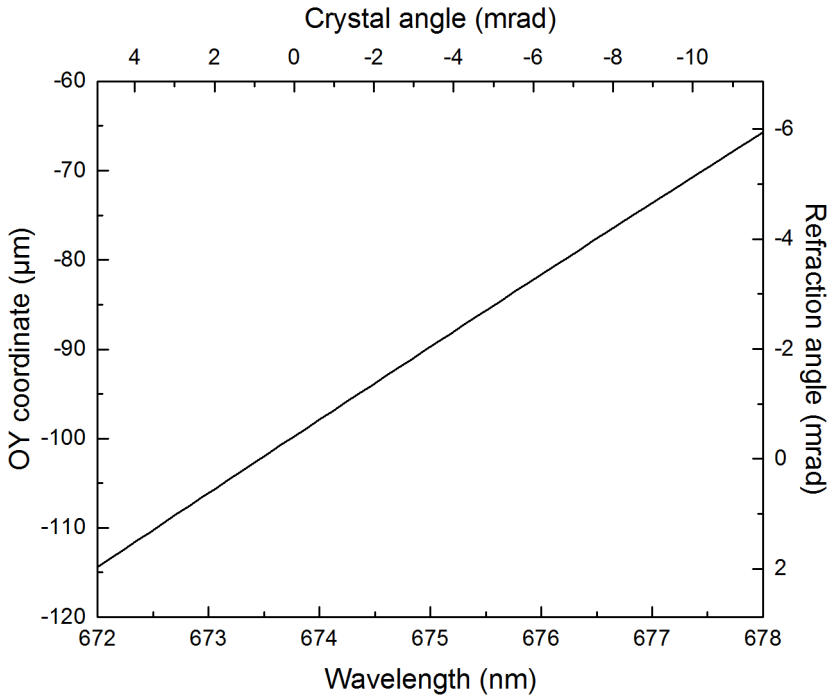

Figure 5.11: Vertical position of the SHG maximum at the end of the SFG crystal. The beam enters the crystal at 100 µm from the fundamental beam (centred at 0). The angle of the SFG crystal can be varied to take advantage of refraction to rejoin both beams. A particular wavelength can be assigned to each crystal angle so the phase matching is maximized.

the figure we use the walk-off parameter B, defined in section 5.3 and equation (5.16), as a measurement of the walk-off angle.

We have calculated the possible modification to the beam path of the SHG with respect to the fundamental beam when the crystal is tilted from normal incidence orientation to the phase matching angle, finding that the refraction suffered by the beams could bring them closer together as much as 30 µm µm (in normal incidence configuration they are separated almost 100 µm.

In addition to this result, further tilting of the crystal (taking advantage of the wide phase matching region, showed in figure 5.12 compared to a zero walk-off system) could reduce this distance even more. The drawback this refraction would have is a reduced conversion efficiency due to the increased angle between the input beams. Quantifying

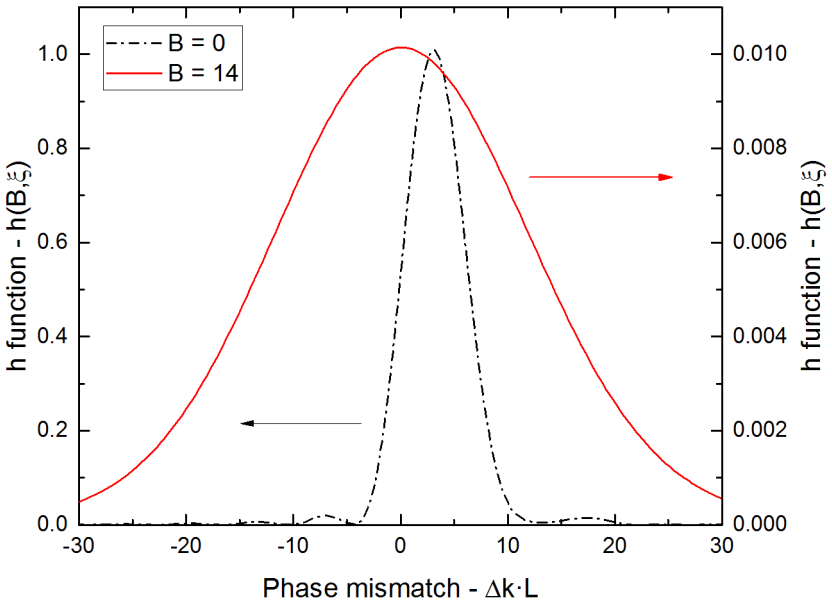

Figure 5.12: Effect of phase matching in the SFG process. For $B = 14$ curve the peak is centred at $\Delta k = 0$. For $B = 0$ curve the optimum phase matching value is greater than 0. The walk-off parameter B is described in section 5.3.

the gain or loss obtained with this overlap compensation by evaluating proximity versus collinearity is an arduous task already, but it becomes so even more when noticing that probably noncollinear phase matching should also be taken into account.

5.2.7 Summary of the section

The main (and most accurate result) we have obtained from this section are the beam sizes inside the SFG crystal. We have used both Fourier propagation and ray transfer matrix analysis to obtain the evolution of the beam geometry inside our 5-mirror and 6-mirror cavity, from the SHG crystal to the SFG crystal. Now that we know how the beams behave inside the SFG crystal, we are prepared to calculate an estimation of the achievable power with this process.

5.3 Theoretical study of SFG

Output power from nonlinear processes has been studied in detail since the early 60s, when the invention of the laser gave access to the field of nonlinear optics. Franken *et al.* [7] showed the first experimental result on harmonic generation from a ruby optical maser in 1961. Harmonic generation has been since extensively studied [1, 8–11]. The paper published by Boyd and Kleinman in 1968 is probably the most complete [12], summing up previous results and offering an in-depth study of several frequency conversion processes. While this is probably the most comprehensive study on the topic, the study of the SFG process is limited to Gaussian beams with equal confocal parameter. Such confocal parameter is defined as:

$$b = 2z_0 = \frac{2\pi w_0^2}{\lambda} \tag{5.10}$$

This limitation means the beam waists of the input beams follow the relation:

$$w_{0,2} = \frac{w_{0,1}}{\sqrt{2}} \tag{5.11}$$

Guha and Falk ([13]) extended the theory of the SFG process to describe the mixing of focused beams with different confocal parameters. Their result reduces to that of ([12]) when using equal confocal parameters. The output power of the SFG beam, third harmonic in our case, would be:

$$P_3 = \frac{32\pi^2 d_{\mathbf{eff}}^2}{\epsilon_0 c n_3^2 \lambda_1 \lambda_2 \lambda_3} P_1 P_2 e^{-\frac{1}{2}(\alpha_1+\alpha_2+\alpha_3)L} Lh \tag{5.12}$$

Where the h function, analogous to that of [12], can be expressed as:

$$h = \frac{1}{4\xi_4} I \tag{5.13a}$$

$$I = \int_0^1 \int_0^1 \mathrm{d}z_1 \, \mathrm{d}z_2 \times \frac{\exp\left[i\Delta k L \left(z_1 - z_2\right)\right] \exp\left[-\left({}^{4B^2}/_{\beta}\right)\left(z_1 - z_2\right)^2 f\right]}{\left(z_1 - A_1\right)\left(z_2 - A_1^*\right) + C_1} \tag{5.13b}$$

The parameters used in this equation are defined as follows:

$$\xi_1 = \frac{L}{b_1} \qquad \xi_2 = \frac{L}{b_2} \tag{5.14}$$

$$\begin{aligned} k &= \frac{k_1}{k_2} & \xi_3 &= \frac{\xi_1 \xi_2 \left(1 + k\right)}{\xi_2 + k\xi_1} \\ \xi_4 &= \frac{\xi_1 + k\xi_2}{1 + k} & \beta &= \frac{\xi_1 + k\xi_2}{\left(1 + k\right)\xi_1 \xi_2} \\ A_1 &= \frac{1}{2} + \frac{i}{4}\left(\frac{1}{\xi_3} + \frac{1}{\xi_4}\right) & C_1 &= -\frac{1}{16}\left(\frac{1}{\xi_3} - \frac{1}{\xi_4}\right)^2 \\ z_3' &= \frac{1}{2} + \frac{i}{2\xi_3} & f &= \frac{\left(z_1 - z_3'\right)\left(z_2 - z_3'^*\right)}{\left(z_1 - A_1\right)\left(z_2 - A_1^*\right) + C_1} \end{aligned} \tag{5.15}$$

$$B = \frac{\rho}{2}\left[\frac{L\left(k_1 + k_2\right)}{2}\right]^{1/2} \tag{5.16}$$

We can then consider different parameters as variables, modifying them to investigate how each of them affects the output of this nonlinear process, gaining a deeper understanding on how sum-frequency generation works. Some of these parameters are mainly for physical or mathematical simplification and little attention will be paid to them (A_1, C_1, ξ_3, ξ_4, z_3', f). However the focusing parameters (ξ_1, ξ_2) and the walk-off parameter (B) are of particular importance, and we will refer to them often in this

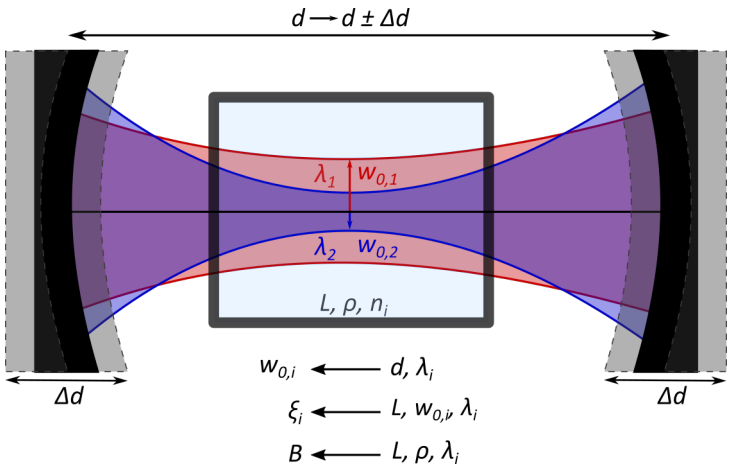

Figure 5.13: Representation of the different parameters involved in the following calculations. Beam geometry (in particular beam waist) is strongly dependent on cavity geometry and beam wavelength. The focusing factor represents the amount of focusing inside the crystal (and so it is inversely proportional to the beam waist). The walk-off parameter accounts for the walk-off of a beam of given wavelength in a crystal of length L.

section. As described before, b is the confocal parameter, L is the crystal length and k_i are the wavevectors. Figure 5.13 represents a simplified cavity, depicting how the aforementioned parameters are varied.

5.3.1 Power estimation

Equation (5.12) can be used to estimate output power from the SFG process as long as we know every parameter involved. While some of those refer to the basics of the system (wavelength, crystal length or properties...) others depend on the particular characteristics of our experiment and have to be measured. However, we suffer from limitations on what we can measure in our experiment, the beam waist inside the crystals being the obvious example.

We have seen in the first part of this chapter how beam propagation can be studied to obtain the waists of both beams (fundamental and SHG) in the SFG crystal based on the beam size of the fundamental beam inside the SHG crystal. Of course this value of

the fundamental beam waist in the SHG crystal is also theoretical, but being based on the geometrical properties of the cavity, and given the narrow stability region, we can be certain it is a reasonable value.

Another source of uncertainty is the actual beam powers. Due to experimental limitations, initially we were unable to simultaneously measure the fundamental leaking power, the SHG output power and the THG output power. While this was solved at a later stage of the process, degradation on the SDL sample was already limiting the efficiency of the process. The fundamental output power, measured from the leak of one of the HR mirrors, is a direct measurement of the intracavity power, with an error of no more than a couple of watts (caused by the accuracy on determining the mirror transmittance). The SHG output power was measured directly at every stage of the setup building process, except when third harmonic generation was achieved. Of course measuring the THG power was a priority. The SHG power is therefore estimated from previous measurements, assuming similar process efficiency.

Once we know every variable needed, as shown in table 5.2, we are finally ready to begin with the calculations. Equation (5.12) gives an output power centred around 100 µW at the third harmonic wavelength of 224.5 nm. This value, an approximation due to the strong dependence to variations in the input powers P_ω and $P_{2\omega}$, is on the same order of magnitude of our experimental result, suggesting that both mirror and crystal alignment was successful, maximizing the output power for the current system configuration.

This result itself does not give much insight on the process apart from providing reassurance that our experiment is well-optimised within the current set-up. However we are now able to study how the THG output power behaves as a function of several of the variables involved. The following sections will deal with these calculations, considering different crystal lengths, beam sizes and variation of the B parameter itself; for an in-depth study of this complex nonlinear process.

Table 5.2: Experimental parameters.

λ_ω	$\lambda_{2\omega}$	w_ω^0	$w_{2\omega}^0$
674 nm	337 nm	39 µm	90 µm
P_ω	$P_{2\omega}$	L	d_{eff}
26 ± 4 W	26 ± 5 mW	5 mm	1.55 pm/V
n_ω	$n_{2\omega}$	$n_{3\omega}$	ρ
1.665	1.712	1.696	82.60 mrad

5.3.2 Effect of crystal length

Crystal length is probably one of the main decisions to make when designing the laser system. While sometimes there is an optimum crystal length, it is common that longer crystals offer better results, and it is then necessary to find a balance between crystal length and crystal price. Moreover, depending on the crystal it may happen that the current technology only allows for a limited-length growth/fabrication.

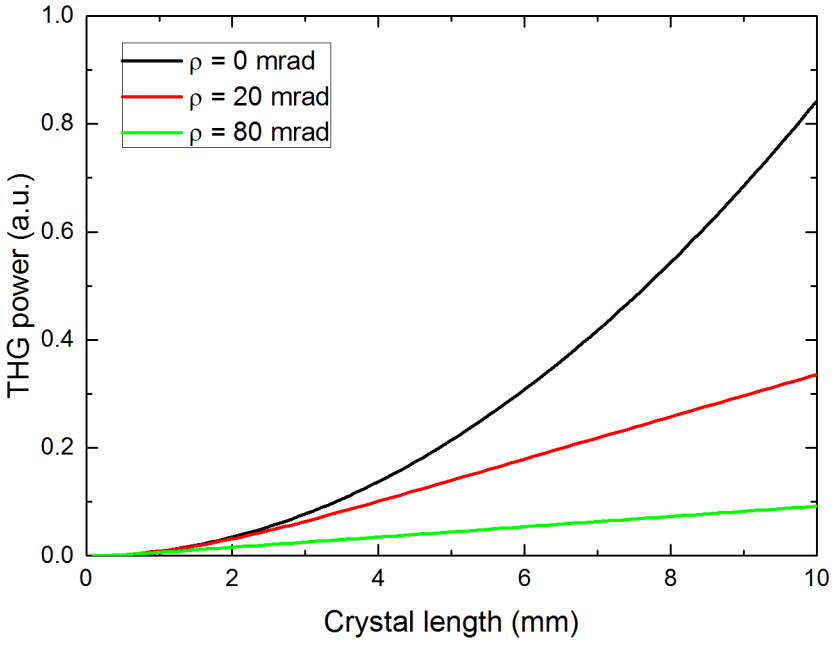

Figure 5.14: Evolution of the THG output power for different values of walk-off. Quadratic dependence is limited to systems with small values of the walk-off angle.

In the particular case of nonlinear frequency up-conversion, it is often thought that the output power is a function of the square of the crystal length; however this is only true when walk-off is not taken into account. For a given walk-off angle, the walk-off parameter equation (5.16) increases as the crystal is made longer, effectively decreasing the output power (if compared with the no-walk-off result). This is shown in figure 5.14.

We can observe how the THG output power shows a quadratic dependence with the crystal length for the case $\rho = 0$. This dependence drifts towards linear already for a walk-off angle of 20 mrad. For the case $\rho = 80$ mrad, close to our experimental conditions, we observe a linear dependence with a reduced slope, as compared with the $\rho = 20$ mrad case.

Since the walk-off parameter depends on the crystal length (apart from the walk-off angle and wave vector), it becomes larger as the crystal length increases, as shown in figure 5.15, effectively decreasing the conversion efficiency of the process.

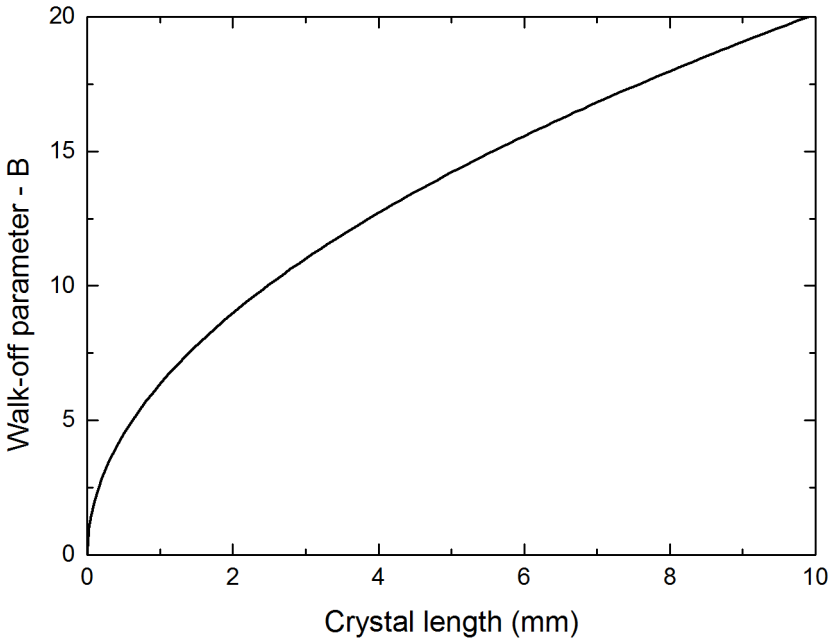

Figure 5.15: Walk-off parameter variation with increasing crystal length for SFG in BBO. A rapid rise is observed at the beginning (e.g. for the first 2 mm).

Crystal length also has an effect on the optimum beam sizes for the given crystal. In general, we can consider that the optimum beam sizes are those which make the confocal parameter equal to the crystal length (see discussion after figure 5.16). This definition still holds for intracavity frequency conversion as long as the conversion efficiency is much smaller than the optimum output coupling value of the cavity.

$$b = L \qquad w_0 = \sqrt{\frac{\lambda L}{2\pi}} \tag{5.17}$$

Therefore, the optimum beam sizes can be defined as:

$$w_{0,\text{fun}} = \sqrt{\frac{\lambda_1 L}{2\pi n_1}} \tag{5.18}$$

$$w_{0,\text{SHG}} = \sqrt{\frac{\lambda_2 L}{2\pi n_2}} \tag{5.19}$$

In figure 5.16, we can see the importance of choosing the optimum beam sizes for each particular crystal length has in the output power of the SFG process, compared with the output power for the estimated beam sizes of our system. Our system is very limiting in terms of beam size choice due to the narrow stability region and all the conditions to fulfil (size in SDL and both crystals specially). At the same time the SHG beam size is not independently set, but depends on the fundamental beam size in the SHG crystal and the geometry of the laser cavity.

The given definition for optimum beam sizes is a good approximation for small walk-off conditions (in the particular case of SHG, Boyd and Kleinman calculated the optimum value to be 2.84 [12]), but the larger the walk-off angle is, the more the optimum beam waist drifts towards looser focus. Figure 5.16 is therefore showing a suboptimum result, as will be seen in the following section.

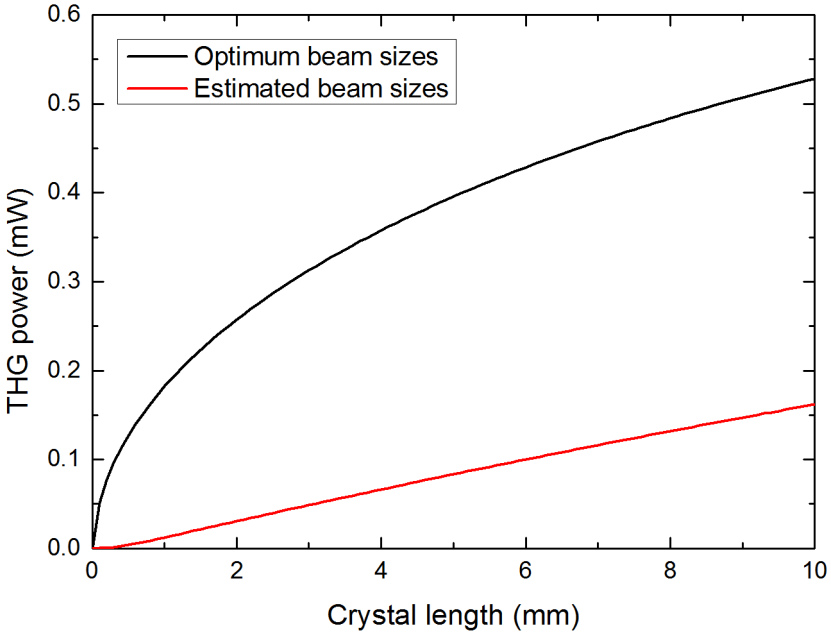

Figure 5.16: THG output power dependence for increasing crystal length comparing optimum beam sizes with the estimated beam sizes of our system.

5.3.3 Effect of beam sizes

In order to study the dependence of the SFG process with the beam sizes, or beam waists since one factor sets the other, it is sometimes convenient to think in terms of the focusing parameter (ξ_1 and ξ_2 in equation (5.13)). This parameter, defined as crystal length over confocal parameter ($\xi = L/b$), equals 1 when both quantities have the same value (corresponding to the condition described in the previous section for optimum beam sizes in the crystal). We can see in the figure 5.17 how the THG power is maximized around a focusing parameter of 1 (red line). Since both ξ_1 and ξ_2 affect the output power, ξ_2 is on the horizontal axis while different curves correspond to different ξ_1. A walk-off value of 82 mrad has been used in this calculation.

Figure 5.17 shows how every curve is maximized for similar values of both focusing parameters. It is also noticeable how the maximum efficiency would be found near $\xi_1 = \xi_2 = 1$ (indeed implying confocal parameters being close to crystal size), although from this graph we cannot tell where exactly (next section expands this information).

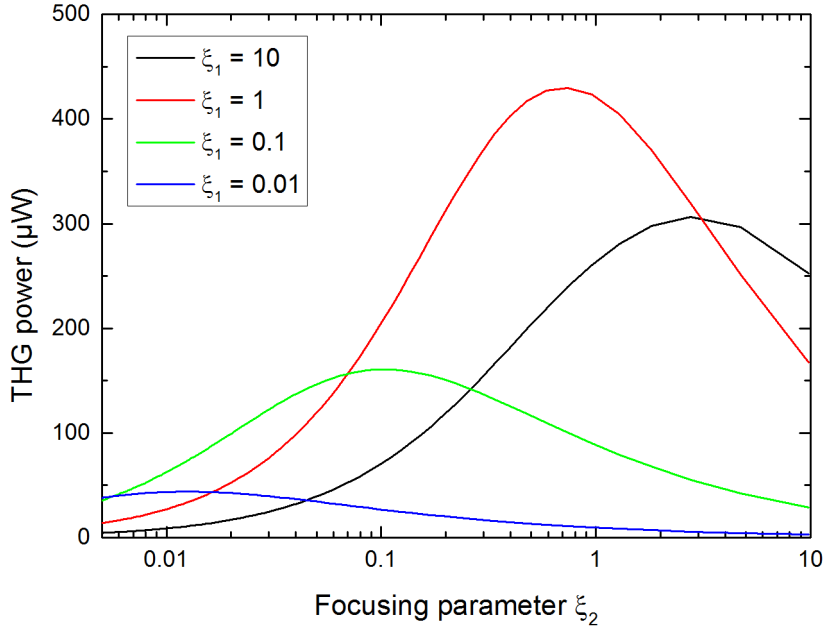

Figure 5.17: Calculated THG output power for different values of the focusing parameters of fundamental and SHG beams.

The effect space constraints caused by the laser cavity have on the conversion efficiency of the system can be inferred from this figure: if the beam sizes cannot be freely adjusted to the optimum values, a decrease of more than 50 % on the performance of the laser system is a reality.

If we calculate the direct dependence of the THG output power with the beam waists in the SFG crystal (figure 5.18), we can see how the optimum case occurs for both beams focusing to a 20 µm waist (black curve). Larger waists of the fundamental beam (different curves) demand larger waists of the SHG beam. Since in our system the beam size of the SHG beam depends on the beam size of the fundamental, and it is probably not possible to design a cavity to make the SHG waist smaller than the fundamental waist (the non-Gaussian shape of the SHG implies larger divergence), we have dashed the "unreachable" regions of the curves. For a SHG beam waist of ∼90 µm (as calculated for our laser setup) we can observe the output power to offer similar values for the different fundamental beam waists (except for the 20 µm curve). Since

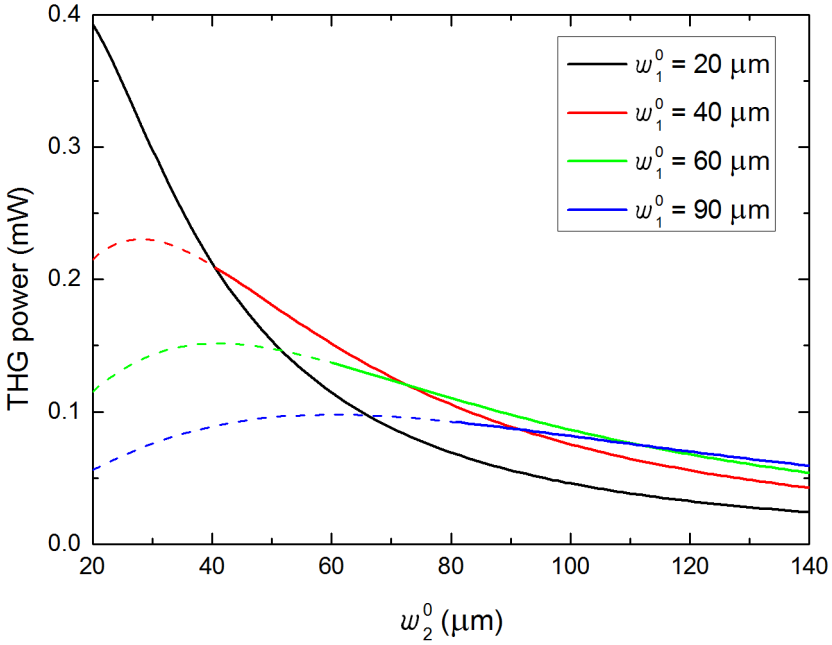

Figure 5.18: Direct comparison between calculated THG output power and beam waists. Since intracavity propagation of SHG produces a looser focus in the SFG crystal (around 90 µm), fundamental waist should not be too tight (over 40 µm).

the cavity is designed for a fundamental beam size of ∼40 µm in the SFG crystal, our system is represented by the red curve.

5.3.4 Effect of B parameter

As previously described, the walk-off angle is taken into account by means of the walk-off parameter (equation (5.16)), with a linear dependence between them (as opposed to the crystal length and wavevector, inside a square root). The evolution of the output power with varying walk-off angle can therefore be equally visualized considering the walk-off parameter. Figure 5.19 depicts said behaviour for an increasing walk-off parameter, with all other variables being set to the experimental values. The red dot corresponds to our experimental result, occurring at $B = 14$ (corresponding to $\rho = 82.60$ mrad). The effect the walk-off angle has on the SFG process is clearly shown here, as it decreases the output power of the system dramatically.

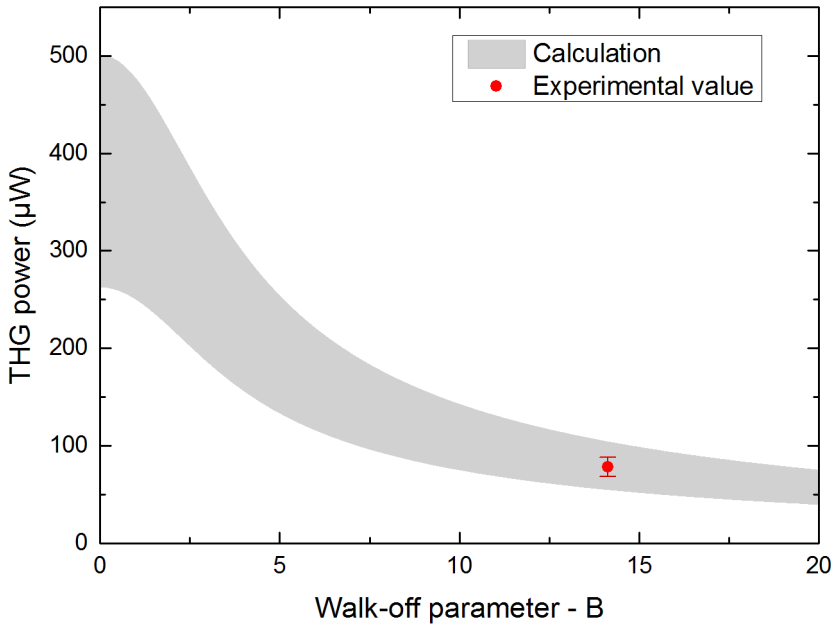

Figure 5.19: Effect of walk-off parameter on the SFG process, calculated using the parameters in table 5.2. $B = 14$ is the walk-off parameter value in our experiment.

It is important to notice that the maximum value suggested by this plot (at $B = 0$) is defined by the values set for all the variables involved, and could potentially increase in a different configuration.

In relation to the optimum configuration, we can look at how the optimum beam sizes are affected by the walk-off angle of the crystal. We have already seen how the optimum values are usually found around $\xi = 1$, and in particular $\xi = 2.84$ for SHG with 0 walk-off. However, the optimum focusing is heavily affected by the walk-off suffered by the beams, and so a tight waist (which maximizes photon density, increasing the efficiency of the process) is not ideal in systems with a high walk-off angle. We have calculated the output power of our process as a function of the focusing parameters for different values of the walk-off parameter. Since we are mixing two beams, on each plot one occupies the horizontal axis, while the other is fixed at our experimental value.

We observe how the optimum ξ parameter shifts towards looser focus in both cases. While the peak for $B = 0$ is always near $\xi = 1$, it drifts an order of magnitude for

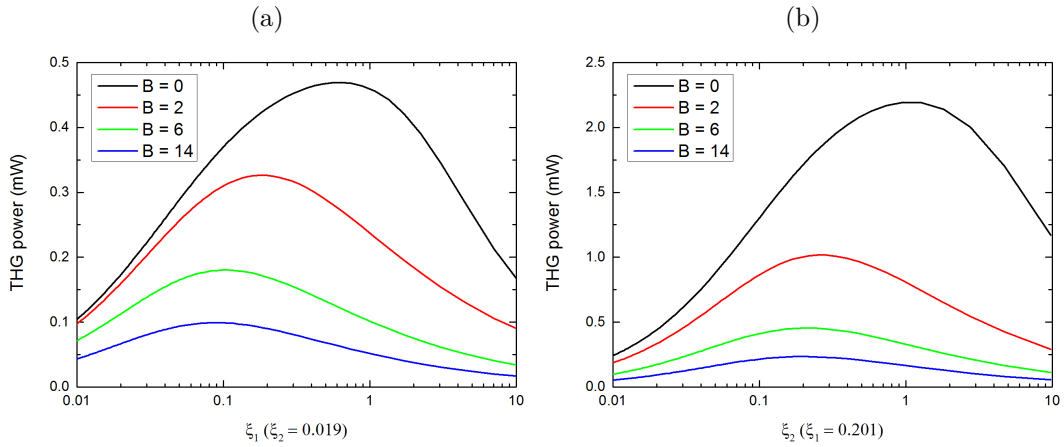

Figure 5.20: THG output power with respect to the focusing parameters of the fundamental (ξ_1) and SHG (ξ_2) beams for different values of the walk-off parameter. a) Varying ξ_1 and fixed ξ_2. b) Varying ξ_2 and fixed ξ_1.

values of $B = 14$, such as in our system. The plots, especially figure 5.20a, show as well how, in SFG, the optimum focusing parameter of one of the beams is also affected by the focusing of the second beam, trying to also maximize the overlap between them: while in figure 5.20b the fixed ξ_1, being larger, allows for ξ_2 to be around the unit; in figure 5.20a the low value of ξ_2 forces ξ_1 values under the unit even at $B = 0$. From figure 5.20b we can see how a focusing parameter $\xi_1 \sim 0.2$ in our setup would be ideal considering the size of the fundamental beam, offering output powers around 0.25 mW. Unfortunately, finding a compromise between all the factors involved (space, waists in SDL and LBO, cavity length and stability...) only allowed for values roughly an order of magnitude smaller, negatively affecting the THG output power. The divergence of the SHG beam, which did not permit a tight focus in our cavity configuration, together with its low power are currently limiting the output power of the laser, but this problems are by no means irresoluble, and overcoming them will help unleash the potential of this type of laser.

5.4 Optimizing the system

As we have seen in the previous sections, most of the problems, or limitations faced when building an intracavity tripled laser (other than intracavity losses caused by the optical elements) can be blamed on the walk-off angle of the crystal, especially high in BBO at deep UV wavelengths. The walk-off suffered in LBO in the SHG process is much smaller, but is also a limitation as we showed in section 5.2.5. Since non-critical phase matching is not possible at the wavelengths of interest (at a glance, the critical phase matching angle is close to 60°, relatively equidistant from ordinary and extraordinary axes), we have briefly investigated other possible solutions, namely walk-off compensation and quasi-phase matching in periodically poled crystals.

5.4.1 Walk-off compensation

Walk-off compensation consists of the use of several nonlinear crystals (several pieces of the same crystal), oriented such that the walk-off suffered inside each part occurs in the opposite direction in the following, thus being effectively compensated. This method has been extensively studied (see e.g. [14, 15]) and has been proved to offer improvements in output power as well as beam quality [16–18]. Walk-off compensation addresses both beam separation and frequency conversion efficiency.

Beam separation is solved in walk-off compensating crystals when using an even number of stages. If in the first stage the walk-off affected beam drifts away from the optical axis, in the second stage it drifts back due to the walk-off occurring in the opposite direction. While this of course does not work with an odd number of nonlinear stages, the beam separation is still reduced since only the last, odd part is not compensated. A system with half-length parts at the beginning and end of the walk-off compensating structure has been suggested to increase the process efficiency even further [19].

The efficiency of the nonlinear process is also improved by walk-off compensating crystals. This can be explained in terms of the walk-off parameter: B is defined by the walk-off angle and the crystal length (wavevector is not relevant in this case) and while the crystal material determines the walk-off angle and thus it cannot be easily modified (temperature-assisted phase matching does not produce a significant change at the required wavelengths in BBO), the crystal length can usually be chosen over a broad range. As seen in figure 5.15, shorter crystal length produces smaller B values, thus increasing the efficiency of the process (per unit length at least). The drawback of short crystals is that, in general, reducing the interaction length greatly reduces the output power. Walk-off compensating crystals, however, can be as large as non-compensated crystals, at least in the scale of our current crystal sizes (around 5 mm), and therefore the frequency conversion process extends through the same length as in ordinary crystals. But because the walk-off compensating structure is composed of much shorter pieces that reverse the walk-off with respect to the previous component, the walk-off parameter is defined by the length of each part, rather than the length of the whole structure. As an example, a 5-mm-long BBO crystal as in our setup exhibits a walk-off parameter of $B = 14$, while a walk-off compensating structure of the same total length, made of 1-mm-long BBO components, presents a value of $B = 6$. If we consider this looking at figure 5.19, we can see that this structure would actually double the THG output power achievable in this system.

The drawback of these walk-off compensating structures is that they are not widely commercially available, and the prices are still very high as compared with their bulk counterparts. Since their fabrication is a highly specialised process, requiring for example crystal poling and vacuum bonding as described in [19], their implementation was outwith the scope of this work.

5.4.2 Quasi-phase matching

QPM is a technique that completely removes the walk-off effects by propagating all beams along a crystal axis. An added advantage of this method is that the polarization states of the beams can all be the same, so the dual waveplate we use to rotate the SHG polarization would not be needed. While phase matching over the whole crystal length cannot be achieved with this configuration, this method makes use of the coherence length to produce conversion over small periods. After one period, the axes are reversed to account for the phase mismatch. Advantages of this technique are a zero walk-off angle, and therefore potentially long crystals, and the possibility to use the highest nonlinear coefficient of the crystal. However, the conversion efficiency is reduced by a factor $2/(m\pi)$, where m is the order of the QPM. Periodical poling (PP) is currently the most common technique to achieve QPM, being necessary to calculate the poling period. While QPM is widely used in infrared lasers, providing large conversion efficiency without any walk-off side effects, in the UV region the manufacturing process is still in development, as the small poling periods required are very challenging to fabricate. As a result, it is common that at such short wavelengths the order of QPM is higher than one, thus reducing the effective nonlinear coefficient and the conversion efficiency of the process and even limiting the growing process to shorter lengths.

We considered QPM SHG for our particular case, which can solve the problems with beam overlap mismatch and improve the SHG beam quality, potentially increasing the subsequent SFG process. The solution offered as optimum was a 3^{rd} order QPM, pp-LBGO crystal, too short to produce enough SHG power for an efficient SFG process to be achievable. Absorption is also to be taken into account, since crystals such as pp-MgSLT, which offer a high nonlinear coefficient (as compared with other bulk crystals at our wavelength of interest), present it at the SHG wavelength of our system.

5.4.3 Optimum case

Considering the pace at which technology advances, the described manufacturing limitations may be overcome in the near future, thus allowing for a more efficient intracavity frequency tripling. In particular the use of a periodically poled crystal to achieve QPM SHG, removing any walk-off effect and the need of an intracavity dual waveplate, would be desirable for the first nonlinear step if the crystals allow for efficient conversion. Reducing the number of intracavity elements decreases the intracavity losses, allowing for higher intracavity power and therefore increasing the conversion efficiency of both nonlinear processes. As an added advantage, removing the rather bulky mount required by the waveplate (a rotational mount is needed in order to adjust the angle) would provide more flexibility in terms of cavity design. A walk-off compensating structure would possibly be the best option for the second nonlinear step, with potential to at least double the conversion efficiency of the SFG process. The given reasons could allow this system to reach the millwatt level while maintaining its simplicity and compact design.

References

[1] D. A. Kleinman, A. Ashkin, and G. D. Boyd. "Second-Harmonic Generation of Light by Focused Laser Beams". In: *Physical Review* 145.1 (May 1966), pp. 338–379. DOI: 10.1103/PhysRev.145.338.

[2] W. P. Risk, T. R. Gosnell, and A. V. Nurmikko. *Compact Blue-Green Lasers*. April. Cambridge: Cambridge University Press, 2003. DOI: 10.1017/CBO9780511606502.

[3] O. Svelto. *Principles of Lasers*. Boston, MA: Springer US, 2010, p. 4419. DOI: 10.1007/978-1-4419-1302-9.

[4] A. A. Tovar and L. W. Casperson. "Generalized beam matrices: Gaussian beam propagation in misaligned complex optical systems". In: *Journal of the Optical Society of America A* 12.7 (July 1995), p. 1522. DOI: 10.1364/JOSAA.12.001522.

[5] J. W. Goodman. *Introduction to Fourier optics*. 3rd. Engleweood: Roberts & Company Publishers, 2005, p. 528.

[6] G. C. Bhar and U. Chatterjee. "Analyses of Phase-Matching for Noncollinear Three-Wave Mixing in Uniaxial Crystals". In: *Japanese Journal of Applied Physics* 29.Part 1, No. 6 (June 1990), pp. 1103–1107. DOI: 10.1143/JJAP.29.1103.

[7] P. A. Franken, A. E. Hill, C. W. Peters, and G. Weinreich. "Generation of Optical Harmonics". In: *Physical Review Letters* 7.4 (Aug. 1961), pp. 118–119. DOI: 10.1103/PhysRevLett.7.118.

[8] J. A. Armstrong, N. Bloembergen, J. Ducuing, and P. S. Pershan. "Interactions between Light Waves in a Nonlinear Dielectric". In: *Physical Review* 127.6 (Sept. 1962), pp. 1918–1939. DOI: 10.1103/PhysRev.127.1918.

[9] D. A. Kleinman. "Theory of Second Harmonic Generation of Light". In: *Physical Review* 128.4 (Nov. 1962), pp. 1761–1775. DOI: 10.1103/PhysRev.128.1761.

[10] G. D. Boyd, A. Ashkin, J. M. Dziedzic, and D. A. Kleinman. "Second-Harmonic Generation of Light with Double Refraction". In: *Physical Review* 137.4A (Feb. 1965), A1305–A1320. DOI: 10.1103/PhysRev.137.A1305.

[11] J. Bjorkholm. "Optical Second-Harmonic Generation Using a Focused Gaussian Laser Beam". In: *Physical Review* 142 (1966), pp. 126–136. DOI: 10.1103/PhysRev.142.126.

[12] G. D. Boyd and D. A. Kleinman. "Parametric Interaction of Focused Gaussian Light Beams". In: *Journal of Applied Physics* 39.8 (1968), p. 3597. DOI: 10.1063/1.1656831.

[13] S. Guha and J. Falk. "The effects of focusing in the three-frequency parametric upconverter". In: *Journal of Applied Physics* 51.1 (Jan. 1980), pp. 50–60. DOI: 10.1063/1.327353.

[14] J.-J. Zondy, C. Bonnin, and D. Lupinski. "Second-harmonic generation with monolithic walk-off-compensating periodic structures. I. Theory". In: *Journal of the Optical Society of America B* 20.8 (Aug. 2003), p. 1675. DOI: 10.1364/JOSAB.20.001675.

[15] J.-J. Zondy, D. Kolker, C. Bonnin, and D. Lupinski. "Second-harmonic generation with monolithic walk-off-compensating periodic structures. II. Experiments". In: *Journal of the Optical Society of America B* 20.8 (Aug. 2003), p. 1695. DOI: 10.1364/JOSAB.20.001695.

[16] J. Friebe, K. Moldenhauer, E. M. Rasel, W. Ertmer, L. Isaenko, A. Yelisseyev, and J. J. Zondy. "β-BaB_2O_4 deep UV monolithic walk-off compensating tandem". In: *Optics Communications* 261.2 (2006), pp. 300–309. DOI: 10.1016/j.optcom.2005.12.008.

[17] T. Onda, M. Shinnosuke, and I. Shoji. "A New Walk-Off Compensating BBO Device with Thinner-Plate-Stacked Structure Fabricated by Room-Temperature Bonding". In: *Nonlinear Optics*. Washington, D.C.: OSA, 2013, NTu3B.1. DOI: 10.1364/NLO.2013.NTu3B.1.

[18] C. Jung, K.-K. Kim, B.-A. Yu, Y. L. Lee, W. Shin, H. Kang, and Y.-C. Noh. "Enhancement of ultraviolet-beam generation through a double walk-off compensation". In: *Applied Optics* 54.27 (Sept. 2015), p. 8043. DOI: 10.1364/AO.54.008043.

[19] K. Hara, S. Matsumoto, T. Onda, W. Nagashima, and I. Shoji. "Efficient Ultraviolet Second-Harmonic Generation from a Walk-Off-Compensating βBaB_2O_4 Device with a New Structure Fabricated by Room-Temperature Bonding". In: *Applied Physics Express* 5.5 (May 2012), p. 052201. DOI: 10.1143/APEX.5.052201.

CHAPTER 6

Conclusion

The work carried out and presented in this thesis has led to the development of a new UVC laser source based on a semiconductor disk laser. The approach exploits the inherent characteristics of SDLs for efficient intracavity frequency conversion to produce a simple and compact solution, removing the need for separate external enhancement cavities often used in frequency conversion systems and their associated cavity stabilization implementations. The whole tripling process takes place in continuous-wave operation, highlighting the potential of SDLs for intracavity applications (here represented by nonlinear frequency conversion). The emission of this laser, with a tunable wavelength around 225 nm, brings new (laser) light to a region characterised by its inaccessibility, with current options mostly limited to pulsed operation, fixed wavelength sources or complex setups difficult to develop outside the laboratory.

6.1 Semiconductor disk lasers

As summarised in Chapter 2, semiconductor disk lasers have seen major growth since first being implemented 20 years ago [1]. Their characteristics, namely high beam

quality, tunable wavelength with pump flexibility, power scaling, and capability for short pulse or single frequency operation [2], have expanded and improved to the point that mature, well-established, laser solutions are now being superseded in favour of these XXI century devices. Current advances in novel semiconductor materials also benefit this family of lasers, even more readily since no modifications or improvements for efficient carrier transport are needed thanks to the optical pump approach. At the same time, ongoing development in gain structure simulation and matching high quality material growth and fabrication translates into better performance of the semiconductor structures. And fabrication is indeed an active area of development nowadays, with advances as seemingly disparate as MIXSELs, semiconductor devices integrating the gain region and a SESAM mirror in the same structure [3, 4]; or thin film devices, in which the DBR is excluded, thus increasing the semiconductor materials SDLs can employ [5–7]. From scientific to commercial applications, SDLs are replacing well-established solutions. Considering the increasingly pace of advances in this field, we can only forecast a bright future for these lasers over a broad range of the electromagnetic spectrum.

6.2 Intracavity frequency tripling

Nonlinear optics, in particular nonlinear frequency conversion, played a major role over the course of this work, and careful study of the literature was needed to help understand all relevant processes. Control and optimization of each stage was a difficult yet important challenge that we needed to address. Since both the doubling and tripling processes deplete the fundamental intracavity power, considering that the power converted is actually extracted from the cavity, and taking into account that the laser presents an optimum output coupling value, it can be seen that an optimum conversion efficiency ratio should exist for each nonlinear conversion step that maximizes the final THG output power. These values were estimated to be 1.2 % and 1.8 % for our particular laser, well above current conversion efficiencies for similar AlGaInP SDLs [8].

There is still room for improvement in this respect, but further development of nonlinear crystals, e.g. very high resolution periodic poling, is probably needed to reach such high values. While intracavity losses are not considered in this estimate, maintaining them at minimun levels (e.g. high quality mirrors and coatings) is also required for efficient performance.

Although the general idea behind intracavity tripling is relatively simple (one nonlinear crystal for SHG and then a second for tripling via SFG) several implementations are possible with options regarding the order of the nonlinear stages, type-I or type-II conversion, crystal orientation, etc. Inverse crystal order to that used in this work, in which the tripling crystal is positioned between the gain structure and the doubling crystal, that has been successfully used [9] as a convenient means for taking advantage of both second harmonic beams, would not work efficiently here due to the large walk-off angles suffered at the short wavelengths involved. The properties of the nonlinear crystals used favoured type-I on both conversion steps, and a dual waveplate was used to maintain the correct polarization at all stages.

The tripling laser was built using 6-mirror and 5-mirror configurations, which offered different beam geometries in particular regarding the relative position of the mixing fields (fundamental and second harmonic). The results showed that this relative position critically affects the mixing process, with parallelism between both beams being an important factor.

While the 6-mirror cavity was only capable of producing no more than a few µW, it proved an easy cavity to align that worked as a first proof of concept, providing an intermediate step before setting up a more challenging laser cavity. The shorter but more alignment-sensitive 5-mirror cavity proved superior in performance to the 6-mirror cavity, giving a clear UVC signal around 225 nm and reaching up to 78 µW of continuous-wave deep-UV emission and over 350 cm^{-1} of tuning range.

Further optimisation of the system was investigated, paying especial attention to utilising both SHG beams in the mixing stage. The original setup only uses the forward propagating beam so the available SHG power for frequency tripling is only 50 % of the total. Preliminary testing suggests that adding an external mirror to reflect the backwards propagating SHG beam back into the cavity with additional directional steering (and thus some walk-off compensation) can double the performance of the last conversion stage without adding undue complexity to the setup. This should be considered in any future implementations or similar systems.

6.3 Beam walk-off

The complexity of the nonlinear processes involved in this work has made necessary a detailed look into the theory of nonlinear interactions, in an attempt to fully understand the underlying physics and find improvements that could be implemented in the laser, in particular to achieve greater efficiency and thus higher output powers.

Beam propagation was a concern from the beginning given the large walk-off angles suffered at the short wavelengths involved in this work. Type-I frequency conversion produces the output beam with extraordinary polarization, thus separating from the fundamental beam a distance proportional to the walk-off angle and the crystal length. Since the fundamental and SHG beams have to propagate through the same cavity, this separation can be increased to the point that the beams cannot interact for a subsequent SFG process. The effects of such beam separation in both of our cavities were studied, finding that while the 6-mirror cavity leads to closer beams ($\sim$50 %) the relative angle between them is an order of magnitude larger than in the 5-mirror cavity. The greater separation in the 5-mirror cavity seems to be less critical than the relative angle, probably due to the beam size of the beams, allowing them to interact even when not collinear.

The information about beam geometry found in the beam propagation study allowed for more accurate predictions when calculating models of sum-frequency generation, since beam size is critical to the conversion process. Other parameters, such as input beam powers, crystal length walk-off angle and nonlinear coefficient, also play an important role in the conversion efficiency [10, 11], but beam sizes (and their derived focusing factor) are the most sensitive to change. While this makes them easy to alter in order to optimise a given system, they are also difficult to measure and can be the cause of large errors in the estimations. Moreover, in this kind of system where one of the SFG input beams (SHG) is generated in the same cavity by the other (fundamental), de-coupled modification of such beam geometry becomes extremely difficult.

The estimated THG output power was calculated as a function of the different parameters under our control, showing how the large walk-off angle (and consequently large walk-off parameter) causes approximately a 5x reduction in the maximum possible conversion efficiency. While every effort was made to experimentally meet the estimated optimum values, walk-off is a formidable adversary difficult to defeat. It seems that a reduction of the walk-off parameter would provide a fair chance for improvement in this type of system, for which quasi-phase matching [12] and walk-off compensation [13, 14] are the preferred solutions. With manufacturing methods for these particular builds of crystals quickly improving and production costs becoming more and more affordable, suitable solutions could be available in the near future. Further to this, the system would benefit from increased intracavity power especially by means of higher efficiency SDL gain structures and intracavity loss reduction. Given the suitability of SDLs for power scaling, higher input power would of course lead to higher output power (a great work in this direction with GaInP-based SDLs is being carried out in the University of Stuttgart [8, 15, 16]), but reducing losses and optimizing the total conversion efficiency, aiming to match the optimum output coupling of the laser, should certainly be the priority for any future efforts to increase the UV power.

6.4 Competing technology

Deep ultraviolet has proven to be an elusive region for laser coverage given the high photon energies involved, with most of the available sources being excimer lasers. These lasers, however, are limited to pulsed operation at a fixed wavelength, albeit normally with Watt-level output power. Tunable emission at these short wavelengths is currently dominated by harmonic generation from dye lasers, but these systems present some serious drawbacks (e.g. cumbersome architecture, toxicity and high cost). The most common solid-state alternative are Ti:Sapphire lasers frequency converted to higher harmonics, showing a broad range of emission although usually in pulsed operation.

Emerging semiconductor lasers offer continuous-wave or pulsed operation with tunable output, standing out as a bright and economical alternative. Deep UV emission with these lasers is also achieved by means of harmonic generation, and while established materials emitting in the near infrared can be converted through several stages to reach such short wavelengths, newer materials allowing visible fundamental emission imply fewer conversion stages are required to reach the UVC region.

Kaneda *et al.* [17, 18] have shown deep UV operation from a fundamental emission just under 1 µm, generating the 4^{th} harmonic by means of several nonlinear stages. Their approach, however, does not benefit from the SDL external cavity, rather making use of enhancing resonators that avoid introducing losses in the fundamental wavelength at the cost of a more complex setup.

Semiconductor disk lasers based on Gallium Nitrides (GaN) with fundamental emission in the blue region could provide a simpler, single nonlinear conversion step system to reach the deep UV. Nevertheless, fundamental emission itself already presents challenges that limit its performance [19], in particular finding suitable DBR materials (lattice mismatch between AlN and GaN is too large) [20].

Commercial semiconductor devices (laser diode based, not SDLs) emitting in the 220 nm – 230 nm region have already been announced [21], albeit working at fixed wavelengths, in pulsed or CW operation. Other diode-based laser solutions that make use of multiple external resonators to achieve deep UV output are currently further developed and offer output power in the mW range [22].

6.5 Summary

In summary, we have demonstrated intracavity third harmonic generation, or tripling, in a visible SDL, building a continuous-wave, tunable, deep ultraviolet laser source and producing the shortest wavelength to date from an SDL. The emission of 78 µW of deep UV output power and tuning over 350 cm^{-1} is produced from a simple and relatively compact setup that benefits from the short fundamental wavelength and high intracavity fields available in this type of laser. As described in Chapter 1, many applications (e.g. in atmospheric or combustion spectroscopy) may benefit from such a compact UVC laser source, with potential for in-field operations and capable of being engineered to target specifics. With dense populated cities reaching dangerous level of air pollution, detection of NO, an important result of combustion that is related to ozone depletion and smog formation, could serve as a first proof of concept of the utility of this system. While further work and optimisation is needed before semiconductor lasers conquer the <250 nm region, this approach shows SDLs are up for the task.

References

[1] M. Kuznetsov, F. Hakimi, R. Sprague, and A. Mooradian. "High-Power (0.5W CW) Diode-Pumped Vertical-External-Cavity Surface-Emitting Semiconductor Lasers with Circular TEM_{00} Beams". In: *IEEE Photonics Technology Letters* 9.8 (1997), pp. 1063–1065. DOI: 10.1109/68.605500.

[2] S. Calvez, J. E. Hastie, M. Guina, O. G. Okhotnikov, and M. D. Dawson. "Semiconductor disk lasers for the generation of visible and ultraviolet radiation". In: *Laser & Photonics Review* 3.5 (Sept. 2009), pp. 407–434. DOI: 10.1002/lpor.200810042.

[3] A.-R. Bellancourt, D. Maas, B. Rudin, M. Golling, T. Südmeyer, and U. Keller. "Modelocked integrated external-cavity surface emitting laser". In: *IET Optoelectronics* 3.2 (Apr. 2009), pp. 61–72.

[4] C. G. E. Alfieri, D. Waldburger, S. M. Link, E. Gini, M. Golling, B. W. Tilma, M. Mangold, and U. Keller. "Recent progress in high power ultrafast MIXSELs". In: *Proc.SPIE* 9734 (2016), p. 9734. DOI: 10.1117/12.2212165.

[5] Z. Yang, A. R. Albrecht, J. G. Cederberg, and M. Sheik-Bahae. "DBR-free optically pumped semiconductor disk lasers". In: 9349 (Mar. 2015). Ed. by M. Guina, p. 9349. DOI: 10.1117/12.2079696.

[6] B. E. Jones. "ZnCdMgSe and AlGaInP multi-quantum well films for colour conversion and optically-pumped visible lasers". PhD thesis. University of Strathclyde, 2015, p. 201.

[7] H. Kahle, C. M. N. Mateo, U. Brauch, P. Tatar-Mathes, R. Bek, M. Jetter, T. Graf, and P. Michler. "Semiconductor membrane external-cavity surface-emitting laser (MECSEL)". In: *Optica* 3.12 (Dec. 2016), pp. 1506–1512. DOI: 10.1364/optica.3.001506.

[8] H. Kahle, R. Bek, M. Heldmaier, T. Schwarzbäck, M. Jetter, and P. Michler. "High optical output power in the UVA range of a frequency-doubled, strain-

compensated AlGaInP-VECSEL". In: *Applied Physics Express* 7.9 (Sept. 2014), p. 092705. DOI: 10.7567/APEX.7.092705.

[9] Q.-z. Shu, A. L. Caprara, J. D. Berger, D. W. Anthon, H. Jerman, and L. Spinelli. "Intracavity-tripled optically-pumped semiconductor laser at 355 nm". In: *Lasers and Applications in Science and Engineering*. Ed. by W. A. Clarkson, N. Hodgson, and R. K. Shori. Vol. 7193. San Jose: SPIE, Feb. 2009, p. 719319. DOI: 10.1117/12.816073.

[10] G. D. Boyd and D. A. Kleinman. "Parametric Interaction of Focused Gaussian Light Beams". In: *Journal of Applied Physics* 39.8 (1968), p. 3597. DOI: 10.1063/1.1656831.

[11] S. Guha and J. Falk. "The effects of focusing in the three-frequency parametric upconverter". In: *Journal of Applied Physics* 51.1 (Jan. 1980), pp. 50–60. DOI: 10.1063/1.327353.

[12] J. Hirohashi, T. Taniuchi, M. Hatori, K. Imai, M. Sakairi, M. Matsukura, S. Takekawa, H. Motegi, S. Makio, S. Miyazawa, and Y. Furukawa. "300 mW 355 nm generation by PP-LBGO". In: *Advanced Solid State Lasers*. Vol. 1. c. Washington, D.C.: OSA, 2014, ATu4A.4. DOI: 10.1364/ASSL.2014.ATu4A.4.

[13] J.-J. Zondy, C. Bonnin, and D. Lupinski. "Second-harmonic generation with monolithic walk-off-compensating periodic structures. I. Theory". In: *Journal of the Optical Society of America B* 20.8 (Aug. 2003), p. 1675. DOI: 10.1364/JOSAB.20.001675.

[14] J.-J. Zondy, D. Kolker, C. Bonnin, and D. Lupinski. "Second-harmonic generation with monolithic walk-off-compensating periodic structures. II. Experiments". In: *Journal of the Optical Society of America B* 20.8 (Aug. 2003), p. 1695. DOI: 10.1364/JOSAB.20.001695.

[15] C. M. N. Mateo, U. Brauch, H. Kahle, R. Bek, T. Schwarzbäck, M. Jetter, M. Abdou Ahmed, P. Michler, and T. Graf. "Efficiency and power scaling of in-well and multi-pass pumped AlGaInP VECSELs". In: *SPIE 9734*. Ed. by K. G. Wilcox. Mar. 2016, p. 973410. DOI: 10.1117/12.2212162.

[16] P. Tatar-Mathes, H. Kahle, C. M. N. Mateo, U. Brauch, R. Bek, M. Jetter, T. Graf, and P. Michler. "Improved gain chip holder design for high efficient, high power AlGaInP-VECSEL". In: *Society of Photo-Optical Instrumentation Engineers (SPIE) Conference Series*. Vol. 10087. Society of Photo-Optical Instrumentation Engineers (SPIE) Conference Series. Mar. 2017, 100870R. DOI: 10.1117/12.2253670.

[17] Y. Kaneda, J. M. Yarborough, L. Li, N. Peyghambarian, L. Fan, C. Hessenius, M. Fallahi, J. Hader, J. V. Moloney, Y. Honda, M. Nishioka, Y. Shimizu, K. Miyazono, H. Shimatani, M. Yoshimura, Y. Mori, Y. Kitaoka, and T. Sasaki. "Continuous-wave all-solid-state 244 nm deep-ultraviolet laser source by fourth-harmonic generation of an optically pumped semiconductor laser using $CsLiB_6O_{10}$ in an external resonator". In: *Optics Letters* 33.15 (July 2008), p. 1705. DOI: 10.1364/ol.33.001705.

[18] Y. Kaneda, J. M. Yarborough, Y. Merzlyak, A. Yamaguchi, K. Hayashida, N. Ohmae, and H. Katori. "Continuous-wave, single-frequency 229 nm laser source for laser cooling of cadmium atoms". In: *Optics Letters* 41.4 (Feb. 2016), p. 705. DOI: 10.1364/OL.41.000705.

[19] R. Debusmann, N. Dhidah, V. Hoffmann, L. Weixelbaum, U. Brauch, T. Graf, M. Weyers, and M. Kneissl. "InGaN-GaN disk laser for blue-violet emission wavelengths". In: *IEEE Photonics Technology Letters* 22.9 (2010), pp. 652–654. DOI: 10.1109/LPT.2010.2043668.

[20] C. Berger, A. Dadgar, J. Bläsing, A. Lesnik, P. Veit, G. Schmidt, T. Hempel, J. Christen, A. Krost, and A. Strittmatter. "Growth of AlInN/GaN distributed Bragg reflectors with improved interface quality". In: *Journal of Crystal Growth* 414 (Mar. 2015), pp. 105–109. DOI: 10.1016/j.jcrysgro.2014.09.008.

[21] Sharp. *UVC Laser Modules*. http://www.sle.sharp.co.uk/sharp/apps/sle-web/research/system/devices/UVC/Laser/modules/index.html. 2016.

[22] Toptica Photonics. *TA-FHG pro*. https://www.toptica.com/products/tunable-diode-lasers/frequency-converted-lasers/ta-fhg-pro/.

APPENDIX A

SimCav

A.1 Introduction

Designing compact, optimised laser resonators can be a complex task, and the difficulty quickly escalates when 4, 5 or even more mirrors are required, as for the work presented in this thesis. Moreover, aside from resonator stability, particular beam sizes are usually desired at certain optical elements.

Software for designing cavity resonators is, however, relatively scarce. Many existing programs are now outdated, made for outdated operating systems, or are very expensive. Often the software being used is simply no more than an elaborate calculator, without the capacity to automatically resolve cavities, offering limited assistance in the search for the optimum resonator. Moreover, most of the available software is propietary, restricting the freedom of the users to a predefined schema that commonly lacks the flexibility often required in such a rapidly evolving field, with further limitations on the choice of operating system.

SimCav is a multiplatform software, developed during this work for advanced design of laser cavities. Indeed it maintains the common functionality of quickly drawing user made resonators, but SimCav also offers design calculations previously done by trial and error or cumbersome calculations. The user can trigger this advance feature simply by defining variations over multiple parameters and setting the required conditions the cavity must fulfil.

The program features a simple mouse-based interface for ease of use, such that advanced knowledge of computers or programming languages is not required. In addition, 'power users' can modify and adapt the program to their particular needs thanks to its release under the GNU General Public License (GPL). SimCav is written in Python, a powerful, high-level programming language that emphasizes code readability and simplicity (simple is better than complex, complex is better than complicated; as expressed in the Zen of Python [1]).

SimCav can run in any system that has Python (and a few of its most common modules) installed, and native applications are available for Linux, Windows and Mac. No installation is required, so using it is as simple as 'click and run'. The designs can be saved for future use and can be used over multiple platforms.

A.2 Mathematical background

SimCav makes use of ray transfer matrix analysis (also called ABCD formalism) for its core calculations. In this formalism (that can be found in detail in the literature, e.g. [2]), any optical element can be described by a 2x2 matrix:

$$M_{\text{element}} = \begin{bmatrix} A & B \\ C & D \end{bmatrix} \tag{A.1}$$

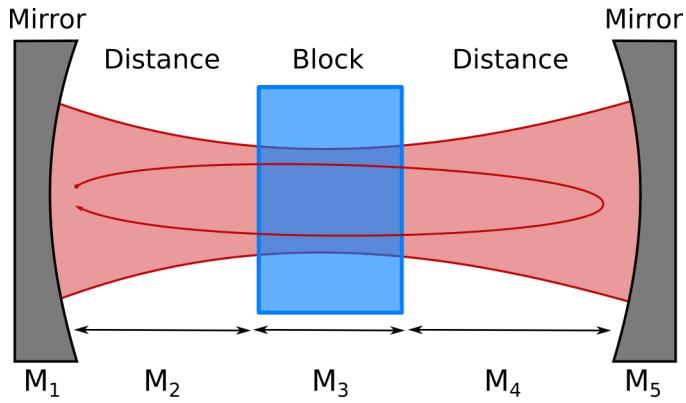

Figure A.1: A simple cavity for analysis. The optical elements are defined as in equation (A.2).

The four matrix elements that give name to the formalism will appear hereinafter.

A cavity can then be described by the product of the matrices of its components. In a resonator, this should be done considering the light round trip within, as expressed in figure A.1 (starting in element M_1).

$$M_{\text{roundtrip}} = M_2 \times M_3 \times M_4 \times M_5 \times M_4 \times M_3 \times M_2 \times M_1 \tag{A.2}$$

The beam inside the cavity can be described by means of the complex beam parameter:

$$\frac{1}{q(z)} = \frac{1}{R(z)} - \frac{i\lambda_0}{\pi n w(z)^2} \tag{A.3}$$

Where z is the distance, $R(z)$ and $w(z)$ are respectively beam radius and beam size at position z, n is the refractive index and λ_0 is the vacuum wavelength. The value of q at $z = 0$ can be obtained from the round trip condition (the beam must be unchanged after a round trip):

$$\begin{pmatrix} q(0) \\ 1 \end{pmatrix} = M_{\text{roundtrip}} \times \begin{pmatrix} q(0) \\ 1 \end{pmatrix} \qquad \Rightarrow \qquad q(0) = \frac{Aq(0) + B}{Cq(0) + D} \tag{A.4}$$

$$q(0) = \frac{-(D - A) \pm \sqrt{(D - A)^2 + 4BC}}{2C} \tag{A.5}$$

Once the complex beam parameter $q(z = 0)$ has been found, the characteristics of the beam at any given point of the cavity can be calculated simply by propagating it:

$$q(z) = q(0) + z \tag{A.6}$$

And recalculating it at the other side of an interface (which is an optical element with matrix $M_{\text{interface}}$):

$$q_{\text{after}} = M_{\text{interface}} \times q_{\text{before}} \tag{A.7}$$

The stability of the resonator can also be obtained from the round trip matrix. The cavity will be stable if:

$$\left| \frac{A + D}{2} \right| < 1 \tag{A.8}$$

In the SimCav interface it is more convenient to normalize the stability, therefore it varies between not stable (0) and very stable (1). This simplifies the plotting and empties the negative vertical axis: since the calculations are done separately for the tangential and saggital planes, they can be plotted simultaneously in the positive and negative regions, respectively, of the vertical axis.

A.3 Conclusion

The original version of SimCav consisted in a simple yet powerful command line tool, but considering the lack of suitable cavity analysis software available, an effort was made to convert it to a program with a user-friendly graphical interface (figure A.2).

Currently, SimCav is available online [3], with applications for Linux, Windows and Mac ready to download. While the interface is intuitive, a short manual is also offered for reference. The source code is also available, hosted in GitLab [4] to simplify and encourage collaboration.

Finally, SimCav releases are published in Zenodo [5] and assigned a digital object identifier (DOI) making its management or citation effortless and straightforward.

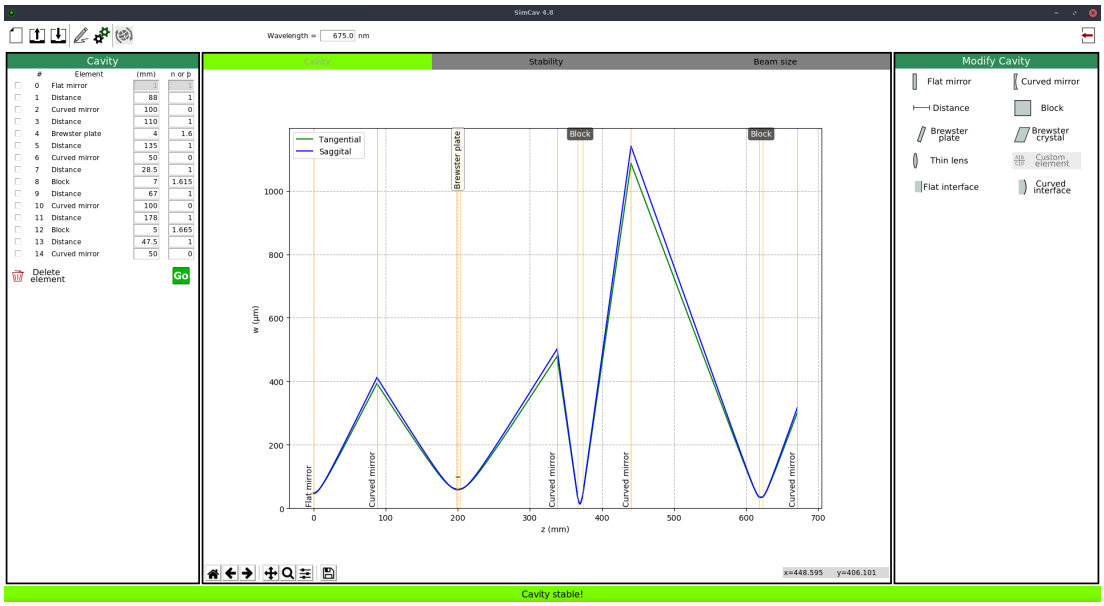

Figure A.2: SimCav features a modern and user-friendly graphical interface.

References

[1] T. Peters. *The Zen of Python*. https://www.python.org/dev/peps/pep-0020/. Aug. 2004.

[2] O. Svelto. *Principles of Lasers*. Boston, MA: Springer US, Dec. 28, 2009. DOI: 10.1007/978-1-4419-1302-9.

[3] J. M. Rodríguez-García. *SimCav website*. https://simcav.gitlab.io/. 2017.

[4] J. M. Rodríguez-García. *SimCav code*. https://gitlab.com/simcav/simcav. 2017.

[5] J. M. Rodríguez-García. *Simcav in Zenodo*. https://zenodo.org/record/1184130. 2017.

List of Publications

Julio M. Rodríguez-García, David Pabœuf, and Jennifer E. Hastie, "Tunable, CW laser emission at 225 nm via intracavity frequency tripling in a semiconductor disk laser," IEEE Journal of Selected Topics In Quantum Electronics 23 (6) 5100608 (2017)
DOI: 10.1109/JSTQE.2017.2696882

David Pabœuf, Brynmor E. Jones, Julio M. Rodríguez García, Peter J. Schlosser, Dariusz Swierad, Joshua Hughes, Ole Kock, Lyndsie Smith, Kai Bongs, Yeshpal Singh, Stefano Origlia, Stephan Chiller, and Jennifer E. Hastie, "Narrow linewidth visible/UV semiconductor disk lasers for quantum technologies," Photonics West, San Francisco, USA, Paper 9734-22 (2016)
Invited Talk

Julio M. Rodríguez García, David Pabœuf, and Jennifer E. Hastie, "Continuous-wave semiconductor disk laser emitting at 224 nm via intracavity frequency tripling," presented at Advanced Solid State Lasers, Berlin, Paper AM5A.47 (2015)
DOI: 10.1364/ASSL.2015.AM5A.47
Awarded Best Student Poster